



Available online at www.sciencedirect.com



Materials Science and Engineering R 60 (2008) 1–51



Reports: A Review Journal

www.elsevier.com/locate/mser

Growth of nanowires

N. Wang ^{a,*}, Y. Cai ^a, R.Q. Zhang ^b

^a Department of Physics and the Institute of Nano Science and Technology,
the Hong Kong University of Science and Technology, Hong Kong, China

^b Center of Super-Diamond and Advanced Films (COSDAF) & Department of Physics and Materials Science,
City University of Hong Kong, Hong Kong, China

Available online 5 March 2008

Abstract

The tremendous interest in nanoscale structures such as quantum dots (zero-dimension) and wires (quasi-one-dimension) stems from their size-dependent properties. One-dimensional (1D) semiconductor nanostructures are of particular interest because of their potential applications in nanoscale electronic and optoelectronic devices. For 1D semiconductor nanomaterials to have wide practical application, however, several areas require further development. In particular, the fabrication of desired 1D nanomaterials with tailored atomic structures and their assembly into functional devices are still major challenges for nanotechnologists. In this review, we focus on the status of research on the formation of nanowire structures via highly anisotropic growth of nanocrystals of semiconductor and metal oxide materials with an emphasis on the structural characterization of the nucleation, initial growth, defects and interface structures, as well as on theoretical analyses of nanocrystal formation, reactivity and stability. We review various methods used and mechanisms involved to generate 1D nanostructures from different material systems through self-organized growth techniques including vapor–liquid–solid growth, oxide-assisted chemical vapor deposition (without a metal catalyst), laser ablation, thermal evaporation, metal-catalyzed molecular beam epitaxy, chemical beam epitaxy and hydrothermal reaction. 1D nanostructures grown by these technologies have been observed to exhibit unusual growth phenomena and unexpected properties, e.g., diameter-dependent and temperature-dependent growth directions, structural transformation by enhanced photothermal effects and phase transformation induced by the point contact reaction in ultra-thin semiconductor nanowires. Recent progress in controlling growth directions, defects, interface structures, structural transformation, contacts and hetero-junctions in 1D nanostructures is addressed. Also reviewed are the quantitative explorations and predictions of some challenging 1D nanostructures and descriptions of the growth mechanisms of 1D nanostructures, based on the energetic, dynamic and kinetic behaviors of the building block nanostructures and their surfaces and/or interfaces.

© 2008 Elsevier B.V. All rights reserved.

Contents

1. Introduction	2
2. Growth technologies for nanowires	3
2.1. Vapor–liquid–solid (VLS) technique	3
2.2. Laser-assisted growth	5
2.3. Thermal evaporation	6
2.4. Metal-catalyzed molecular-beam epitaxy	7
2.5. Solution methods	9
3. Growth mechanisms of nanowires	9
3.1. Metal-catalyzed growth	9
3.2. Vapor–solid growth	14
3.2.1. Internal anisotropic surfaces	14
3.2.2. Crystal defects	14
3.2.3. Self-catalytic growth	15

* Corresponding author. Tel.: +852 2358 7489; fax: +852 2358 1652.

E-mail address: phwang@ust.hk (N. Wang).

3.3.	Oxide-assisted growth	16
3.3.1.	Kinetics and reactivity of silicon oxide in nucleation and growth	16
3.3.2.	Effect of defects in 1D growth	18
3.3.3.	Effect of external electrical field in 1D growth	19
3.4.	Self-assembly growth from solution	20
3.4.1.	Solution-liquid-solid (SLS) growth from seeds	20
3.4.2.	Self-assembly oriented attachment growth	20
3.4.3.	Anisotropic growth of crystals by kinetic control	20
4.	Controlled growth of nanowires	22
4.1.	Control of structures, growth direction and defects in nanowires	22
4.1.1.	Interface structures	22
4.1.2.	The growth direction of VLS nanowires	23
4.1.3.	Defects in nanowires	28
4.1.4.	From nanowire to nanoribbon	31
4.2.	Structural transformation in nanowires	32
4.2.1.	Surface relaxation and saturation of zinc oxide nanowires	32
4.2.2.	The stability of Si nanowires	34
4.2.3.	Optical rapid annealing effect	35
4.3.	Contacts and heterostructures in nanowires	37
4.3.1.	Metal-semiconductor contacts	37
4.3.2.	Heterostructures in nanowires	39
5.	Other challenging nanowire structures	41
5.1.	Non-tetrahedral Si nanowires	41
5.2.	Oxide nanowires	43
5.2.1.	Silicon oxide nanowires	43
5.2.2.	Silicon dioxide tube-like nanowires	45
5.2.3.	Zinc oxide tube-like nanowires	46
6.	Concluding remarks	47
	Acknowledgements	47
	References	48

1. Introduction

In the physics of nanoscale structures, quantum effects play an increasingly prominent role [1]. Quantum wires have demonstrated interesting electrical transport properties that are not seen in bulk materials. This is because, in quantum wires, electrons could be quantum-confined laterally and thus could occupy discrete energy levels that are different from the energy bands found in bulk materials. Due to low electron density and low effective mass, the quantized conductivity is more easily observed in semiconductors, e.g., Si and GaAs, than in metals [2]. In addition to the opportunity to describe the new physics demonstrated by nanowires, much effort has been devoted to fabricating high-quality semiconductor nanowires by employing different techniques because of the importance of semiconductor materials to the electronics industry. The most popular technique used to fabricate semiconductor artificial structures with feature sizes in the sub-100 nm range is lithography [3,4], which involves tedious processes of photoresist removal, chemical or ion-beam etching and surface passivation, etc. On semiconductor nanostructures, etching processes always lead to significant surface damage, and thus surface states are introduced to the nanostructures. Such damage may not be serious for the structures in the micrometer range. However, structures with dimensions in the nanometer range are very sensitive to the surface states or impurities induced by fabrication processes. One-dimensional (1D)

nanostructures formed “naturally” (also called self-organized growth) without the aids of *ex situ* techniques, such as chemical etching, are desirable not only in fundamental research but also in future nanodevice design and fabrication.

In this paper, various novel technologies for synthesizing nanowires are reviewed. A well-known self-organized growth mechanism for creating nanowires is the vapor–liquid–solid (VLS) process (also known as metal catalytic growth [5]). This technique can produce free-standing crystalline nanowires of semiconductor and metal oxide materials with fully controlled nucleation sites and diameters from pre-formed metal catalysts. Since the 1960s, semiconductor whiskers grown by this technique [5,6] have been extensively studied. In recent years, various new techniques have been developed to realize 1D nanostructures, such as laser-assisted chemical vapor deposition (CVD) [7–10], oxide-assisted CVD (without a metal catalyst) [11], thermal CVD [12], metal-catalyzed molecular beam epitaxy (MBE) [13–15] and chemical beam epitaxy (CBE) [16]. Though the number of various kinds of 1D nanostructures fabricated via different techniques increases dramatically every year, our understanding of the basic process of 1D nanostructure formation has not reached maturity. How to fabricate desired 1D nanomaterials with tailored atomic structures and how to integrate functional nanostructures into devices are still challenging issues for materials scientists. For 1D semiconductor nanomaterials to have wide practical applications, however, many areas require further pursuing.

This review focuses on describing the status of research on the formation of semiconductor and metal oxide nanowires. It consists of four sections. After a brief introduction, the first section introduces the growth technologies currently employed to synthesize nanowires with an emphasis on advances in the newly developed techniques of metal-catalyzed MBE and CBE by which high-quality ultra-thin nanowire structures have been fabricated. These techniques allow high levels of control over atomic structures, chemical composition, defects, doping states, junctions, and so forth. We next discuss several novel nucleation and growth mechanisms and theoretical analyses of the formation, reactivity and stability of nanocrystals. The initial alloying process of metal catalysts, growth of nanowire nuclei, changes in nanowire shapes and diameters as well as deposition of source materials are described in the second section. In the third section, we describe the controlled growth and structures of nanowires. Recent progress in controlling growth directions, defects, interface structures, structural transformation, contacts and hetero-junctions is addressed. In the last section, we describe some theoretical nanowire structures that have not yet been observed or are challenging to synthesis.

2. Growth technologies for nanowires

2.1. Vapor–liquid–solid (VLS) technique

The VLS technique was first described by Wagner and Ellis [5] in 1964. They used Au particles as catalysts to grow crystalline semiconductor whiskers from vapor sources such as SiCl_4 or SiH_4 . The principle for Si whisker growth is schematically shown in Fig. 1(a). The Au particles deposited on the surface of an Si substrate react first with Si to form Au–Si alloy droplets at a certain temperature. As shown in the Au–Si phase diagram in Fig. 1(b), the melting temperature of the Au–Si alloy at the eutectic point is very low (about 363 °C at an Au:Si ratio of 4:1) compared with that of Au or Si. Au and Si can form a solid solution for all Si content (0–100%). In the case of Si deposition from the vapor mixture of SiCl_4 and H_2 , the reaction between SiCl_4 and H_2 happens at a temperature above 800 °C without the assistance of catalysts. Below this temperature, almost no deposition of Si occurs on the substrate

surface [6]. At a temperature above 363 °C, Au particles can form Si–Au eutectic droplets on Si surfaces, and the reduction of Si occurs at the Au–Si droplets due to a catalytic effect. The Au–Si droplets absorb Si from the vapor phase resulting in a supersaturated state. Since the melting point of Si (1414 °C) is much higher than that of the eutectic alloy, Si atoms precipitate from the supersaturated droplets and bond at the liquid–solid interface, and the liquid droplet rises from the Si substrate surface. The absorption, diffusion and precipitation processes of Si as schematically shown by the path 1 → 2 → 3 in Fig. 1(c) involve vapor, liquid and solid phases. The typical feature of the VLS reaction is its low activation energy compared with normal vapor–solid growth. The whiskers grow only in the areas seeded by metal catalysts, and their diameters are mainly determined by the sizes of the catalysts. The VLS method can result in unidirectional growth of many materials [6]. It has become a widely used technique for fabricating a variety of 1D nanomaterials that include elemental semiconductors [6–8,17–23], II–VI semiconductors [24–26], III–V semiconductors [27–41], oxides [42–47], nitrides [48] and carbides [49,50].

The experimental setup of the VLS reaction has been reported in previous work [5,6]. In brief, for Si nanowire growth, the sources can be SiH_4 mixed in H_2 at a typical ratio of 1:10. The reaction gases have to be diluted to about 2% in an Ar atmosphere. The pressure for the reaction is about 200 Torr, and the flow rate is kept at 1500 sccm. Au nanoparticles can be prepared simply by first depositing an Au thin film on an Si substrate using sputtering or thermal evaporation and then annealing the thin film to form droplets. Fig. 2(a) shows uniform Au nanoparticles formed by annealing an Au thin film (thickness = 1 nm) at 500 °C. A thick film results in large diameters of Au particles. Au particles arrays can be prepared by lithography techniques. Fig. 2(b) shows an Au disc array prepared by e-beam lithography. The thickness of the Au pattern is critical to the final sizes of the nanoparticles generated by the subsequent annealing. Au films that are too thin always result in splitting of the Au pattern (Fig. 2(c)). A proper treatment of the substrate surface by chemical etching and cleaning can result in the catalyst totally wetting the substrate surface (see Fig. 3(a)), which is important for later growth of the nanowires epitaxially on the substrate. Because of the oxide layer on the substrate surface or impurities on the

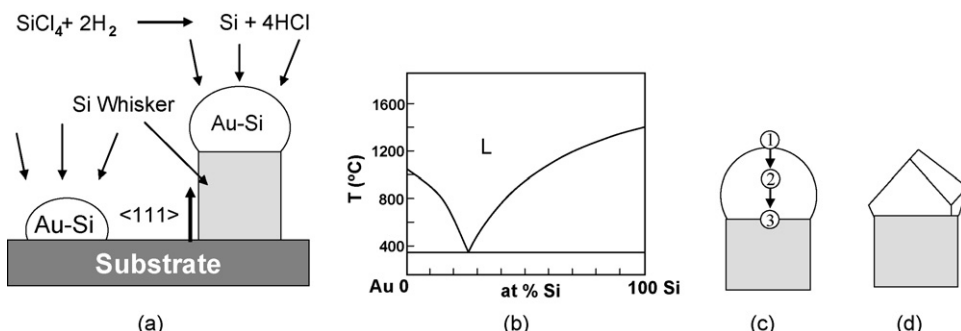


Fig. 1. Schematic illustration of Si whisker growth from vapor phases via Au–Si catalytic droplets. (a) The Au–Si droplet formed on an Si substrate catalyzes the whisker growth; (b) the Au–Si phase diagram. (c) The diffusion path of the source materials through a metal droplet; (d) the whisker growth can be catalyzed with a solid catalyst.

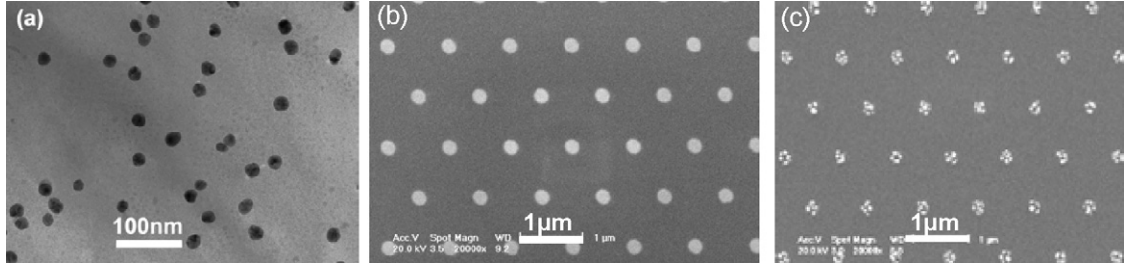


Fig. 2. (a) Au catalysts prepared by annealing a thin Au film. (b) Au patterns prepared by e-beam lithography. (c) Splitting of the Au particles by annealing.

catalyst surface induced by the lithography technique, Au catalysts may not wet the substrate surface. In this case, Si nanowires may not have orientation relationship with the substrate and grow along random directions (Fig. 3(b)). For Si nanowires with diameters larger than 20 nm, their growth is generally along the $\langle 1\ 1\ 1 \rangle$ direction. Thin Si nanowires with diameters smaller than 20 nm, however, show interesting growth behaviors for example the diameter-dependent and temperature-dependent growth direction (see details in Section 4.1).

Before growing Si nanowires, activation of Au nanoparticles may be needed. An inactivated Au particle will not lead to nanowire growth. The activation of Au–Si alloy droplets can be carried out in Ar or H₂ atmospheres. We have found that plasma treatment is effective for cleaning and activating the surfaces of Au catalysts. HCl mixed in the reaction gases can also effectively activate Au particles. However, the activation temperature largely relies on the diameters of Au catalysts. For large Au catalysts (diameter > 50 nm), the activation temperatures can be 800 °C or higher. Large Au catalysts can easily wet a Si substrate at sufficiently high temperatures and thus Si nanowires grow epitaxially even on an untreated substrate. In the growth of thin Si nanowires (diameter < 20 nm), the growth temperatures are about 500 °C. Too high activation temperatures may cause evaporation of the catalysts. The vacuum condition is another critical experimental parameter that affects nanowire growth. Low vacuum conditions may cause evaporation of Si from the substrate surface and thus result in a rough surface.

Under isothermal conditions, the crystalline structures of Si whiskers are generally perfect, though steps and facets occur on the whiskers' surfaces. Twinning structures and twin-dendrites (or branched whiskers) have been frequently observed in the whiskers. Though the cross-section of most whiskers is round (determined by the metal droplets), ribbon-like whiskers with a rectangular cross-section often coexist and show the $\langle 1\ 1\ 1 \rangle$ or $\langle 1\ 1\ 2 \rangle$ growth direction [17]. Dislocations or other crystalline defects are not essential for the growth of the whiskers via the VLS method. In different semiconductor material systems, whiskers with similar morphologies and structures have been fabricated by the VLS reaction and a variety of whisker forms have been obtained [6]. Although the VLS technique has been widely used for the fabrication of nanowires in recent years, the real absorption, reaction and diffusion processes of source atoms through the catalyst are complicated and largely depend on the experimental conditions and the material systems [52–54]. Many experiments have shown the deviation of some nanowire growth from the classical VLS mechanism. For example, it has been observed that nanowires of Ge [18,19], Si [22], GaAs [27] and InAs [28] can grow even at temperatures below their eutectic points. There has been a long-standing debate on whether the metal catalysts in these cases are solid particles (see Fig. 1(d)) or liquid droplets [54]. There are two main uncertainties in this debate: (1) because of the nanosize effect, the melting temperatures of nanoparticles are always lower than those of bulk materials and (2) it is not possible to measure the real temperature at the catalyst tips. In fact, in some cases, nanosized metal droplets are in a partially molten state

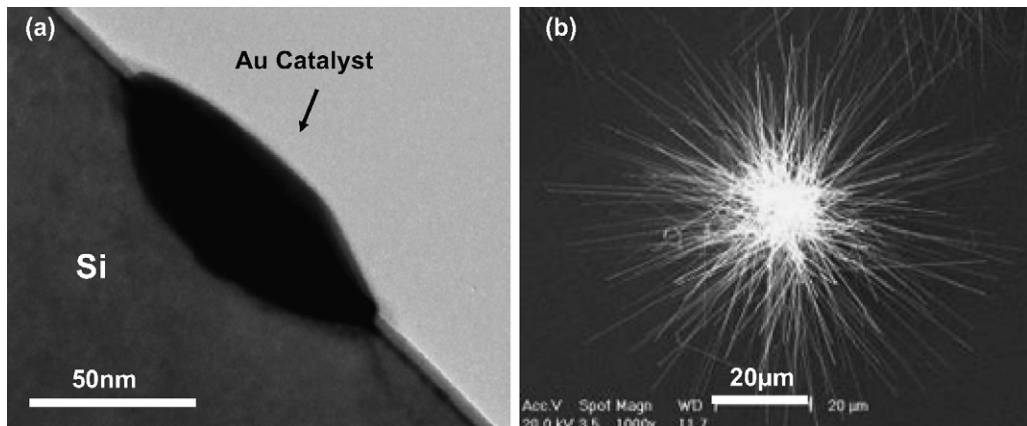


Fig. 3. (a) An Au catalyst reacts with the substrate after the activation treatment. (b) Si nanowires grow in different directions.

[51]. The surface and interface regions are liquid, while the cores of the droplets are solid.

The VLS mechanism is very successful in generating large quantities of 1D nanomaterials (single nanowires and heterostructured nanowires) with uniform crystalline structures not only in semiconductors but also in oxide, nitride and other material systems. However, it seems to be difficult to grow metal nanowires by the VLS method. The disadvantage of the VLS method may be the contamination caused by the necessary use of a metal particle as the catalyst. This may result in the change in the nanowire's properties. However, by selecting an appropriate catalyst, the affection of the contamination for specific properties of the nanowire can be minimized.

2.2. Laser-assisted growth

Among the various techniques developed to synthesize ultra-thin nanowires, of particular interest is the laser ablation of metal-containing solid targets or similar techniques [7–10], by which bulk-quantity nanowires can be readily obtained directly from solid source materials. When using metal catalysts, for example, for the synthesis of Si nanowires, this method is suggested to rely on the VLS mechanism, whereby the vapor (or gaseous clusters) generated by laser ablation dissolves in a molten metal catalyst and then crystallizes to form nanowires. Ultrasmall nanoparticles of metals or metal silicides in large quantities are rather easy to obtain from the high temperature induced by laser ablation. Assisted by laser ablation, these nanoparticles act as the critical catalyst for the nucleation and growth of nanowires.

The laser-assisted method has unique advantages over other growth techniques in synthesizing nanowires containing complex chemical compositions. This is because no matter how many elements are involved, it is not necessary to prepare the target (or the source materials) in a crystalline form. A simple mixture of the elements is good enough as the source material. The source materials are ablated into a vapor phase, which may have the same composition as the source materials. The vapor phase can be easily transferred to the substrate where nanowires nucleate and grow. A high-energy laser can ablate solid materials in an ultra short time and vaporize the materials in a non-thermo-equilibrium process, also called congruent evaporation [55]. This

technique is particularly useful in the synthesis of nanowires with a high-melting temperature, such as SiC nanowires [56]. It is also a very effective method in synthesizing nanowires with multi-components and doping nanowires during growth. The vaporized molecules (or clusters) by the high power laser have high kinetic energy (about 100 eV), and this largely enhances the chemical reaction, e.g., the reaction with oxygen or other gases, and thus can largely improve the crystal quality of the nanowires at a low substrate temperature. This special technique has many practical uses for the control of the stoichiometries of nanowires. For example, ZnO nanowires grown by thermal CVD always have oxygen vacancies and other defects that cause poor optical (non-band edge emission) and electrical (low conductivity compared with bulk ZnO crystals) properties. These defects cannot be easily eliminated even by annealing in oxygen after nanowire growth. ZnO nanowires synthesized by laser ablation, however, generally show better optical properties. Another example is that indium oxide nanowires synthesized by laser ablation have a significantly high mobility [57].

Fig. 4 is a schematic of the experimental setup of the laser-ablation technique. The laser used in the experiment can be any high-power pulsed laser, e.g., a Nd:YAG laser [7], an interfered femto-second laser [58] or an excimer laser [59]. The synthesis of Si nanowires by the experiment reported in Refs. [10,59,60] was carried out using a high-power KrF excimer pulsed laser (248 nm, 10 Hz, 400 mJ/pulse) to ablate a target in an evacuated (~500 Torr) quartz tube with Ar (50 sccm) flowing through the tube. Other inert gases, such as He, H₂ and N₂, can also be used as the ambient gases. The use of different ambient gases may influence the diameters of the nanowires and affects their optical properties [60]. The temperature around the target materials in the experiment was about 1200 °C. The target was highly pure Si powder mixed with Fe, Ni, or Co (about 0.5%). The laser beam (1 mm × 3 mm) was focused on the target surface. Si nanowire products (sponge-like, dark yellow in color as shown in **Fig. 5(a)**) formed on the Si substrate or the inner wall of the quartz tube near the water-cooled finger after 1 h of laser ablation. The temperature of the area around the substrate where the nanowire grew was approximately 900–1000 °C. The growth rate of the Si nanowires was about 10–80 μm/h.

By laser ablation, the metal powder is evaporated out of the target to form clusters. They are in a semi-liquid state and serve

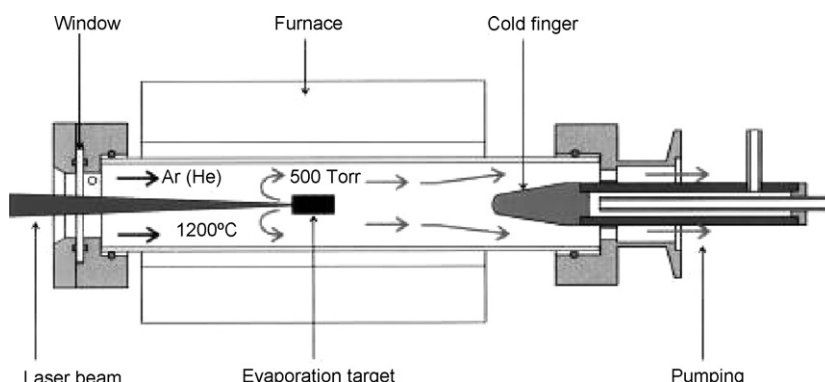


Fig. 4. Experimental setup for the synthesis of Si nanowires by laser ablation (Courtesy of Prof. I. Bello).

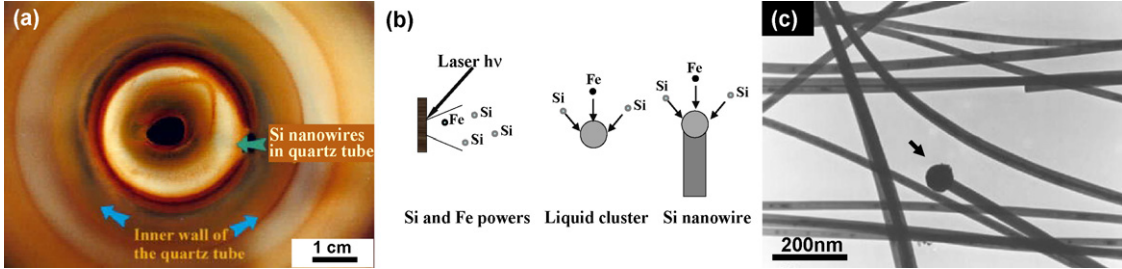


Fig. 5. (a) Si nanowire product. (b) Formation of Si nanowires from liquid clusters. (c) TEM image of Si nanowires catalyzed by metal droplets. The arrow indicates the metal catalyst on the nanowire tip.

as the energetically favored reaction sites for absorption of the reactant. They are also the nucleation sites for crystallization of the source materials when supersaturated (see Fig. 5(b)). Then, preferential 1D growth occurs in the presence of the reactant. Si nanowires obtained by ablating a metal-containing (0.5–1%) Si powder target are extremely long and straight. The typical diameters of the nanowires are 10–50 nm. There is a metal catalyst at the tip of each nanowire (Fig. 5(c)). During the laser ablation, the reaction is not under thermodynamic equilibrium conditions. Ultrasmall-size metal catalysts and thus very thin Si nanowires with diameters smaller than 10 nm can be easily generated by this method. The growth rate of Si nanowires from laser ablation depends on many factors, such as the power of the laser beam, the vacuum, the carrier gasses and the temperature. A rate of 500 $\mu\text{m}/\text{h}$ has been observed in Si nanowire growth assisted by laser ablation, which is much faster than that from the classical VLS using vapor sources.

Without adding any metal catalysts, however, nanowires of many other materials have been fabricated by laser ablation. These materials include metal oxides, some semiconductors and multi-component materials with rather complex stoichiometries. The growth of these nanowires is called self-catalyzed growth. Though no obvious catalyst is observed with these nanowires, it is possible that metal elements in the source materials may act as the catalysts. For example, the laser ablation of the ZnSe crystal surface may result in Zn clusters that act as the effective catalysts. Similar self-catalyst VLS growth has also been observed in the growth of GaN [61] and ZnO [62] nanowires. Nanowires with multi-components, for example, the yttrium–barium–copper–oxygen (YBCO) compound, have been synthesized by laser ablation of $\text{YBa}_2\text{Cu}_3\text{O}_7$ (a high T_c superconductor) in an oxygen atmosphere [63]. The

YBCO nanowires were structurally uniform. Their diameters range from 20 and 90 nm and their lengths are up to several micrometers. Most of the YBCO nanowires were single crystals (an orthorhombic lattice) and their axis was along the [0 0 1] direction. The growth mechanism of the YBCO nanowires is not known. It might be a self-catalytic growth or the oxide-assisted growth (without any metal catalysts) as discussed below in Section 2.3.

2.3. Thermal evaporation

Nanowires and some interesting morphologies of nanostructures such as nanoribbons, nano-tetrapods and comb-like structures [64,65] can be fabricated by a simple method of thermal evaporation of solid source materials. The experimental setup is extremely simple as shown in Fig. 6. The temperature gradient and the vacuum conditions are two critical parameters for the formation of nanowires by this method. Typical materials suitable for this fabrication are metal oxides, e.g., ZnO , SnO_2 , In_2O_3 , VO , etc. and some semiconductors [12,66]. The fabrication of these nanowires is simply through evaporating commercial metal oxide powders at elevated temperatures under a vacuum or in an inert gas atmosphere with a negative pressure. Nanowire products form in the low-temperature regions where materials deposit from the vapor phase. It is believed that the nanowires are generated directly from the vapor phase in the absence of a metal catalyst, and this process is often called vapor–solid (VS) growth. To generate the vapor phases of the source materials, vacuum conditions are sometimes needed. This is because some materials may not sublime in the normal atmosphere. An effective way to generate the vapor source materials in a normal atmosphere is

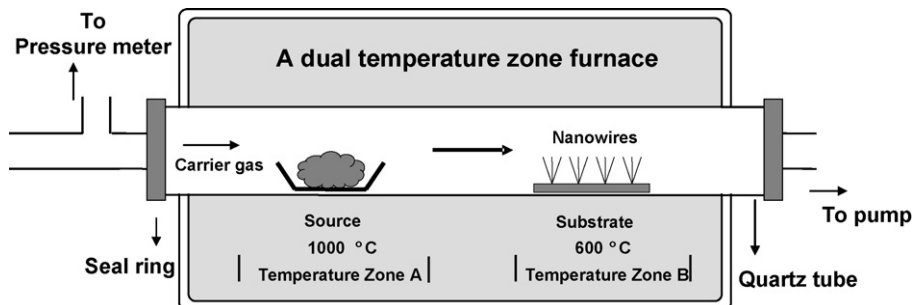


Fig. 6. A simple experimental setup of the thermal evaporation method for synthesizing ZnO nanostructures. The source material is ZnO or a mixture of ZnO and carbon. Different forms of the ZnO nanostructures, e.g., nanowires and ribbons, grow in different temperature zones.

to add additional materials to react with the source materials. For example, ZnO powder does not sublime in a normal atmosphere at 1000 °C. By adding carbon powder to react with the ZnO source, Zn or Zn-suboxide vapor phases can be easily generated at 1000 °C. Various forms of ZnO nanostructures grow in the low-temperature zone. In this case, vacuum conditions, carrying gases and catalysts are all unnecessary. The temperature is critical for the formation of different forms of ZnO nanostructures [67].

The growth mechanisms of many nanowires from thermal evaporation (without adding metal catalysts) are poorly understood. There are some special materials containing no metal elements that can also develop into nanowires from their oxide decomposition. Wang et al. [11,68,69] reported that SiO₂ largely enhanced Si nanowire growth (Fig. 7(a)). A model called oxide-assisted growth (OAG) was therefore proposed with evidence from experiments not only on Si but also on Ge [70] and III–V [71–73] semiconductor nanowire growth. As shown in Fig. 7(b), the presence of SiO₂ in the source significantly increases the yield of Si nanowire product. The Si nanowire product obtained using a powder source composed of 50% SiO₂ and 50% Si is 30 times larger than the amount generated by using a metal-containing target [11].

The OAG reaction is special because no metal elements or catalysts are involved either in the source materials or the nanowire itself. The starting material is oxide and the nanowires are in non-oxide form. In OAG using SiO, the nanowires are pure Si (not Si-oxide), and Si itself does not have a self-catalyst effect. This means that Si nanowires are formed by the assistance of Si-oxide. The OAG model has been tested by a simple experiment [74], which was carried out by simply sealing highly pure SiO powder or a mixture of Si and SiO₂ (1:1, Si reacts with SiO₂ to form SiO or Si_xO ($x > 1$) vapor phase) in an evacuated (vacuum <10 Torr) quartz tube and then inserting the tube into a preheated furnace (1250–1300 °C). No special ambient gas was needed. One end of the tube was left outside the furnace to generate a temperature gradient between the source material and the nanowire formation zone. After 20–30 min of annealing, a high yield of sponge-like Si nanowire product formed on the cooler parts of the tube where the

temperature was about 800–1000 °C. A similar thermal evaporation experiment was actually performed in 1950 [55,75]. Two kinds of materials were obtained at the temperature range of 800–1000 °C, one was a SiO product and the other one was labeled as “light brown loose material”. The loose materials were characterized by X-ray diffraction and determined to be Si structures [75]. The “light brown loose material” can be obtained routinely nowadays by thermal evaporation as Si nanowires. Unfortunately, the Si nanowires in the loose materials were not identified at the time of the initial experiments. The advantages of the OAG technique are (1) the nanowires are highly pure since no metal catalyst is involved and (2) doping of nanowires can be easily achieved because the experimental setup for OAG of Si nanowires is very similar to that of the laser ablation technique. Doping can be easily realized with the assistance of laser ablation of solid dopant materials during nanowire growth. Si nanowires fabricated by this method showed very uniform diameters (about 20 nm) and their lengths were over several hundred micrometers.

2.4. Metal-catalyzed molecular-beam epitaxy

Since 2000, MBE and CBE techniques have been employed to synthesize Si [15], II–VI [14] and III–V [13,16] compound semiconductor nanowires based on the VLS growth mechanism. MBE and CBE techniques provide an ideal clean growth environment, and the atomic structures, doping states and junctions (or heterostructures) can be well controlled. Combined with the VLS, these techniques are able to produce high-quality semiconductor nanowires. Different from other synthesis techniques, MBE works under ultra-high vacuum conditions. The mean free path of the source molecules under vacuum conditions of 10⁻⁵ Torr is about 0.2 m. The evaporated source atoms or molecules from the effusion cells behave like a beam aiming directly at the substrate (see Fig. 8). The growth, surface structures and contamination can be monitored *in situ* by reflection high-energy electron diffraction, Auger electron spectroscopy and other surface probing techniques. MBE has several advantages over other synthesis techniques: (1) the ultra-high vacuum can reduce contamination/oxidation of

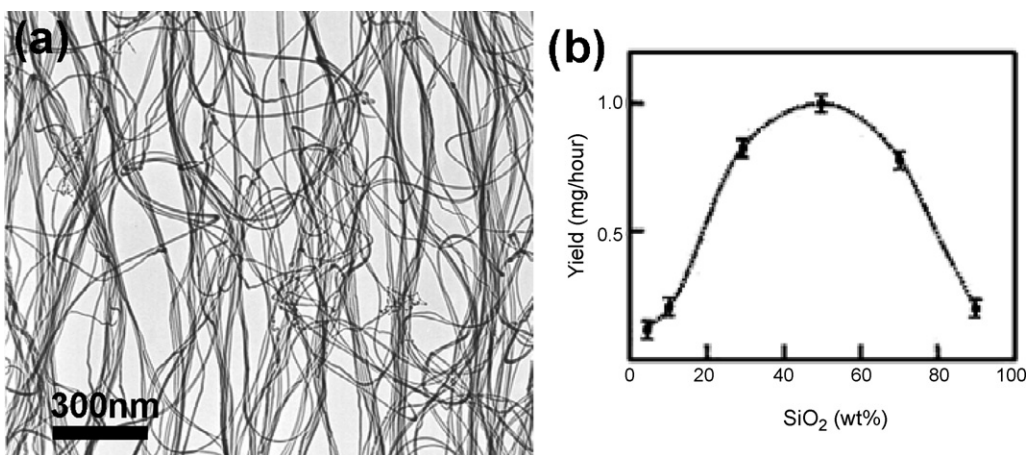


Fig. 7. (a) Si nanowires synthesized by oxide-assisted growth. (b) Yield of Si nanowires vs. the percentage of SiO₂ in the target [11].

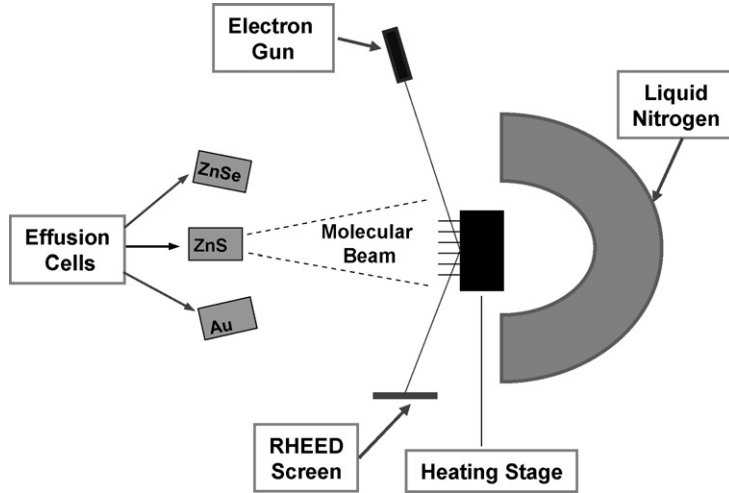


Fig. 8. A typical MBE growth chamber.

material surfaces; (2) the low growth temperature and the growth rate prevent inter-diffusion in the nanostructures; (3) *in situ* monitoring of growth is possible; (4) since all growth parameters can be adjusted precisely and separately, the intrinsic nanowire growth phenomena can be studied individually.

For a classical VLS reaction, the metal particles are essential for the catalytic decomposition of the precursors. For MBE growth, however, no molecules or precursors need to decompose. The function of the metal particles is twofold: (1) absorption of atoms from vapor phases or substrate surfaces. The driving force is to lower the chemical potentials of the source atoms and (2) precipitation or crystallization of the source materials at the particle-substrate interface. The preparation of the substrate surface is critical for growing high-quality nanowires. After wet-chemical cleaning, the substrate has to be deoxidized. Substrate de-oxidation is essential because the oxide layer on the substrate influences the nanowire growth direction. A poorly treated substrate results in random growth directions. The deoxidation temperature depends on the substrates used. For a GaP(1 1 1) substrate, for example, annealing at 600 °C is essential. For the growth of II–VI (e.g., ZnSe and ZnS) nanowires [14], the synthesis is carried out using compound-source effusion cells at temperatures above 500 °C. According to *in situ* observations of the reflection high-energy electron diffraction patterns during the growth, Au nanoparticles are in a molten state at this

temperature. In practice, Au nanoparticles are not necessarily molten droplets. In fact, the nanowires can grow at a temperature below the eutectic point. However, the deposition of the source atoms on the substrate surface becomes significant at a low temperature. Then, the surface diffusion becomes an essential mechanism. Excess adatoms are driven to the low energy state of the molten metallic particles or the molten interfaces at these particles.

The growth temperature is a critical factor for the formation of high-quality ZnSe nanowires. On the one hand, the deposition of ZnSe on the substrate is restrained when the substrate temperature is substantially higher than 300 °C. Therefore, almost no ZnSe deposition occurs on the fresh surface of the substrate (see Fig. 9(a)). On the other hand, a certain high temperature is needed in order to activate the Au-alloy particles on the substrate and to “catalyze” the growth of the ZnSe nanowires epitaxially on the substrate. Due to the surface melting effect, it is possible to grow ZnSe nanowires at a low temperature of about 390 °C. In this case, the deposition of ZnSe on the substrate surface is significant (Fig. 9(b)), and the quality of the nanowires is poor compared with the quality of nanowires grown at a higher temperature. These nanowires contain high-density defects, e.g., stacking faults and twinings. However, a too-high growth temperature results in coarsening of the Au catalyst and a low growth rate and, in turn, leads to non-uniform diameters of the ZnSe nanowires. The resulting growth rate of the nanowires is mainly determined by

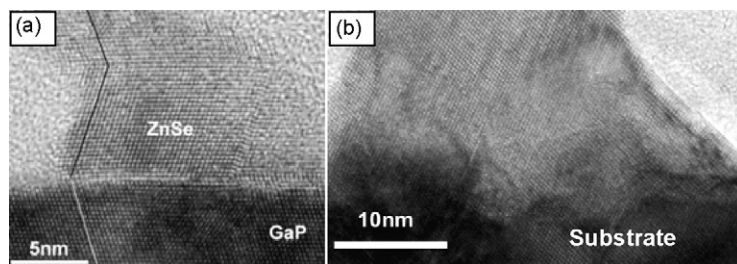


Fig. 9. TEM images of the interface structures at the substrate. (a) No deposition of the source materials on the substrate surface under a high growth temperature. (b) Deposition of the source materials on the substrate surface under a low growth temperature.

the ZnSe flux at a fixed temperature. At 530 °C, the growth rate of ZnSe nanowires is about 0.1 nm/s [14].

CBE is a hybrid form of molecular beam epitaxy. Different from MBE (using solid sources evaporated at high temperatures), gas sources are used (also called gas source molecular beam epitaxy). CBE works at an ultrahigh vacuum condition so that the mean-free paths between molecular collisions become longer than the source inlet and the substrate. The gaseous source materials are introduced (the gas transport is collision free) into the reaction chamber at room temperature in the form of a beam. From Au-catalyzed CBE, high-quality 1D heterostructure nanowires (InAs/InP) with diameters of about 40 nm have been fabricated [16]. Very thin InP barrier layers with thicknesses of 1.5 nm and excellent interface structures have been demonstrated by this method. The growth direction and defect density in the nanowires grown by CBE and MBE are influenced by several factors. Twinning (see Fig. 9(a)) or stacking faults are the main defects that very often occur in thicker nanowires and cause a change of the nanowire growth direction. For ZnSe nanowire growth, the growth temperature and the ratio of the source elements are the main reasons causing the defects. The defect density is also dependent on the growth direction. We have observed that [0 0 1] growth nanowires contain fewer defects compared with nanowires grown in other directions, and ultra-thin nanowires (diameter < 10 nm) generally contain few defects. The growth directions of ultra-thin II–VI compound nanowires are mainly determined by the diameters or the sizes of the catalysts and the growth temperature. The size-dependent and temperature-dependent growth directions and the interface structures of II–VI nanowires are discussed in Section 4.1 based on the estimation of the surface and interface energies of the nanowire nuclei.

2.5. Solution methods

The major advantages of the solution-based technique (in aqueous or non-hydrolytic media) for synthesizing nanomaterials are high yield, low cost and easy fabrication. The solution-based technique has been demonstrated as a promising alternative approach for mass production of metal, semiconductor and oxide nanomaterials with excellent controls of the shape and composition with high reproducibility. In particular, this technique is able to assemble nanocrystals with other functional materials to form hybrid nanostructures with multiple functions with great potential for applications in nanoelectronic and biological systems. The nanocrystals synthesized in aqueous media may often suffer from poor crystallinity, but those synthesized under nonhydrolytic conditions at a high temperature, in general, show much better crystal quality [76,77]. For the formation of nanowires from solution, several routes have been developed, such as metal-catalyzed solution-liquid-solid (SLS) growth from metal seeds [78–88], self-assembly attachment growth [89–94], and anisotropic growth of crystals by thermodynamic or kinetic control.

Many nanowires grown from solution methods largely rely on “structural directors”, including (1) “soft templates,” such

as surfactants and organic dopants and (2) “hard templates,” such as anodized alumina membranes [95–103] containing nanosized channels, track-etched polymer porous membranes, and some special crystals containing nanochannels. Through DC or AC electrochemical deposition, various materials can be introduced into the nanochannels of the hard template [100–103]. In some cases, vapor molecules may selectively diffuse into the channels because of special chemical properties of the nanochannel walls [103]. Without the assistance of structural directors, anisotropic growth of crystals induced by different surface energies can lead to the formation of elongated nanocrystals. However, the differences in the surface energies of most materials are not large enough to cause highly anisotropic growth of long nanowires. By adding surfactants to the reaction solution, some surfaces of nanocrystals can be modulated, i.e., the surfactant molecules selectively adsorb and bind onto certain surfaces of the nanocrystals and thus reduce the growth of these surfaces. This selective capping effect induces the nanocrystal elongation along a specific direction to form nanowires. The selective capping mechanism has been evidenced recently in many nanomaterials such as metal nanowires [104–109], metal oxide nanowires [110–115] and semiconductor nanowires [116,117]. Though structural directors are often used for the synthesis of nanowires, the actual growth process is poorly known. As a matter of fact, in many cases, the structural directors may not exist or the materials are self-constitutive templates. The formation mechanism of nanowires in solution is complicated and the selection and function of the structural directors require further and systematic investigation.

3. Growth mechanisms of nanowires

3.1. Metal-catalyzed growth

The most significant work on the mechanism of the unidirectional growth of semiconductor whiskers grown by VLS was published by Wagner and Ellis in 1965 [118]. The unidirectional growth of Si whiskers can be simply interpreted based on the difference of the sticking coefficients of the impinging vapor source atoms on the liquid (the catalytic droplet) and on solid surfaces. In principle, an ideal liquid surface captures all impinging Si source atoms, while a solid surface of Si rejects almost all Si source atoms if the temperature is sufficiently high. This classical VLS mechanism is still applicable to the growth of many nanoscale wires produced today. As schematically shown in Fig. 10(a), Au particles deposited on the surface of an Si substrate initially react with Si to form active Au–Si alloy droplets. The melting temperature of a Si–Au alloy particle is significantly decreased once its size is in the nanometer range [119]. During the initial reaction of the catalyst on a flat surface (see also Fig. 10(b)), the shape or the contact angle (β_0) of the droplet is determined by the balanced forces of the surface tension and the liquid–solid (LS) interface tension. The droplet has a radius, R , which can be described by $R = r_0/\sin(\beta_0)$ (r_0 is the radius of the contact area) [120,121]. The contact angle is related to the surface tension

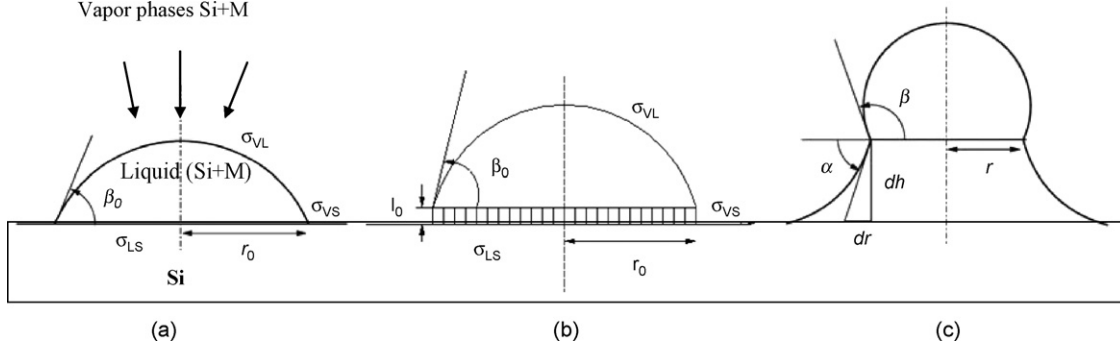


Fig. 10. Schematic of Au–Si droplets (a) formed on the substrate. (b) Initial growth of the nanowire. (c) The hillock shape of the nanowire root (from Ref. [121]; courtesy of Prof. T.Y. Tan).

and the line tension, τ , by a modified (a line tension is added) Young's equation [122]:

$$\sigma_1 \cos(\beta_0) = \sigma_s - \sigma_{ls} - \frac{\tau}{r_0}. \quad (3.1.1)$$

For a droplet of macroscopic size, the effect of the line tension can be ignored. For a nanosized droplet, the line tension should be considered. At the initial growth, when the nanowire's length, dh , increases, the radius of the contact area, dr , decreases. The inclination angle, α , of the nanowire flanks will increase ($\alpha = 0$ before growth). The inclination angle can be expressed as

$$\sigma_1 \cos(\beta) = \sigma_s \cos(\alpha) - \sigma_{ls} - \frac{\tau}{r_0}. \quad (3.1.2)$$

An increase in α is accompanied by an increase in β . The droplet will approach a spherical section. Since the contact area decreases with an increase in the nanowire length, the final radius of the nanowire should be smaller than the initial radius, r_0 (see Fig. 10(c)). The line tension (difficult to determine experimentally) strongly influences the catalyst contact area. A large line tension can result in hillock growth and thus stop the growth [120]. Using the minimization method of the system's

Gibbs free energy, Li et al. obtained [120,121]:

$$\sigma_{VL} \cos \beta_0 = \sigma_{VS} - \sigma_{LS} - \sigma_{LS}^c - \frac{\tau^c}{r^0}, \quad (3.1.3)$$

$$\sigma_{LS}^c = -l_0 \frac{k_B T}{\Omega} \ln \eta, \quad \tau^c = l_0 \sigma_{VS}, \quad (3.1.4)$$

where σ_{LS}^c is the effective surface tension, τ^c the effective chemical tension, l_0 the elementary thickness and η is the vapor source of the actual-to-equilibrium-pressure ratio. The chemical tensional is defined as: $\sigma^c = \sigma_{LS}^c + (\tau^c/r^0)$. Then, the general equation for a wire already grown to some length is $\sigma_{VL} \cos \beta_0 = \sigma_{VS} - \sigma_{LS} - \sigma^c$. The equilibrium condition of the VLS reaction is the balance among the various static factors in the system, the surface energies, the dynamic factors due to the growth of a crystal layer, and the chemical tension. The shape of an initially grown Si nanowire (due to the line-tension) is shown in the TEM image in Fig. 11(a). Based on the chemical-tension model, Li et al. predicted that different line-tension values can result in nanowire or nanohillock growth as shown in Fig. 11(b).

For Si whisker growth, a typical kinetic experimental result is the growth rate dependence on the whisker diameter. The larger the whisker diameter, the faster is its growth rate. This growth phenomenon is attributed to the well-known

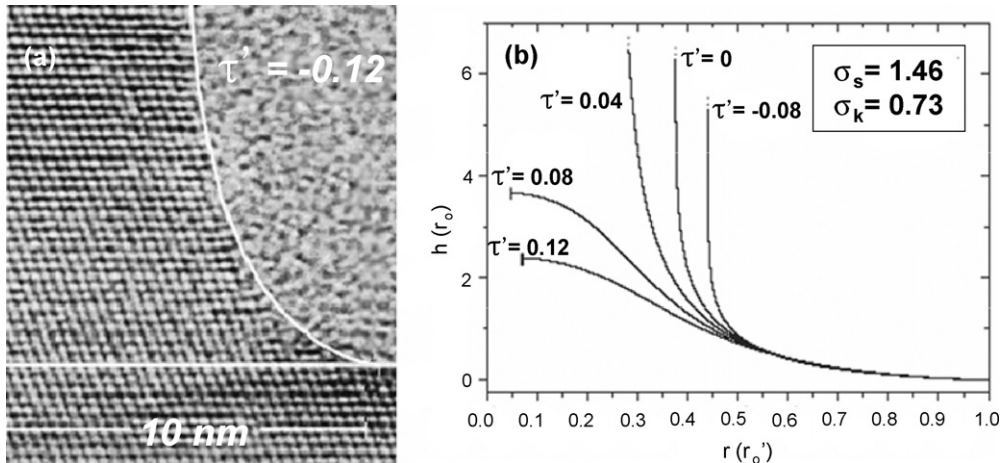


Fig. 11. (a) The shape of the initial growth of Si nanowires due to the line-tension. (b) Prediction of Si nanowire and nanohillock growth by the chemical-tension model for various line-tension values (from Ref. [120]; reproduced with permission from Springer Science).

Gibbs–Thomson effect, i.e., the decrease of supersaturation as a function of the whisker diameter [6]:

$$\frac{\Delta\mu}{kT} = \frac{\Delta\mu_0}{kT} - \frac{4\alpha\Omega}{kT} \frac{1}{d}, \quad (3.1.5)$$

or

$$\Delta\mu = \Delta\mu_0 - \frac{4\alpha\Omega}{d}, \quad (3.1.6)$$

where $\Delta\mu$ (also the driving force for whisker growth) is the effective difference between the chemical potentials of Si in the vapor phase and in the whisker. $\Delta\mu_0$ is the chemical potential difference for the plane boundary case, i.e., the whisker diameter $d \rightarrow \infty$. Ω is the atomic volume of Si; α the specific free energy of the whisker surface. Due to the change of the driving force (the chemical potential difference), Si whiskers with small diameters ($<0.1 \mu\text{m}$) grow very slowly. Obviously, there is a critical diameter at which $\Delta\mu = 0$ and the whisker growth stops completely. Those whiskers with diameters smaller than the critical diameter will stop growing. Thick whiskers grow faster than narrow ones [6]. At the thermodynamic equilibrium state, the stability of a liquid droplet depends on the degree of supersaturation. For a liquid droplet in its own vapor, the stability can be described by $d_{\min} = (4\alpha\Omega)/(kT \ln S)$. Here, S is the degree of supersaturation (the chemical potential $\Delta\mu = kT \ln S$).

Although Eq. (3.1.5) can well predict the VLS growth for most whiskers, however, it is not sufficient to describe the VLS reaction because (1) the droplet size may not be the same to that of the whisker and (2) the binary alloy nature (Metal–Si) of the droplet should be considered [123]. For the VLS reaction (Fig. 10(a)), four phases of materials are involved. They are Si and metal (M) vapor phases, the M–Si liquid droplet and the Si crystal. Because of the binary nature of the metal droplet, two minimum diameters are defined on the basis of thermodynamics by Tan et al. [123]: the minimum droplet diameter d_{\min}^l (equal to the critical diameter of the Si–M liquid droplet nucleated by the two vapor phases Si and M) and minimum wire diameter d_{\min}^s :

$$d_{\min}^l = \frac{4\alpha_{LV}\Omega_L}{KT \ln(P_{Si}/\bar{P}_{Si})} = \frac{4\alpha_{LV}\Omega_L}{KT \ln(P_M/\bar{P}_M)} \quad (3.1.7)$$

Here P_{Si} and P_M are partial pressures of Si and M. \bar{P}_{Si} and \bar{P}_M are unique values of the Si and M vapor phase pressures respectively allowing the two phases and the liquid phase with a flat surface to coexist under thermal equilibrium condition. The minimum Si wire diameter d_{\min}^s has a similar form which is equal to the critical diameter of a cylindrical Si crystal grown from the liquid Si–M droplet of diameter d_{\min}^l :

$$d_{\min}^s = \frac{2\alpha_{SV}\Omega_S}{KT \ln(P_{Si}/\bar{P}_{Si}^{eq})} \quad (3.1.8)$$

\bar{P}_{Si}^{eq} is the Si vapor phase pressure in the thermal equilibrium state. According to Eqs. (3.1.7) and (3.1.8), thermodynamically there is no absolute limit on the diameters of the Si–M droplet and Si wire. The diameters of Si wires can reach smaller sizes if there is no limit from the kinetic process in the VLS. Tan et al.

[123] have calculated the minimum radii of Si wires formed from Si–M systems based on appropriate phase diagrams and the interface energy α_{SV} . Smaller radii can be reached at lower growth temperatures. As illustrated in Fig. 12, the radii of some small Si nanowires have approached some effective limit set by the liquid composition.

Though the classical VLS reaction can still be extrapolated to explain the growth of most nanowires, ultra-thin nanowires (diameter $< 10 \text{ nm}$) of different materials show distinct growth behaviors. In the classical VLS reaction, it is believed that the catalyst is in molten state which absorbs the source materials to form a supersaturated liquid droplet (Fig. 13(a)). The LS interface structure is very critical to nanowire growth. At the LS interface, there is a region consisting of several layers of atoms in which atoms are in semi-molten state, i.e., atoms can move easily between the crystal lattice sites [124]. Atom precipitation occurs at the LS interface. The growth rate of the nanowires is determined by the supersaturation in the catalyst droplet ($\Delta\mu/kT$). Givargizov et al. [6,125] determined the whisker growth rate as a function of the driving force (supersaturation $\Delta\mu/kT$) and first empirically described their results by the relationship:

$$V = \frac{dL}{dt} = b \left(\frac{\Delta\mu_0}{k_B T} - \frac{4\Omega\sigma}{dk_B T} \right)^n, \quad (3.1.9)$$

where b and n (~ 2) are empirical fitting parameters. This relationship was later justified (numerically) by Givargizov using a 2D island nucleation-growth model [6]:

$$V = V_0 \exp \left(- \frac{\pi\Omega\eta^2}{3k \text{ Th } \Delta\mu} \right), \quad (3.1.10)$$

where η is the island edge energy density and h is the layer thickness. Again, these results indicated that in the VLS deposition, thick whiskers grow faster than narrow ones. But if the nanowire is thick enough, the growth rate will tend to be a constant.

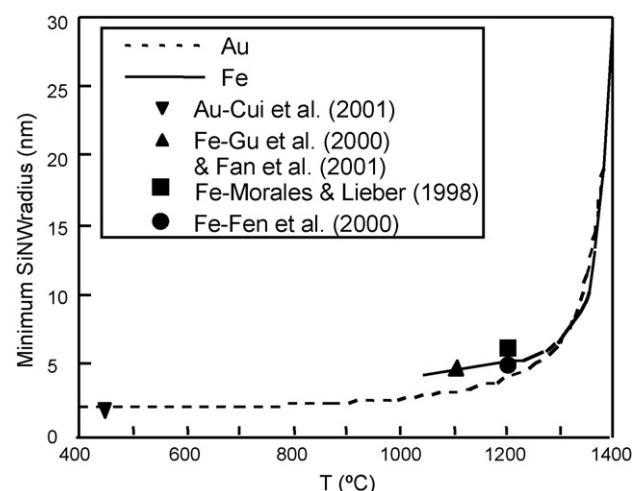


Fig. 12. Calculated curve using Eq. (3.1.8) for the Si–M systems. The surface energy used for the calculation is $\alpha_{SV} = 1610 \text{ erg/cm}^2$. Some available smallest radii of Si nanowires have approached the effective limits (from Ref. [123]; reproduced with permission from American Institute of Physics).

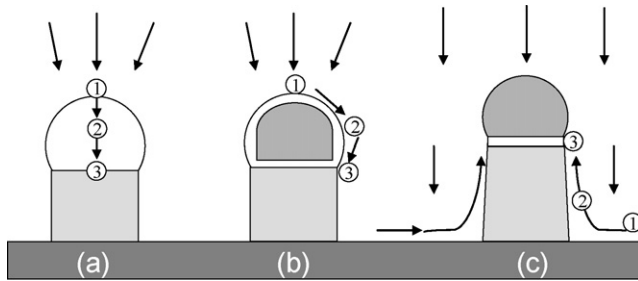


Fig. 13. Different diffusion models for the source atoms to incorporate into the growth front of the nanowire. (a) The classical VLS. (b) The metal droplet is in partially molten state. Its surface and interface are liquid, while the core of the droplet is solid. (c) The metal catalyst is solid, but the interface is liquid.

Wang et al. [52] have shown that in some cases the nanowire growth may be controlled by surface diffusion. In their diffusion-induced VLS model, molecules in the vapor phase are considered to first fall on the liquid surface and then diffuse along the surface to the LS interface and finally incorporate into the solid wire (see Fig. 13(b)). Then, the nanowire growth rate mainly depends on the surface concentration gradient ∇_s and the surface diffusion coefficient A_s . The relative growth rate V'_s is proportional to the inverse of the nanowire diameter, $V'_s = (\Delta L'_s / \Delta t) = (4A'_s \nabla'_s / d)$ [52,126,127]. The surface diffusion model becomes important for the growth at a low temperature. In addition to the direct impinging atoms, the source atoms may also arrive at the droplet by diffusion along the substrate surface and wire side surfaces (Fig. 13(c)). Nanowires formed by this model usually show tapering shape at their roots. At a relatively high growth temperature, however, this growth model should be inhibited because no adatom can stay at solid surfaces.

The measured growth rates V [6] of the VLS grown Si whiskers as a function of their diameters d is shown in Fig. 14(a). According to Eq. (3.1.9), $V^{1/n}$ and $1/d$ should be linear dependence, and this dependence matches the experimental results fairly well. The data can fit to straight lines for $n = 2$. The classical VLS model can predict the growth behaviors of whiskers well. However, the growth behaviors of ultra-thin nanowires may be totally different from that of whiskers. As an example, Fig. 14(b) illustrates the growth rates

for thin ZnSe nanowires (diameters < 100 nm) grown by Au-catalyzed MBE. It is very obvious that smaller nanowires have a higher growth rate compared to thicker ones [127,128]. The relationship between the growth rates and the diameters can be described by $V = C/d$ (C is a constant). This relation agrees with the growth model controlled by surface diffusion [126].

Different theories have been developed to explain the deviation of the growth behavior of ultra-thin nanowires from the classical VLS [129,130]. The main reason for the deviation of the growth rates is attributed to the change of the incorporation process and the diffusion paths of source atoms. For a thick nanowire, the surface diffusion contributes insignificantly to the growth rate because the ratio of cross-section area to the circumference is large. For an ultra-thin nanowire, however, the surface diffusion becomes significant. Especially when the growth temperature is low and the metal catalyst becomes solid (or partially solid), the interface between the catalyst and nanowire may still be in semi-melting state. This is similar to the case of a grain boundary whose melting temperature is always lower than that of its bulk crystals. It is known that grain boundaries are fast channels for atomic diffusion. At a certain temperature the atoms at the interface between Si and metal may be in partially molten state [51]. Therefore, at a low growth temperature, a solid metal catalyst can also lead to growth of ultra-thin nanowires through surface diffusion since the interface is still active, while in this case, the growth of a thick nanowire (a large solid catalyst) through interface diffusion should be difficult. The growth rates of ultra-thin nanowires controlled by surface diffusion are proportional to the inverse of the diameters. Recently, Kodambaka et al. [54] have demonstrated by *in situ* TEM observation that solid catalysts can lead to Ge nanowire growth.

At the same growth condition, the melting temperatures of metal catalysts are size-dependent. On the one hand, small catalysts have lower melting temperatures due to the nanosize effect. On the other hand, due to the Gibbs–Thomson effect, decreasing the diameter of the catalyst droplet results in a lower solubility of the source atoms and thus shifts the melting temperature of the catalyst (see also the phase diagram in Fig. 1(b)). Therefore, when the growth temperature falls below

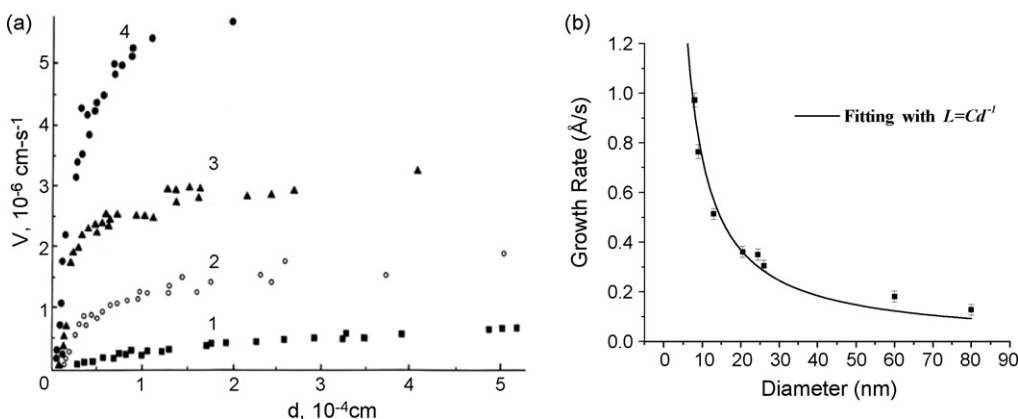


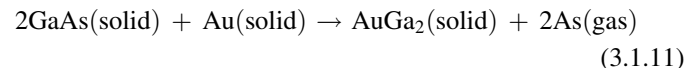
Fig. 14. The growth rates of (a) VLS Si whiskers (from Ref. [6]; reproduced with permission from Elsevier Science) and (b) VLS ZnSe nanowires plotted as a function of diameters.

the eutectic point, the metal catalysts at the tips of nanowires with relatively small diameters became solid first, while those catalysts with relatively large diameters remained in the liquid state. This interesting phenomenon has been observed by *in situ* TEM [54].

For Si or Ge nanowire growth, Au catalysts are liquid or solid solution. For compound semiconductors, such as GaAs, the structure and chemical composition of Au catalysts are complicated. Fig. 15(a) and (d) shows the Au particles formed on a GaAs(1 1 1) surface after annealing at 530 °C. Fig. 15(a) is an enlarged image showing the typical hexagonal shape of an Au catalyst in which 2D moiré patterns are clearly visible. The selected-area electron diffraction (SAED) pattern (Fig. 15(b)) taken from this particle illustrates clearly strong diffractions of GaAs (along the [111] zone axis) surrounded by satellite spots which come from the double diffraction effect that occurs when the particle and the substrate have a certain orientation relationship. The structure of the catalysts has been identified to be AuGa₂ (face center cubic (FCC), space group *Fm3m*, lattice parameter $a = 0.6073$ nm) by electron diffraction and TEM image simulation [131]. The moiré fringes are due to the overlap between GaAs substrate and AuGa₂ particles. The AuGa₂ catalysts are single crystalline if their sizes are small. Two grains often form (marked by I and II in Fig. 15(a)) in a large catalyst. According to the SAED patterns in Fig. 15(b) (along the [1 1 1] zone axis) and (c) (along the [1 1 2̄] zone axis), only one AuGa₂ grain epitaxially forms on the substrate with orientation relations of [1 0 0]_{GaAs}//[1 0 0]_{AuGa₂} and [0 1 0]_{GaAs}//[0 1 0]_{AuGa₂}.

For Au–GaAs system, the catalysts reacted with the substrate during annealing and formed sharp interfaces between the catalyst and GaAs substrate. Fig. 15(e) is the cross-sectional view of an individual AuGa₂ catalyst. The orientation relations between AuGa₂ grain II and the substrate agree well with the SAED results. The chemical composition of the catalysts was characterized using electron energy-loss spectroscopy and X-ray energy dispersive spectroscopy, and the results indicated that the catalysts consisted of Au and Ga, but no As was detected in the catalysts. The interface of the catalyst at the substrate (about 7.4% of mismatch) was (1 1 1) at which interfacial dislocations occurred. It was interesting to note that

only AuGa₂ binary alloy formed by annealing, and arsenic did not participate in the nanowire growth. The reaction of the catalysts can be described as



In this reaction, arsenic is extracted from the substrate during the formation of AuGa₂ alloy. Then, arsenic may diffuse out of the catalyst surface and evaporate [192,193]. For large catalysts, the Ga rich form (AuGa₂) of the Au–Ga alloy remains at the tips of ZnSe nanowires (see Fig. 15(f)). However, the solubility of Ga in an ultra small catalyst is largely reduced, and only Au solid solution (in FCC structure of Au) is formed (Fig. 15(g)). The change of Ga solubility in the catalyst is due to the well-known Gibbs–Thomson effect. Due to the change of the solubility, the melting point of the catalyst shifted according to Au–Ga phase diagram.

On the surfaces of ZnSe, a similar reaction occurred when Au catalysts reacted with ZnSe to form Zn–Au alloy droplets and Se evaporated (see Fig. 16(a)). According to the Zn–Au phase diagram, a Au rich Au–Zn alloy should form. As observed by TEM, the catalysts were single crystalline FCC structures, same to that of Au. The interaction between Au nanoparticles and ZnSe or ZnS buffer layer (grown on GaAs(1 0 0) substrate) displayed interesting features. Thermal annealing always induced the movement of the droplets along a certain pair of ⟨1 1 0⟩ direction (see the inset in Fig. 16(b)) and formed parallel trenches on their path [128]. Fig. 16(b) shows the SEM image of the trenches on a ZnSe substrate surface caused by the sliding of Au-catalysts. Separate atomic force microscopy (AFM) imaging done on this sample revealed that the nanotrenches are quite uniform in width and depth with typical width of ~20 nm and depth of a few nanometers. Similar thermal annealing resulted six symmetric ⟨1 1 0⟩ oriented nanotrenches on the sample grown on a GaAs(1 1 1)B substrate. These results together indicated that some specific ⟨1 1 0⟩ directions were the preferred orientation of the nanotrenches.

The formation of these nanotrenches is believed to be due to the special interaction between Au particles and the substrate.

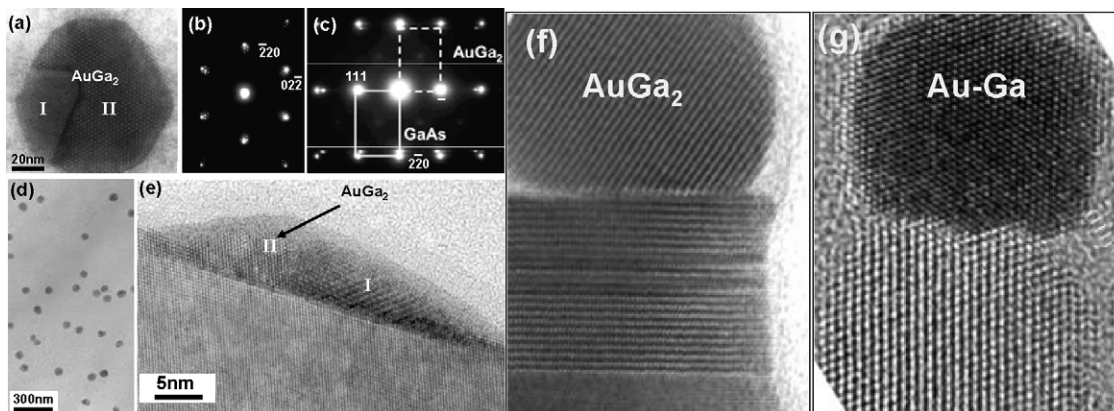


Fig. 15. (a) Plan-view TEM image of Au catalysts formed on GaAs substrate surface by the annealing treatment. (b) and (c) SAED patterns taken along the [1 1 1] and [1 1 2̄] zone axes of the catalyst, respectively. (d) Morphology of Au catalyst. (e) Cross-sectional HRTEM image (along the [1 1 0] direction) of the catalyst formed on the substrate. (f) AuGa₂ phase in a large catalyst. (g) Au–Ga solid solution in a small catalyst in FCC structure.

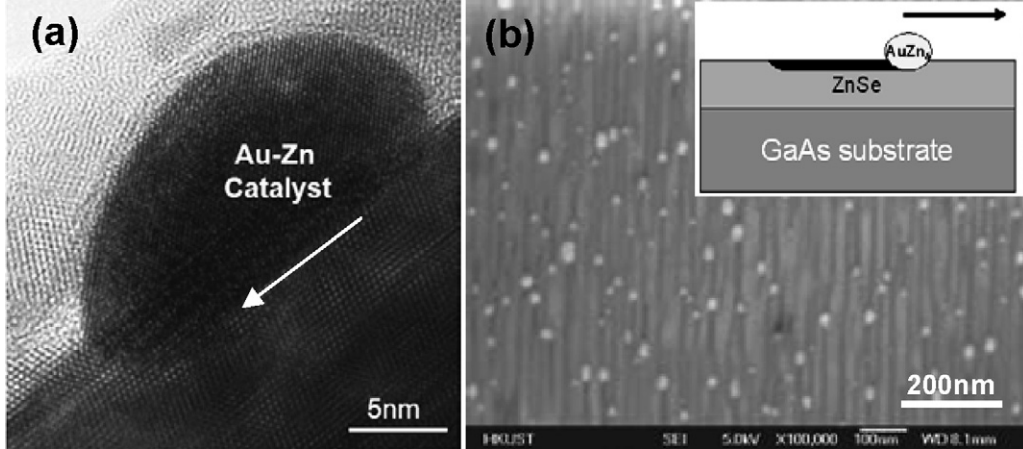


Fig. 16. (a) Au–Zn nanocatalyst formed on ZnSe substrate. (b) Sliding of the catalysts by annealing results in trenches along the [1 1 0] direction *n* the substrate surface.

By annealing at a high temperature, Au droplets first react with the ZnSe thin film to form AuZn_x (with x less than 14%) alloy droplets while the other by-products are vaporized. In this reaction, the resulting AuZn_x alloy droplets fall into the ZnSe buffer by a fraction of their size until the composition of the alloy is saturated. Further annealing will lead to migration of the alloy droplets along a most preferred direction accompanying the decomposition of ZnSe along the path. The observed specific [1 1 0] direction of the trenches can be explained by the fact that the bonding between {1 1 0} planes are the weakest for most of the zinc blende structures. During the migration, the AuZn_x alloy droplets will act as a catalyst for decomposing the ZnSe along the path. Both Zn and Se decomposed from this reaction most likely are vaporized, so nanotrenches are developed along the path. The perfect alignment of these nanotrenches make them potentially useful as a common template for fabricating 1D structures of other materials.

3.2. Vapor–solid growth

Without the aid of metal catalysts, the vapor–solid (VS) growth has been mainly used to synthesize metal oxide and some semiconductor nanomaterials. It is often called self-catalytic growth since the nanostructures grow directly from vapor phases. Plausible growth mechanisms such as the anisotropic growth, defect-induced growth (e.g., through a screw dislocation), and self-catalytic growth have been suggested based on electron microscopy studies. According to the classical theories of crystal growth from liquid or vapor phases, the growth fronts play a crucial role for the deposition of atoms. There are two kinds of microscopic surfaces: (1) rough surfaces on which atoms of about several layers are not well arranged. Deposition of atoms is relatively easy compared to a flat surface and crystal growth can continue if enough source atoms are continuously provided; (2) atomically flat surfaces on which atoms are well arranged. Atoms from the source have a weak bonding with flat surfaces and can easily return to the liquid/vapor phase. Atoms deposition occurs only on the atomic steps.

There are three ways to generate atomic steps on a flat surface: (1) nucleation of new two-dimensional islands which is difficult because the nucleation barrier is high, and there is almost no super-cooling. The islands will be exhausted eventually (see Fig. 17(a)); (2) screw dislocations which generate atomic steps to help atoms to deposit continuously (Fig. 17(b)); and (3) twining structures which contain ditches at the cross of two grain surfaces. Atoms deposit at the ditches resulting in atomic steps along twining surfaces. The resulting growth can be continuous along the direction of the twining plane (Fig. 17(c)). Followings are important factors for the nanocrystal growth in the VS process.

3.2.1. Internal anisotropic surfaces

Because of anisotropic properties of different surfaces in a crystal, such as the preferential reactivity and binding of gas reactants on specific surfaces and all crystals tend to minimize their total surface energy, rod- or wire-like shapes are frequently resulted. However, the degree of the anisotropic properties of crystals is not significant large, highly anisotropic growth (i.e., the length-to-diameter ratio >100) of nanocrystals at or near the thermal equilibrium state is not expected.

3.2.2. Crystal defects

Screw dislocations (the well known Burton–Cabrera–Frank theory) are known to significantly enhance the crystal growth of metals and some molecular materials [132]. This classical mechanism is based on the fact that the growth of a crystal proceeds by adding atoms at the kink sites of a surface step. Kink sites always exist on the steps even at the thermal equilibrium state. Due to the advance of the kink along the surface by the addition of atoms, the crystal grows perpendicularly to the surface. In thermal equilibrium state, a perfect crystal should eventually contain no surface steps. Then, the growth of a perfect crystal depends on the nucleation of surface steps. For the growth of a real crystal, however, the growth rate is much faster than that predicted for a perfect crystal because real crystals contain defects, e.g., dislocations and twins. A dislocation cannot terminate inside a perfect

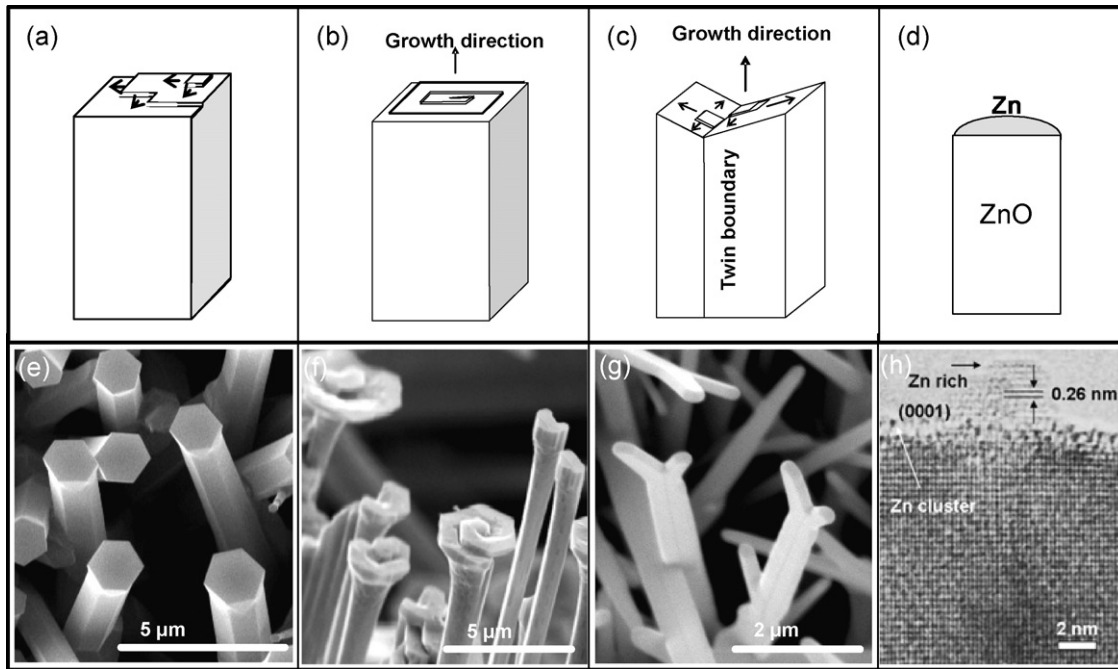


Fig. 17. (a) Nanorods formed due to anisotropic growth of ZnO crystals. (b) Unidirectional growth of ZnO single crystals due to screw dislocation. (c) Growth induced by twining. (d) Self-catalytic growth of ZnO nanowires by Zn droplets. (e) ZnO crystals contain no catalysts and defects. (f) ZnO whiskers growth due to dislocations. (g) ZnO bi-crystal growth due to twining. (h) Zn or Zn-rich phase observed on the tips of ZnO nanowires (image (h) from Ref. [62]; reproduced with permission from American Physical Society).

crystal. They can terminate on a defect inside the crystal or on a surface. If a dislocation ends on a surface and its Burgers vector has a component normal to the surface (the screw component), a step forms starting from the emerging point of the dislocation. Leading by the dislocation, steps can winds into a spiral, and the growth of the crystal is largely enhanced without the need of nucleation for fresh surface steps. There are many reasons for the formation of a dislocation in a crystal. For Si nanowires, oxygen atoms may cause the nucleation of a dislocation [133]. It has been frequently observed that screw dislocations are associated with growth of crystal in the dendrite or whisker geometries. In ultra-thin nanowires, so far no screw dislocations have been evidenced. However, in thick wires, for example ZnO nanowires (diameters > 200 nm), unidirectional growth induced by dislocations in VS growth mode has been observed (Fig. 17(f)). The spiral feature at each whisker tip is obviously due to the steps generated by a screw dislocation. In thin ZnO nanowires grown by the VS growth, however, no screw dislocations existing at the core of the nanowires have been found.

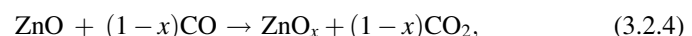
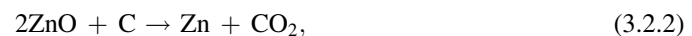
3.2.3. Self-catalytic growth

Self-catalytic growth has been proposed based on the fact that metal vapor, for example Zn, can be extracted from ZnO vapor phase by heating ZnO powder in vacuum. When ZnO is sealed in an evacuated quartz tube (10^{-1} to 10^3) and heated at a temperature above 1100 °C, ZnO may decompose into Zn and oxygen as described in Eq. (3.2.1) [62]. Zn droplets are easily observed on the inner walls of the tube where the temperature is about 500 – 600 °C. Under a normal atmosphere condition, however, no obvious decomposition of ZnO is observed, and

thus no nanowires can be generated by heating ZnO power at a high temperature.



Another way to generate Zn or Zn oxide vapor phases is to add carbon powders into ZnO solid source, mass production of ZnO nanowires and nanoribbons can easily realized in the temperature range of 500 – 800 °C. In this case, Zn or Zn suboxide play a crucial role for the nucleation of ZnO nanostructures [67]. This is because that at a high temperature condition ($T > 1100$ °C), carbon reduced ZnO into Zn or Zn suboxides by the following reactions:



The carbon powder might directly react with ZnO (for the case of the sealed quartz tube) or first react with oxygen to form CO (for the case of the open-end quartz tube). Zn and Zn suboxides have low melting temperatures (approximately 419 °C for both Zn and ZnO_x , where $x < 1$) compared to that of ZnO (1975 °C) and should be in vapor phases at 1100 °C. At the low temperature site, Zn vapor generated by reactions (3.2.2) and (3.2.3) will condense on the inner wall of the quartz tube forming liquid droplets, which are ideal catalysts for ZnO nanowire growth through the VLS mechanism. Carrying gases are not necessary for the formation of ZnO nanostructures. Temperature is the critical experimental parameter for the

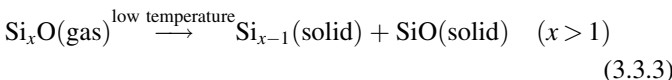
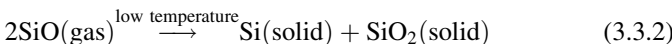
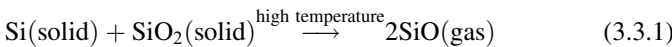
formation of different morphologies of ZnO nanostructures [67].

With the presence of carbon, during the reaction in an open-end quartz tube (open one end of the tube to air), Zn vapor or droplets can be partially oxidized forming suboxides, which generally have low melting temperatures. The formation of the suboxides is because the amount of oxygen contributing to the reaction in the open-end quartz tube is limited. This condition is reasonable since Zn droplets co-exist with ZnO nanowire products in the early stage of the nanowire formation. Either Zn droplets or vaporized Zn suboxide droplets could be the nuclei for ZnO nanowires. Similar to the oxide-assisted growth mechanism (to be discussed in the next section), Zn suboxides are more reactive than ZnO and may largely enhance the deposition of Zn oxides at the tips of ZnO nanowires during growth. Due to further oxidation of Zn or Zn suboxides, the concentration of oxygen in the droplets/tips increases, and thus ZnO deposits on the interface between the droplets and substrate, resulting in the growth ZnO nanowires. Zn and Zn-rich phases have been observed by HRTEM on the ZnO nanowire tips grown by the VS growth (Fig. 17(h)) [62]. Moreover, Zn-ZnO core–shell nanobelts and tubes were also observed [134]. Though the self-catalytic growth mechanisms of the VS growth are complicated and unclear, many metal oxide nanowires and interesting morphologies of nanostructures have been produced by this method [135,136].

3.3. Oxide-assisted growth

3.3.1. Kinetics and reactivity of silicon oxide in nucleation and growth

Compared to the VLS mechanism, the nucleation and growth of Si nanowires from the oxide-assisted mechanism appears to be novel. The oxide-assisted nanowire growth is described by reactions (3.3.1), (3.3.2) and (3.3.3). The vapor phase of SiO and Si_xO ($x > 1$) generated by the thermal effect (thermal evaporation or laser ablation) is the key factor:



Silicon oxide clusters generated and present in the gas phase in Si nanowire synthesis play an important role in the nucleation and growth. Small silicon oxide clusters Si_nO_m ($n, m = 1–8$) studied both experimentally and theoretically [137–139,262,270,271,274] revealed that silicon monoxide-like clusters adopt planar and buckled-ring configurations, while oxygen-rich clusters are rhombuses arranged in a chain with adjacent ones perpendicular to each other. Si suboxide clusters are highly reactive to bond with other clusters and prefer to form Si–Si bonds [141]. By analysis of the highest occupied molecular orbitals (HOMOs) and the lowest unoccupied molecular orbitals (LUMOs) of silicon oxide clusters, the reactivity

for them to form the Si–Si, Si–O, and O–O bonds were revealed according to the well-known frontier orbital theory [142]. The HOMO–LUMO gap for (SiO)_n clusters are 2.0–4.5 eV, much lower than those for (SiO)₂ species, indicating higher chemical reactivity of (SiO)_n clusters. The HOMO mainly localizes on the Si atoms at the cluster surface, making these regions the reactive. As the O ratio is less than about 0.62, the reactivity to form a Si–Si bond of two silicon oxide clusters is remarkably larger than to form a Si–O or O–O bond [141], as shown in Fig. 18. The combination of these clusters might occur easily through the Si–Si bonding.

The richer the Si atoms in the cluster, the higher will be the chance for them to form a Si–Si bond. However, the cohesion energy per atom of the silicon-rich clusters is much higher, indicating a smaller chance of their presence in the gas phase. The optimum ratio of Si atom to O atom in the silicon suboxide clusters to achieve the highest yield and formation of Si nanowire should be close to 1, as also observed experimentally (about 49 at.% of O) [40]. Our recent experiment using silicon monoxide has given the largest yield of Si nanowires. It is worthwhile noting that there are also experimental reports on the formation of the crystalline phase of Si nanoclusters from the deposition of silicon-rich oxide [140,143].

The nucleation of Si nanocrystals could be expected to take place via the combination of small Si suboxide clusters. The formation of Si core begins at $n = 3$ is shown in Fig. 19 [144]. As shown in the figure, (1) a Si core (represented by the open circles containing stars surrounded by a silicon oxide sheath is involved; (2) the Si–Si bonds prefer to form in the center rather than at the cluster surface so as to reduce the strain caused; (3) most of the Si atoms in the Si core have three or four coordinates with Si–Si–Si bond angles close to 109° (the value found in silicon crystal), which is quite different from that of pure Si clusters of the same size [145]; (4) with increasing cluster size, the size of the Si core increases and the fraction of

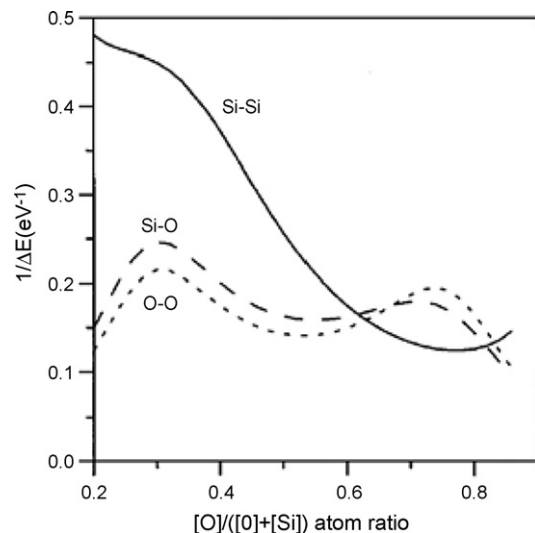


Fig. 18. The inverse of the energy difference $\Delta E = \text{LUMO}(\text{electron acceptor}) - \text{HOMO}(\text{electron donor})$ and thus the reactivity (proportional to the inverse of the energy difference) for the formation of a Si–Si bond, a Si–O bond, or an O–O bond between two silicon oxide clusters as a function of the Si:O ratio [141].

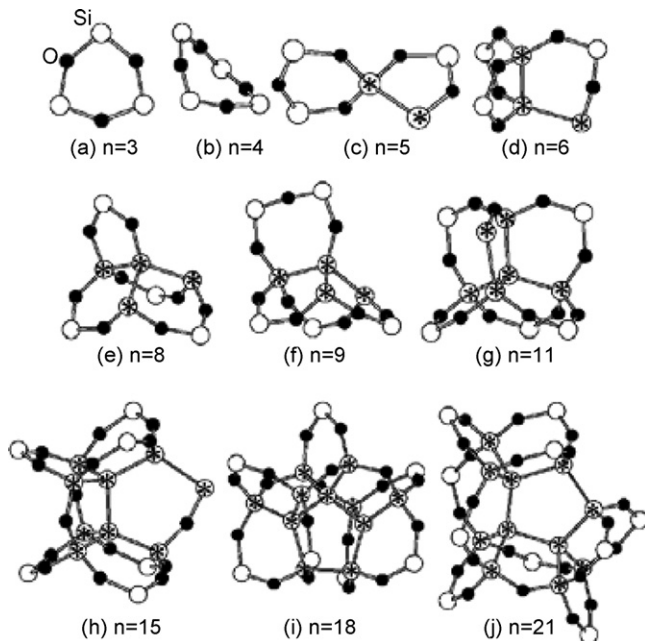


Fig. 19. The most favorable structures of silicon monoxide clusters (SiO_n) for $n = 3\text{--}21$ [144].

Si atoms with three and four coordinates increases correspondingly, making the cluster more stable; and (5) starting at $n = 18$ all of the Si atoms in Si cores are four-coordinated, indicating the formation of sp^3 Si cores similar to the configuration in the Si crystal. Fig. 20 depicts the binding energies of $(\text{SiO})_n$ clusters containing Si cores as a function of n , together with those containing buckled structures. It is clear that: (1) the configurations containing Si cores become energetically more favorable than the buckled structures for $n = 5$ and larger and (2) the cluster becomes increasingly more stable with increasing Si core size. As the two structures from $n = 5$ to $n = 8$ in Fig. 20 are close in energy, we further estimate their relative population at 900 °C (the growth temperature of Si

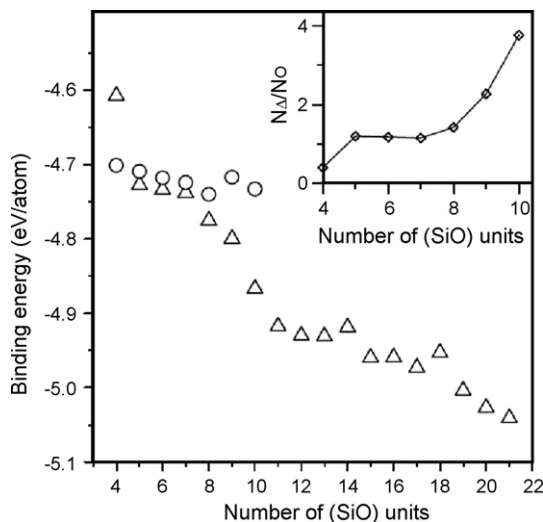


Fig. 20. Binding energy (eV/atom) of $(\text{SiO})_n$ clusters vs. n . The up triangles are $(\text{SiO})_n$ with the Si-cored structure surrounded by a silicon oxide sheath, and open circles are those with buckled-ring structure. The inset shows the relative population of the former (N_Δ) and the latter (N_0) structures at 900 °C.

nanowires [146]) by assuming the process is at equilibrium and described by the Boltzmann factor $\exp(-E/kT)$, where k is the Boltzmann's constant, E the energy difference, and T is the temperature in Kelvin. The results shown in the inset in Fig. 20 confirm that the structures containing Si cores still play the major role at such a high temperature starting at a size as small as $n = 8$. The formation of sp^3 Si core inside the silicon oxide clusters contributes to the nucleation of the Si nanocrystals. Because of their high chemical reactivity, a combination of these clusters may easily take place, forming clusters with a large sp^3 Si core via subsequent reconstruction and O migration from the center to the surface of the clusters. The crystalline Si cores thus formed can act as nuclei and precursors for subsequent growth of Si nanostructures.

Fig. 21 shows three different isomers of the $(\text{SiO})_{21}$ cluster with an O atom locating in different sites from the center to the surface of the cluster. The most stable configuration is the one with O located on its surface, and the total binding energy is 211.74 eV. However, the binding energy decreases as the O atom moves from the surface into the cluster. The O atom could migrate from the center of the silicon monoxide cluster to its surface via bond switching. For the $(\text{SiO})_5$ cluster, the estimated migration barrier is about 1.79 eV. The high strain involved in the large $(\text{SiO})_n$ cluster may cause the migration of O atom from the inside to the surface, leading to the formation of a Si core. The nuclei containing a Si core would grow larger with the assistance of O diffusion from the core to the surface layer during deposition.

In an experiment using SiO powder or a mixture of Si and SiO_2 powder as the source, the evaporated $(\text{SiO})_n$ clusters deposited on a substrate would be anchored due to their high reactivity at Si sites. The deposited clusters would act as the nuclei to absorb $(\text{SiO})_n$ clusters from the vapor because of their

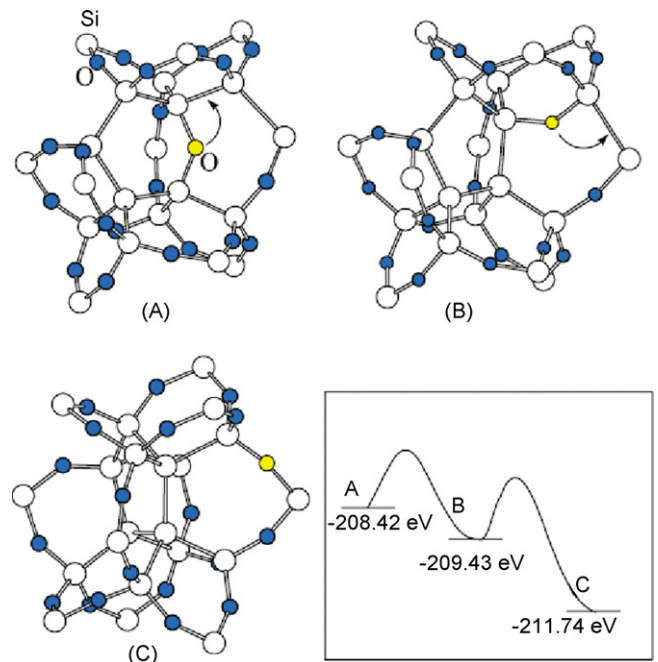


Fig. 21. Possible path of O atom migration from the center of a $(\text{SiO})_n$ cluster to its surface: (a) $(\text{SiO})_5$ and (b) $(\text{SiO})_{21}$ [144].

remaining reactive Si atoms facing outwards from the substrate. A Si core would start to form at a size of $n \sim 5$. The nuclei containing a Si core would grow larger with the assistance of O diffusion from the core to the surface layer during deposition. The O diffusion length depends on the temperature and the crystallographic orientation of the crystalline core formed, leading to the formation of Si nanowires with different crystalline orientations such as $\langle 1\ 1\ 0 \rangle$ and $\langle 1\ 1\ 2 \rangle$, as observed in our experiments [146]. The above process may be similarly responsible for the ready formation of Si nanocrystals in the sp^3 configuration from amorphous SiO [147].

The nucleation of Si nanoparticles has been observed to occur on the substrate due to the decompositions or precipitation of Si-rich oxide [68,69]. All nuclei are clad by shells of silicon oxide. The precipitation, nucleation and growth of Si nanowires always occur at the area near the colder region, which suggests that the temperature gradient provides the external driving force. The formation of Si nanowire nuclei at the initial growth stage is revealed in Fig. 22(a) and (b), in which some nanoparticles pile up on the matrix surface soon after the start of the decomposition of SiO. Notably, the nanowire nuclei that stand separately with their growth direction normal to the substrate surface undergo fast growth (Fig. 22(c)). Each nucleus consists of a Si crystalline core and an amorphous (silicon oxide) outer layer. Fig. 22(d) and (e) are the model schematically showing this nucleation and initial growth of Si nanowires from Si-oxide. Different from the VLS mechanism, no metal catalysts or impurities exist at the tips of the nuclei. The key point for the formation of the nanowires is the fast growth of the nuclei in the $\langle 1\ 1\ 2 \rangle$ orientation of the Si cores assisted by a thin Si-oxide layer on the tip. Therefore, only those nuclei with their growth direction of $\langle 1\ 1\ 2 \rangle$ direction normal to the substrate surface undergo fast growth. Since the formation of the nanowire nuclei is controlled by the self-decomposition of SiO, the diameters of the nanowires are uniform. As observed by electron diffraction and imaging, the growth direction of Si nanowires from the oxide-assisted method are along the $\langle 1\ 1\ 2 \rangle$ direction [68].

The catalytic effect of the Si_xO ($x > 1$) layers on the nanowire tips is an important driving force for the nanowire growth. Among the number of different forms of Si sub-oxides,

some of them are very reactive. The materials at the Si nanowire tips (similar to the case of nanoparticles) may be in or near their molten states. This is because that the surface melting temperatures of nanoparticles can be much lower than that of their bulk materials. For example, the difference between the melting temperatures of Au nanoparticles (2 nm) and Au bulk material is over 400 °C [148]. The atomic absorption, diffusion, and reaction are thus largely enhanced at the tips.

3.3.2. Effect of defects in 1D growth

Different from the VLS mechanism, the tips of Si nanowires from oxides contain no metal droplets. HRTEM investigations show that the defects and silicon oxide outer layers existing at the nanowire tips may play important roles for the formation and growth of Si nanowires. Fig. 23(a) illustrates the typical tip structure. Most tips are round and covered by a thin Si oxide layer of about 2–3 nm. A high density of stacking faults and micro-twins exists in the Si crystal core near the tip. Most stacking-faults and micro-twins are along the axis of the nanowire in $\langle 1\ 1\ 2 \rangle$ direction. Based on our investigation, we believe that Si nanowires from the oxide-assisted growth are determined by several factors, such as defects, lower melting temperature at the tips, SiO_2 component formed in the shells and retarding the lateral growth of nanowires, charging effect at the tips and relativities of Si sub-oxides. Among these facts, we believe that the defects and the catalytic effects of SiO_x are important for the nanowire nucleation and growth.

The main defects in Si nanowires are stacking faults and nano-twins along the nanowire growth direction of $\langle 1\ 1\ 2 \rangle$, which normally contain easy-moving $1/6\langle 1\ 1\ 2 \rangle$ and non-moving $1/3\langle 1\ 1\ 1 \rangle$ partial dislocations. As discussed for the vapor-solid growth mechanism, dislocation and micro-twins can significantly enhance the growth of the crystals. For the nano-twins at the nanowire tips, atoms deposited at the ditch results in atomic steps along the twining surface. The resulting growth direction is along the twining plane, i.e., along the $\langle 1\ 1\ 2 \rangle$ direction. The presence of these defects at the tip areas should result in the fast growth of Si nanowires since dislocations and twins provide enough atomic steps and kinks for the deposition of Si atoms. On the other hand, the melting temperatures at grain boundaries or interfaces are generally

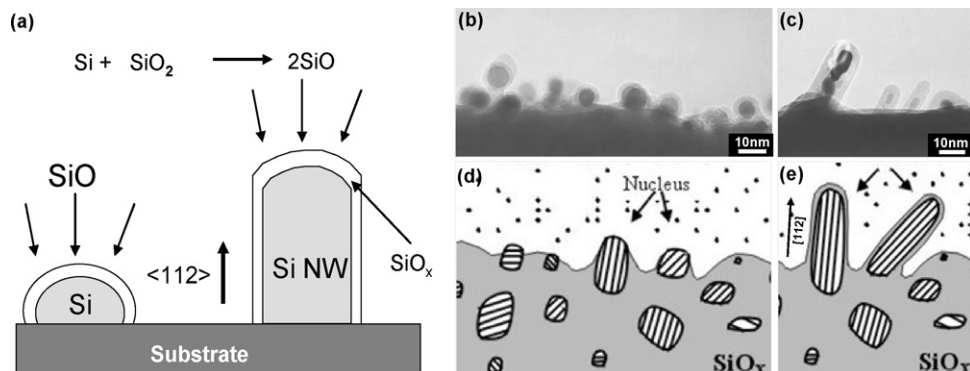


Fig. 22. (a) The mechanism of the Si nanowires from oxide. (b) TEM image of Si nanoparticles precipitate from the decomposition of SiO matrix. (c) The nanoparticles in a preferred orientation (e.g., $\langle 1\ 1\ 2 \rangle$) grow fast and form nanowires. (d) and (e) The model for the nucleation and initial growth of Si nanowires from Si-oxide [27].

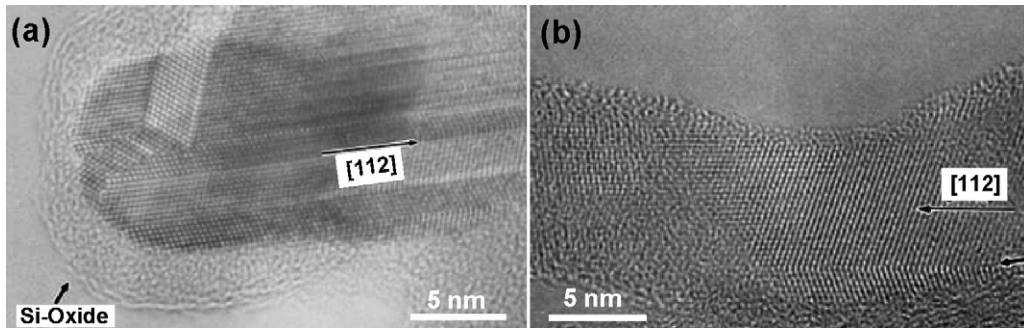


Fig. 23. (a) The tip structure of an individual Si nanowire from oxide-assisted growth. (b) Si nanowires grown along the $\langle 1 \ 1 \ 2 \rangle$ direction. Defects such as micro-twins (marked by the arrow) along the wire axis (marked by the arrow) are frequently observed.

lower than that of the bulk materials. Though the nanowire tips contain a high density of defects, most of Si nanowires grown by the oxide-assisted growth in certain growth temperature contained much low density defects. This may be attributed to the annealing effect since the nanowires were grown at about 1000 °C. Residual defects in the nanowires may be dismissed by moving out the surfaces of the nanowires or by re-crystallization and grain grow. The growth temperature of Si single crystalline nanowires was high enough for the re-crystallization to occur.

3.3.3. Effect of external electrical field in 1D growth

During the vapor condensation process, latent heat is released and transferred to the surroundings. The tip of a Si nanowire may be at a higher temperature in order to achieve a sufficient rate of heat transfer. Assuming that latent heat is released only at the tip and that an electric field exists at the tip due to charge accumulation, latent heat and electrostatic energy become the two main heat sources. Cheng et al. have systematically studied the electrical field, temperature and pressure effects at Si nanowire tips [149,150] and suggested that the presence of an external electric field might facilitate 1D growth [149]. A strong electric field at the tip of the nanowires could attract the SiO clusters in the vapor, not requiring any difference in physical properties or composition of the head and the sidewall. Assuming that the typical diameter of the nanowires is 40 nm, the electric field at the tip would be 2.04×10^{10} V/m. There are three possible cases for the gas phase SiO vapor: (1) the SiO vapor is charged, (2) the SiO vapor has a permanent dipole moment, and (3) the SiO vapor has an induced dipole moment. The presence of a strong electric field at the tip will attract these molecules/clusters towards the tip, thereby changing their trajectory. The trajectory of the SiO molecules/clusters to the tip may indicate the percentage of SiO vapor that lands on the tip compared to that on the sidewall.

Assume that electrostatic attraction is the dominant force and that the electric field around the nanowire tip is given by

$$E = \frac{Q}{4\pi\epsilon_0 r^2}, \quad (3.3.4)$$

where r is the distance from the center of the nanowire tip. At the Si nanowire formation temperature (930 °C), the SiO molecules/clusters move towards the tip with a 930 °C thermal velocity (v).

The impact parameter is denoted by x (see Fig. 24). Initially, the molecules/clusters are 1 mean-free path (λ) away from the nanowire tip, so they have undergone the last collision, and thus no more collisions will occur. Setting $z = \lambda$, and R is the radius of the nanowire tip. Since $\lambda \gg R$, the initial electrostatic potential energy of the SiO molecule/cluster can be neglected.

With the typical nanowire growth at 500 Torr and 930 °C [11], the number of molecules per unit volume is $4 \times 10^{24} \text{ m}^{-3}$. Taking the radius of the SiO molecule to be 1.84 Å, which is the sum of the covalent radii of the Si and O atoms, the mean-free path of SiO molecules is of the order 1700 nm, indicating negligible collision between gas molecules. A SiO molecule/cluster will land on the nanowire tip when it approaches a tip with an impact parameter below this threshold value (called x_{th}). Once the threshold impact parameter (x_{th}) is obtained, the probability of the SiO molecule/cluster landing on the nanowire tip can be approximated by the ratio of the area within the threshold impact parameter to the “territory” of each nanowire:

$$\text{landing probability} = \frac{\pi(x_{th})^2}{4(D/2)^2} = \left(\frac{2x_{th}}{D} \right)^2. \quad (3.3.5)$$

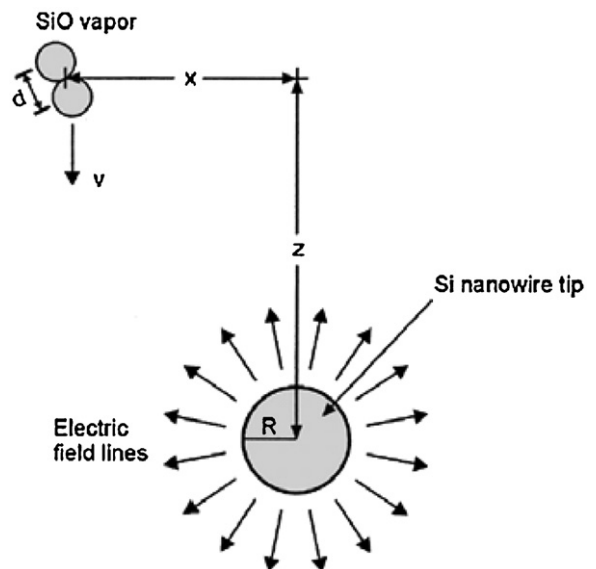


Fig. 24. Geometry of SiO vapor falling on a nanowire tip (from Ref. [149]; Reproduced with permission of American Institute of Physics).

where D is the diameter of the silicon nanowire and the threshold impact parameter (x_{th}) is given by

$$x_{\text{th}} = R \sqrt{\frac{|U_0|}{(1/2)mv^2} + 1} \quad (3.3.6)$$

with U_0 being the electrostatic potential energy of the SiO molecule/cluster when it reaches the surface of the nanowire tip.

(1) If the SiO vapor is singly charged ($q = e$), and is attracted to the nanowire tip, the threshold impact parameter can be calculated by setting

$$U_0 = -\frac{Qe}{4\pi\epsilon_0 R} = -eE_0R \quad (3.3.7)$$

(2) If the SiO vapor has only a permanent dipole moment (p), then $U_0 = -pE_0$.

(3) If the SiO vapor has only an induced dipole moment (polarizability α), then $U_0 = (1/2)\alpha E_0^2$.

Using some additional parameters estimated according to experiments, the landing probability is obtained and listed in Table 1. It seems that the electrostatic attraction to the molecules in the SiO vapors is sufficiently strong so that all molecules land on the nanowire tips. None have a chance to hit the sidewall. In this way, the growth of the nanowires at the tip is guaranteed.

3.4. Self-assembly growth from solution

The formation of nanowires from solution methods is complicated. The growth of nanowires generally involves the following steps: (1) crystalline seed formation; (2) crystal growth by aggregation of monomers to the seeds; and (3) surface stabilization by surfactants. So far, several mechanisms for the anisotropic growth of nanocrystals in solution have been proposed. Here are three representative mechanisms:

3.4.1. Solution-liquid-solid (SLS) growth from seeds

Similar to the VLS reaction, during the SLS reaction, monomers are generated by decomposition of molecular precursor at a high temperature. The metal catalysts for this kind of reaction are extremely small and therefore easily activated at low temperatures. The monomers react with the metal nanoseeds to form supersaturated alloy droplets (see Fig. 25(a)). Semiconductor nanowire growth, e.g., Si

and Ge nanowires [78,79], from Au nanocatalysts under the supercritical fluid environment have been achieved. Specially, ultra-thin nanowires [78] with diameters of 2–3 nm have been fabricated by this method and interesting optical properties have been observed in these nanowires. Such small diameters of nanowires cannot be easily realized by the classical VLS method from vapor phases.

3.4.2. Self-assembly oriented attachment growth

The self-assembly attachment growth is based on the fact that nanoparticles generated in solution have a large surface-to-volume ratio. To reduce the surface energy and thus the total system energy, the particles may segregate together. Oriented attachment is one of the ways for this segregation process. Penn and Banfield [89] first observed this nanowires formation mechanism in the hydrolytic synthesis of TiO₂ nanocrystals. Truncated TiO₂ nanocrystals mainly consisted of three faces, {0 0 1}, {1 2 1} and {1 0 1}. Since the {0 0 1} has the highest surface energy [90], it is reasonable to remove the high energy surfaces {0 0 1} since this is thermodynamic favorable. Through the oriented attachment process, the nanocrystals are fused along the [0 0 1] direction to eliminate the {0 0 1} faces (see Fig. 25(b)). This fusion process resulted in the formation of necklace-shaped wires. Similar structures have been observed in the growth of nanowire or necklace nanocrystals chain of CdTe [91], PbSe [92], ZnS [93] and ZnO [94].

3.4.3. Anisotropic growth of crystals by kinetic control

Anisotropic growth of crystals induced by different surface energies is the reason for the formation of most elongated nanocrystals. However, the difference of surface energies (the intrinsic properties of the crystal) is not large enough to cause highly anisotropic growth of long nanowires. By adding surfactants to the reaction solution, it is believed that the effective surface energy of a nanocrystal can be modulated, and the surfactant molecules selectively adsorb and bound onto certain surfaces of the nanocrystal seeds. For example, the [0 0 1] direction is the fast growth direction of TiO₂ nanocrystal growth in solution. By adding surfactants, the fast growth direction can be changed to [101]. The surfactants function as “structural directors”. This selective capping effect reduces the growth of these surfaces and induces the nanocrystal elongation along a specific direction to form nanowires (see Fig. 25(c)). The selective capping mechanism has been evidenced recently in many nanomaterials. Sun et al. [104,105] demonstrated that Ag nanowires can be fabricated using poly(vinyl pyrrolidone)

Table 1

Summary of the numerical results for SiO molecules (from Ref. [149]; reproduced with permission of American Institute of Physics)

Vapor	Charge carried ($q = 1.602 \times 10^{-19}$ C)	Permanent dipole ($p = 1.03 \times 10^{-29}$ Cm)	Induced dipole ($\alpha = 6.93 \times 10^{-40}$ Fm)
Threshold impact parameter x_{th}	1020 nm	59.9 nm	52.1 nm
Probability of landing on the nanowire tip $4x_{\text{th}}^2/D^2$	100%	100%	100%
Maximum electric field = 2.04×10^{10} V/m		$D = 100$ nm	
Radius of nanowire tip = 20 nm		Radius of SiO molecule = 1.84 \AA°	

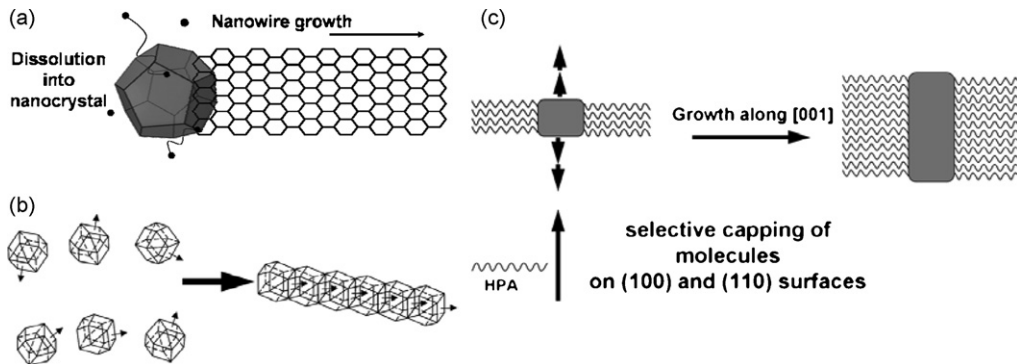


Fig. 25. (a) Schematic diagrams of nanowires formation from solution-based methods by (a) the SLS growth, (b) the oriented attachment growth, and (c) surface selective surfactant assisted growth (redraw after Ref. [77]).

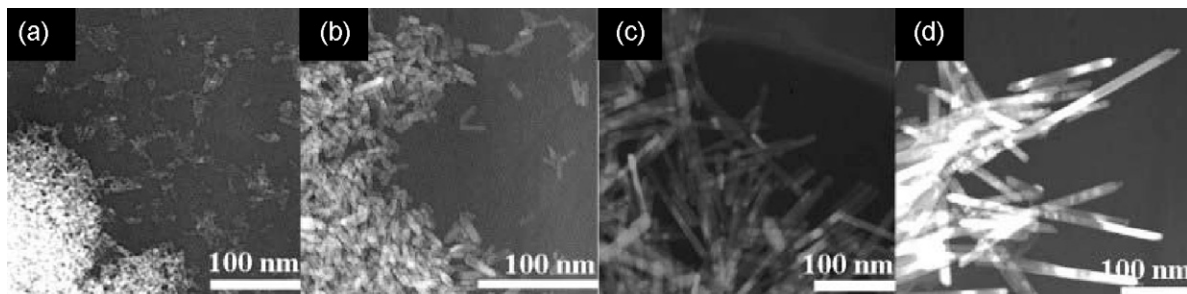


Fig. 26. TEM images of ZnO nanowires grown from solution. The samples were collected at the reaction time of (a) 10 min, (b) 20 min, (c) 40 min, (d) 1 h.

(PVP) as a capping agent. The silver nanocrystals initially formed by reducing AgNO_3 with ethylene glycol (EG) heated to $\sim 160^\circ\text{C}$. These nanocrystals served as seeds for the nucleation and anisotropic growth of silver. Their explanation is that PVP selectively bind (or passivate) to the $\{1\ 0\ 0\}$ facets of Ag particles and allow the growth of $\{1\ 1\ 1\}$ facets. For Au particles, however, the same capping agent PVP bonded only to the $\{1\ 1\ 1\}$ faces. Silver nanowires with a high length-to-diameter ratio (diameters in the range of 30–60 nm and lengths up to 50 μm) were produced. Both the morphology and aspect ratios of these silver nanostructures could be well controlled by the reaction condition.

Using a similar synthetic route, ZnO nanowires have been fabricated via the hydrothermal reactions of Zn salts in the presence of capping agents or structural directors, such as amines [111], hexamethylenetetramine [112]. However, without using any capping agent, ZnO nanowires can also be fabricated from Zn acetate solution in ethanol mixed with NaOH [114]. This synthesis is similar to the process described by Cheng et al. [115]. However, no structural director or surfactant is needed for the formation of high-quality ZnO nanowires. The fabrication is simply carried out by using 5 mL of 0.1 M zinc acetate solution in ethanol, which is mixed with 35 mL of 0.5 M NaOH solution in ethanol to form a solution that is later transferred into a Teflon-lined stainless steel autoclave (50 mL) and heated at 180°C . After 24 h of reaction, ZnO nanowires with uniform diameters were obtained. In this synthesis, it is difficult to identify the structural director for the ZnO crystals.

Fig. 26 shows the morphology changes of ZnO nanowires in the samples collected at different reaction stages. By increasing the reaction time, ZnO crystals developed from nanoparticles to nanorods and then nanowires continually. Noticed as the length of the nanowires increased, the diameter increased accordingly (see Fig. 27). The growth of the ZnO nanowires was not the oriented attachment mechanism. It is also hard to explain the nanowire growth by the surfactant effect since no surfactant is involved. The formation mechanisms and the function of the solution need systematical investigation.

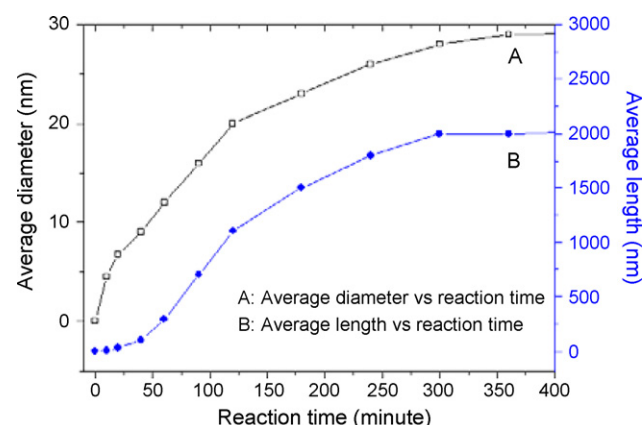


Fig. 27. The changes of the diameters and lengths of ZnO nanowires vs. reaction time.

4. Controlled growth of nanowires

4.1. Control of structures, growth direction and defects in nanowires

4.1.1. Interface structures

Due to the presence of metal catalysts in the VLS growth, the geometry and atomic structure of the interface between the metal catalyst and the nanowire have been found to be very critical to the nanowire growth and formation of defects, particularly the growth direction or crystal orientation in ultra-thin nanowires. Various interface structures have been identified by HRTEM studies [131,151–153]. With respect to cubic semiconductor whiskers that have grown along the $\langle 1\ 1\ 1 \rangle$ direction, the interface at the catalyst is generally perpendicular to the wire axis. However, for other growth directions, the interfaces are generally not perpendicular to the wire axis. This feature becomes obvious when the diameters of these cubic nanowires are smaller than 30 nm.

As an example, Fig. 28 shows the typical interface structures of ZnSe nanowires grown by MBE technique. Since the impurity of source materials, surface structures of the substrate and growth condition can be well controlled by MBE, an interesting growth phenomenon of ultra-thin nanowires has been revealed. The typical growth directions of cubic semiconductor nanowires are $[1\ 1\ 1]$, $[1\ 1\ 2]$, $[1\ 1\ 0]$ and $[0\ 0\ 1]$. The interface structures of different oriented nanowires show distinct morphologies. With respect to the $[1\ 1\ 1]$ growth nanowires, the interfaces at the catalysts are flat ($1\ 1\ 1$) planes which are perpendicular to the wire axis (Fig. 28(a)). For the $[1\ 1\ 2]$ and $[1\ 1\ 0]$ nanowires, the interfaces are generally along

the $(1\ 1\ 1)$ planes which are not perpendicular to the nanowire axis as shown in Fig. 28(b) and (c). Zigzag interfaces in these two oriented nanowires are frequently observed. The zigzag interfaces in the nanowires grown along the $[1\ 1\ 2]$ direction mainly consist of $(1\ 1\ 1)$ plus a small fraction of $(0\ 0\ 1)$ facets (Fig. 28(d)). The zigzag interfaces in the $[1\ 1\ 0]$ nanowires consist of $(1\ 1\ 1)$ and $(1\bar{1}\ 1)$ planes (Fig. 28(e)). In this case, the flat ($1\ 1\ 1$) interface and the zigzag one have the same interface area. The reason that these ($1\ 1\ 1$) planes are dominant at the interfaces is simply due to its low interface (or surface) energy compared to other planes. In cubic semiconductor materials, for example, Si, Ge and ZnSe, the $(1\ 1\ 1)$ is often the lowest surface energy plane and $(0\ 0\ 1)$ is the second lowest energy surface [131,154,155]. Therefore, it is reasonable that $(0\ 0\ 1)$ facets appear in addition to the $(1\ 1\ 1)$ facets at the interfaces. Fig. 29 illustrates the interface models for various growth directions that have been experimentally observed.

During the VLS growth, the metal catalysts are liquid at any temperature above the eutectic point. At the tip of a nanowire, there is a terminal growth zone in the order of several monolayers where atoms are in a nearly semi-molten state [128]. The theoretical calculation has shown that the atoms at the solid phase near the LS interface actually move away immensely from the lattice sites [128]. Using FCC structure models, computer simulation on the LS interface of $(1\ 1\ 1)$ and $(1\ 0\ 0)$ indicated that there were several layers of atoms in the “quasi-crystalline” state in which the amount of diffusion is not negligible, although the atoms spend most of their time in the lattice sites. This special LS zone is schematically shown by Lc (also called the critical thickness in the following discussion) in Fig. 30(a). Within this special zone, atoms in the nanowires are

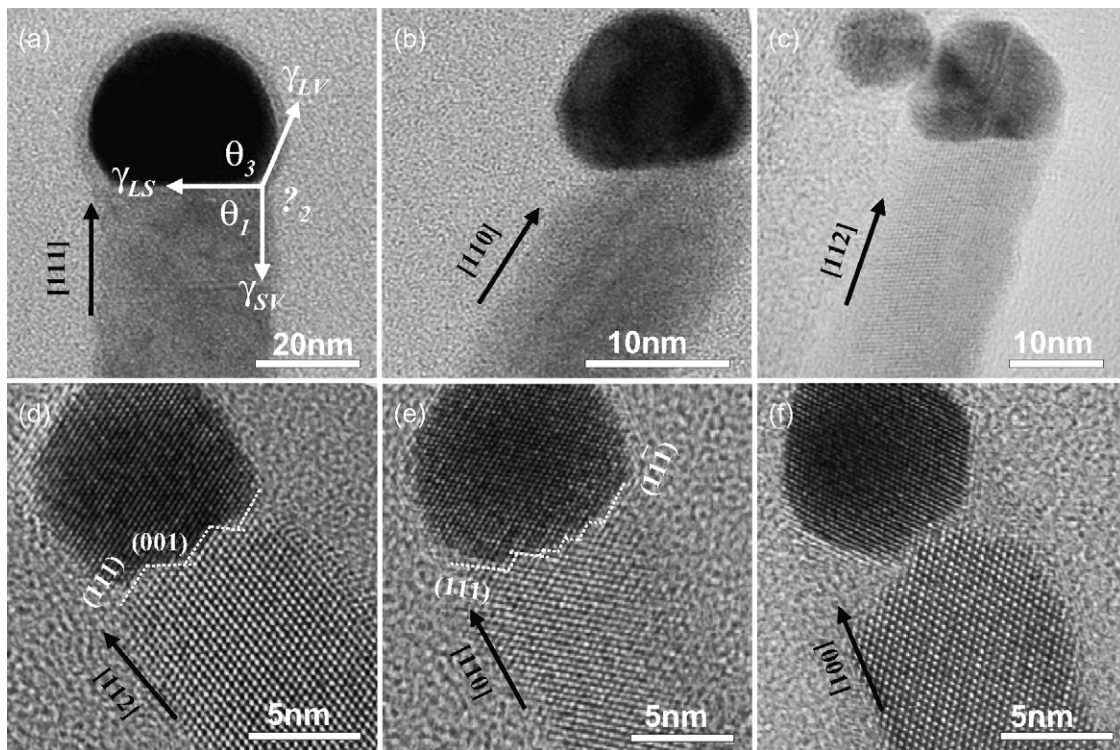


Fig. 28. ZnSe nanowires grown along (a) $[1\ 1\ 1]$, (b) and (e) $[1\ 1\ 0]$, (c) and (d) $[1\ 1\ 2]$, and (f) $[0\ 0\ 1]$ directions. .

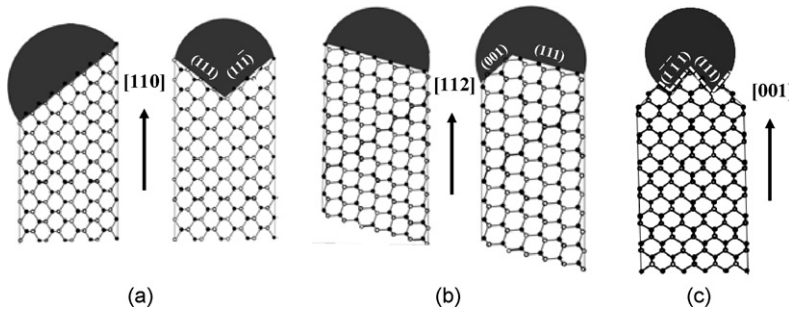


Fig. 29. The interface models of the different growth directions of nanowires. (a) [110], (b) [112], and (c) [001] growth directions.

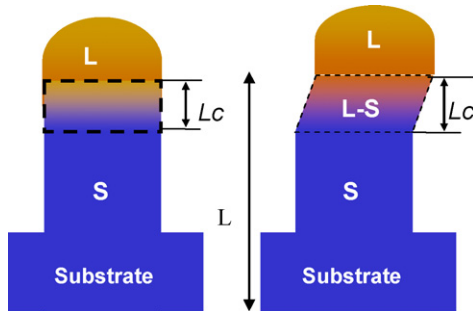


Fig. 30. Schematic of the LS zone at the tip of the nanowires grown by the VLS and the growth direction change at the critical thickness.

able to rearrange without changes in the original crystal structure so that the nanowire may display a certain growth direction (see Fig. 30(b)). The thickness of the LS zone is proportional to the growth temperature. A higher temperature results in a thicker LS zone. Even if the growth temperature is lower than the eutectic point, the LS zone may still exist due to the interface melting effect. Such a special interface has been observed in {111} Si-Al nanocrystal growth [51]. It was found that the atoms in the LS region were in a partially molten state. The width of this region was about 1.9 nm. The interface structures are important for the growth behaviors of ultra-thin nanowires. For the classical VLS deposition, the atomic diffusion is mainly controlled by the droplet. However, for growth at a relatively low temperature, the atomic diffusion and deposition are mainly controlled by surface and interfaces. In addition, this special LS zone has been found to be a critical

parameter for controlling the growth direction transition of ultra-thin nanowires [131].

4.1.2. The growth direction of VLS nanowires

The crystal orientation in semiconductor nanowires is important because it not only affects surface properties, but also their optical and transport properties [78,156]. For cubic semiconductor nanowires, several growth directions have been frequently observed, such as ⟨111⟩ [7], ⟨112⟩ [11,14,157] and ⟨110⟩ [78,158,159]. For most thick nanowires or whiskers, ⟨111⟩ growth direction is considered to be energetically favorable. Ultra-thin nanowires, such as Si, II-VI and III-V nanowires, often show variant growth directions. Nanowires often show different growth directions even on the same substrate. This feature is illustrated in Fig. 31(a), in which ZnSe nanowires inclined mainly along four directions, that is, at $\pm 19^\circ$ or $\pm 35^\circ$ (along the ⟨112⟩ direction as indicated in the pole stereographic projection diagram of cubic crystals in Fig. 31(b)) and $\pm 35^\circ$ (along the ⟨110⟩ direction) to the normal of the GaP(111) surface, respectively. On Si(100) substrate, Si nanowires grown by UHV-CVD displayed similar features of different growth directions [160].

By controlling the sizes of the catalysts and growth temperatures, it is observed that at the same growth temperature, all the nanowires with the same diameter actually grow along a specific direction. Fig. 32(a) and (b) illustrates the typical morphologies of ZnSe nanowires grown on GaAs(001) substrates at 530 °C. Fig. 32(a) were taken with an electron beam that is nearly parallel to the [110] direction of the

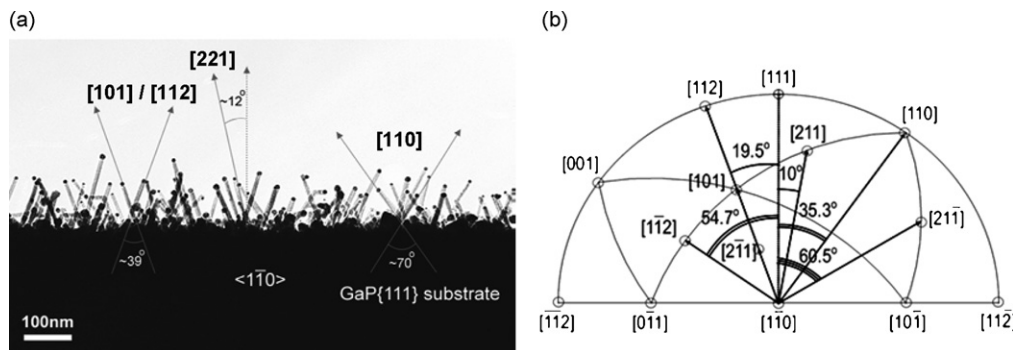


Fig. 31. (a) TEM image of the cleaved specimen viewed with an electron beam that is nearly parallel to the [110] direction of the GaP(111) substrate. ZnSe nanowires inclined mainly along four directions at $\pm 19^\circ$ and $\pm 35^\circ$ as indicated by the arrows. (b) The [110] pole stereographic projection diagram of cubic crystals. Some poles of ⟨110⟩ and ⟨112⟩ are indicated [14].

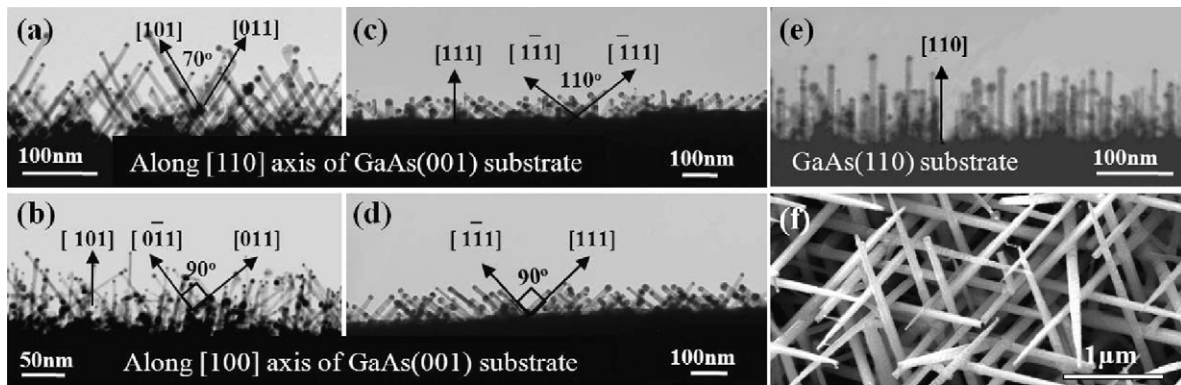


Fig. 32. (a)–(d) and (e) are ZnSe nanowires grown on GaAs(0 0 1) and (1 1 0) substrate surfaces, respectively. (a), (b) and (e) are grown at 530 °C, (c) and (d) are grown at 390 °C. (f) Si nanowires grown on Si(0 0 1) substrate [127].

GaAs(0 0 1) substrate. These ultra-thin ZnSe nanowires grew mainly along two directions that inclined approximately $\pm 35^\circ$ to the normal of the substrate surface. When observed along the $[1\bar{1}0]$ direction, the nanowires displayed the same inclination. Obviously, these nanowires grew along four equivalent $\langle 1\bar{1}0 \rangle$ directions of the substrate.

At 530 °C, ZnSe nanowires with diameters smaller than 10 nm grew mainly along the $\langle 1\bar{1}0 \rangle$ direction on different substrate surfaces (for example, (1 1 1), (1 1 0) and (1 0 0) substrates). This can also be seen in Fig. 32(e), in which almost all ZnSe nanowires with diameters of about 10 nm grew perpendicularly to the GaAs(1 1 0) substrate surface, that is, along the $[1\bar{1}0]$ direction. The nanowires with diameters greater than 30 nm prefer growing along the $\langle 1\bar{1}1 \rangle$ direction on GaAs substrates [131]. Thick Si nanowires grown from SiH₄/H₂ have a similar growth behavior as shown by the SEM pictures (top view) in Fig. 32(f). All of these Si nanowires grow along the $\langle 1\bar{1}1 \rangle$ direction and have 3 equiv. $\langle 1\bar{1}1 \rangle$ directions at 60° to each other. ZnSe nanowires with diameters ranging from 10 to 20 nm may grow along the $\langle 1\bar{1}2 \rangle$ or $\langle 1\bar{1}0 \rangle$ direction on these substrates. The change in the growth direction from $\langle 1\bar{1}1 \rangle$ to $\langle 1\bar{1}0 \rangle$ at a crossover diameter of approximately 20 nm in Si nanowires grown by CVD has been reported by Schmidt et al. [160]. They also observed that Si nanowires with diameters greater than 40 nm preferred to grow in the $\langle 1\bar{1}1 \rangle$ direction. Nanowires show obvious diameter-dependency when the growth condition is specified. Notice that the data on the growth directions of semiconductor nanowires from different research groups are very scattered and sometimes confusing. Even for one type of material, the nanowires with very similar diameters synthesized by different groups may have different growth directions. The main reason is that the fabrication condition varied from group to group. Systematical investigation for the growth condition, the atomistic structures of the nanowires and the catalyst is absolutely needed.

Si and II–VI compound nanowires have been studied and compared to data reported by different groups and it was found that nanowires from cubic semiconductor materials have common features in growth direction. In the past years, models based on various assumptions have been proposed for

interpreting nanowire growth directions. The growth direction $\langle 1\bar{1}2 \rangle$ and $\langle 1\bar{1}0 \rangle$ of Si nanowires synthesized by laser ablation or thermal evaporation of SiO source materials has been analyzed theoretically by Tan et al. [161,162]. In their model, four criteria have been considered, such as the stability of Si atoms at the surface, the stability of Si{1 1 1} surface, the stepped Si{1 1 1} surface growth and the dislocation effect. With these criteria, it is concluded that $\langle 1\bar{1}2 \rangle$ and $\langle 1\bar{1}0 \rangle$ are the preferred growth direction and that $\langle 1\bar{1}1 \rangle$ and $\langle 1\bar{0}0 \rangle$ are not favored. Based on the modeling of interface, surface energies together with the edge tension term, Schmidt et al. [160] demonstrated that for large diameters, the direction with the lowest interface energy is dominant, where for small diameters the surface energy determines the nanowire preferential growth direction. Si nanowires with diameters larger than 40 nm grew along the $\langle 1\bar{1}1 \rangle$ direction. Thin Si nanowires (diameter <20 nm) mostly grew along the $\langle 1\bar{1}0 \rangle$ direction. They did not consider the $\langle 1\bar{1}2 \rangle$ growth direction due to unavailable parameters.

Zhang et al. [171] have studied the structures and energetics of hydrogen-terminated Si nanowire surfaces and explained the experimental findings about the relative abundance of the Si nanowire growth directions. Some cross-sections identified in Si nanowires, the size dependences of the stability and the band-gap energy of these Si nanowires enclosed by low-index surfaces have been revealed by performing density-functional tight-binding simulations. Fig. 33 shows representative possible cross-sections for example for the $\langle 1\bar{1}1 \rangle$, $\langle 1\bar{1}0 \rangle$ and $\langle 1\bar{0}0 \rangle$ wires enclosed by low-index surfaces. These wires may have different possible cross-sections. Many low-index facet configurations and cross-sections are possible, which may lead to the difficulty of controlled growth. In general, the stability of a Si nanowire is determined by a balance between (1) minimization of the surface energy and (2) minimization of the surface-to-volume ratio.

The recent TEM study of the cross-sections of Si nanowires with large diameters grown by the oxide-assisted technique identified some interesting cross-sections, such as square, rectangular, and triangular cross-sections [172]. It is also revealed that the more frequent abundance of the $\langle 1\bar{1}2 \rangle$ (first) and $\langle 1\bar{1}0 \rangle$ (second) direction in these nanowires. As identified

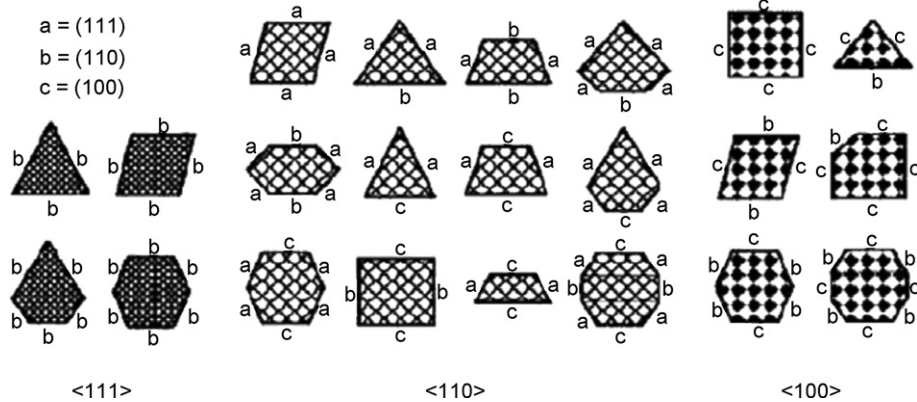


Fig. 33. Representative possible cross sections for the $\langle 111 \rangle$, $\langle 110 \rangle$ and $\langle 100 \rangle$ wires enclosed by low-index surfaces [171].

by scanning tunneling microscopy, an ideal $\langle 112 \rangle$ Si nanowire with an ultra small diameter (hydrogen-terminated after HF etching) was shown to be either a flat (111) surface or a flat (110) surface [173].

The TEM work of Wu et al. [151] indicates a somewhat different abundance of Si nanowires grown using the VLS method than observed with the oxide-assisted method. They found that the abundance of the Si nanowire growth directions depends on the Si nanowire diameter (d) as follows: (1) almost only $\langle 110 \rangle$ wires ($\sim 98\%$) are observed for $d < 10$ nm, (2) the $\langle 112 \rangle$ wires are most abundant for $10 < d < 20$ nm ($\sim 65\%$) but significant amounts of $\langle 110 \rangle$ (20%) and $\langle 111 \rangle$ (15%) are still found, (3) the $\langle 111 \rangle$ is the most abundant Si nanowires for $d > 20$ nm (65%), but 30% $\langle 112 \rangle$ and 5% $\langle 110 \rangle$ wires are still observed. Wu et al. [151] attributed the abundance of the growth direction to the formation of a lowest energy liquid/solid (111) interface first and the surface energetics driving the faceting growth along a specific direction occurs as a second stage. This may explain why in the OAG process where the nucleation is different, surface energetics is more dominant, i.e. the most stable $\langle 112 \rangle$ Si nanowires are the most common for small diameters. The cross section of a 3.8 nm $\langle 110 \rangle$ Si nanowires observed by TEM in Ref. [151] is similar to the hexagonal $\langle 110 \rangle$ wire in the previous STM work [173] enclosed by four (111) and two (100) surfaces that was discussed above.

Based on the interface structures and growth directions of different sizes in the II–VI nanowires, another plausible model was proposed [131] to elucidate the diameter-dependent growth direction of ultra-thin nanowires by estimating the surface and interface energies of nanowires. The interface and surface energies were found to determine the nanowire growth directions. The estimation and comparison of the nanowire energies are based on the following facts: (1) The interfaces at the root of the II–VI nanowires grown along $\langle 111 \rangle$, $\langle 112 \rangle$ and $\langle 110 \rangle$ on GaAs(111) or GaP(111) substrates were always {111} since the nanowires epitaxially formed on the substrate. (1) At the tips of the nanowires, the interfaces between the metal catalysts and the nanowires with different growth directions and diameters were also {111}. The geometries of the nanowires are illustrated in Fig. 34. The interfaces are sometimes not flat and are shown in Fig. 28 as examples for the

[112] and [110] nanowires. However, the zigzag interfaces are mainly consisted of (111) facets. For the [110] nanowire, the interface areas (between the catalyst and the nanowire) for the flat interface and zigzag interface are identical. The observed preferences for growth directions can be understood in terms of the liquid catalyst/nanowire interfacial energy and the ZnSe nanowire surface energy. Obviously, on the same substrate, the growth of the nanowires is driven by the minimum state of the total surface and the interfacial energy of the nanowire.

To estimate the total energy of a nanowire, the nucleus of a ZnSe nanowire as a column with two plane interfaces and a cylindrical side surface is taken under consideration. Since the surface-to-volume ratio is high and the bulk crystal energy is independent of a nanowire orientation, only surface and interface energies need to be considered. For nanosized crystals, a cylindrical side surface generally consists of low-energy surfaces and steps. As shown in Fig. 34, the hexagonal shape is a moderately good approximation to describe the cross-section of a nanocatalyst or a nanowire [163]. The hexagonal shapes predicted by the Wulff construction are moderately good approximations to describe the cross-section of nanowire nuclei (see Fig. 34(c)). Fig. 34(b) is the top view of the Au-catalyst at the tip of a [110]-oriented ZnSe nanowire. The catalyst is hexagonally shaped and the side surfaces are {100} and {111}, which agree well with the model in Fig. 34. For the three growth directions ($\langle 111 \rangle$, $\langle 112 \rangle$ and $\langle 110 \rangle$), the most possible side surfaces are schematically shown in Fig. 34(c). The initially formed nanowires should be hexagonal disks. The side surfaces can be {111}, {110}, {113} and {100} (the energetically most favorable surfaces with low surface energies). The top and bottom surfaces are interfaces with the catalyst and the substrate, respectively. Thus, the total energy of a nanowire nucleus is

$$F = \sum A\gamma_s + E_e \quad (4.1.1)$$

In this context, $A\gamma_s$ and E_e denote the surface/interface energy and edge/step energies, respectively. A is the area of the surface/interface. For the hexagonal shape approximation, E_e can be considered as a fixed term for different oriented nanowires. Therefore, only surface and interface energies need to be

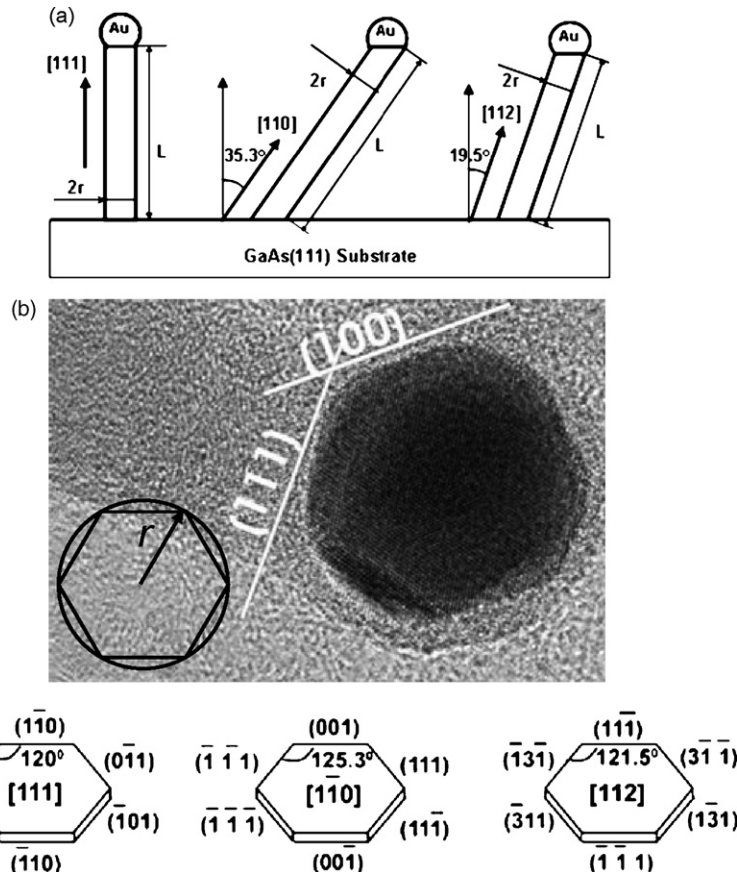


Fig. 34. (a) Models of the nanowire nuclei grown along [111], [110] and [112] directions. (b) Top view of a nanowire tip with Au catalyst. The shape of the catalyst/nanowire section is close to a hexagon. (c) There are two interfaces which can be described by hexagonal shape approximation. [131].

considered and they are the major factors affecting the growth direction of ZnSe nanowires. For a certain volume, nanowires preferentially grow in the direction that minimizes their total interface/surface energy. For a nanowire with radius r and length L , the total surface/interface energy is given by

$$F = 2\pi rL\gamma_{SV} + \pi r^2\gamma_{LS} + \pi r^2\gamma_{SS} \quad (4.1.2)$$

where γ_{SV} is the solid–vapor interface energy (or surface energy) and γ_{LS} is the LS interface energy between Au catalyst and ZnSe. γ_{SS} is the interface energy between ZnSe and the substrate. Since ZnSe nanowire epitaxially formed on the substrate, γ_{SS} is small compared to γ_{SV} and γ_{LS} . It will not be counted in the present model. Dividing F by the nanowire volume, the surface/interface energy per volume f is expressed as

$$f = \frac{2\gamma_{SV}}{r} + \frac{\gamma_{LS}}{L} \quad (4.1.3)$$

The surface energies of the major facets in ZnSe(111), (100), (311) and (110) normalized with respect to $\gamma_{\bar{1}\bar{1}\bar{1}}$ are determined to be 1.18, 1.10, 1.16 and 1.19, such as $\gamma_{\bar{1}\bar{1}\bar{1}} < \gamma_{\{100\}} < \gamma_{\{311\}} < \gamma_{\{110\}}$ [76]. Subsequently, the absolute values of these surface energies can be calculated using $\gamma_{\bar{1}\bar{1}\bar{1}} = 0.563 \text{ J m}^{-2}$ [164]. The interface energy γ_{SL} was

determined on the basis of the Young–Dupre equation:

$$\frac{\gamma_{LV}}{\sin \theta_1} = \frac{\gamma_{LS}}{\sin \theta_2} = \frac{\gamma_{SV}}{\sin \theta_3} \quad (4.1.4)$$

which represents the equilibrium condition of the surface and interface energies. In this context, θ_1 , θ_2 and θ_3 are the contact angles as depicted in Fig. 28(a).

For the $\langle 111 \rangle$ oriented nanowire with a hexagonal cross-section, there are six $\{110\}$ -type side surfaces and two $\{111\}$ interfaces. It is assumed that the nanowire cross-section is an inscribed hexagon of the circular cross-section of the nanowire with a diameter r (see Fig. 34), which can also be considered as the diameter of the circumscribed circle of the hexagon. The radius r of the $\langle 111 \rangle$ oriented nanowire is equal to the width of each $\{110\}$ facet. Its surface/interface energy is

$$f_{\langle 111 \rangle} = \frac{2\gamma_{\{110\}}}{r} + \frac{\gamma_{\{\bar{1}\bar{1}\bar{1}\}SL}}{L} \quad (4.1.5)$$

For the $\langle 110 \rangle$ oriented nanowire, the side surfaces consist of four $\{111\}$ -type facets and two $\{100\}$ -type facets. According to the Wulff construction, the cross-section should not be a regular hexagon with equal sides because there are two large $\{\bar{1}\bar{1}\bar{1}\}$ facets and two small $\{111\}$ facets for polar cubic semiconductor materials. To simplify the calculation, $\bar{\gamma}_{\{111\}}$ (the average surface energy of the polar $\{\bar{1}\bar{1}\bar{1}\}/\{111\}$ pair

planes) is introduced, and then the four $\{1\bar{1}1\}$ planes are equivalent. $\bar{\gamma}_{\{1\bar{1}1\}}$ is estimated on the basis of the relative proportion of $\gamma_{(111)}/\gamma_{(\bar{1}\bar{1}\bar{1})}$. A geometrical parameter q is further defined to represent the percentage of $\{1\bar{1}1\}$ facets among the nanowire circumference. Consequently, the surface/interface energy for $\langle 110 \rangle$ oriented nanowire is

$$f_{\langle 110 \rangle} = \frac{2[q\bar{\gamma}_{\{1\bar{1}1\}} + (1-q)\gamma_{(100)}]}{r} + \frac{\gamma_{(\bar{1}\bar{1}\bar{1})\text{SL}}}{L \cos 35.3^\circ} \quad (4.1.6)$$

35.3° is the incline angle of the $\langle 110 \rangle$ nanowire (see Fig. 34). Similarly, the $\langle 112 \rangle$ oriented nanowire consists of a pair of polar side surfaces $(\bar{1}\bar{1}\bar{1})/(111)$ and four $\{311\}$ side surfaces. Its surface/interface energy can be expressed as

$$f_{\langle 112 \rangle} = \frac{2[p\bar{\gamma}_{\{1\bar{1}1\}} + (1-p)\gamma_{(311)}]}{r} + \frac{\gamma_{(\bar{1}\bar{1}\bar{1})\text{SL}}}{L \cos 19.5^\circ} \quad (4.1.7)$$

where p is the geometrical parameter and 19.5° is the incline angle of $\langle 112 \rangle$ nanowires (see Fig. 34).

The estimated nanowire surface/interface energy changes for different oriented ZnSe nanowires are shown in Fig. 35. The changes of the surface/interface energy (f) versus the nanowire length (L) (see Fig. 35(a) and (b)) indicate that $\langle 111 \rangle$ ultra-thin nuclei are always at the minimum energy state and therefore, $\langle 111 \rangle$ is the preferential growth direction when the nanowire length is shorter than a certain value. This is because in the initial stage of nucleation, the side surface area is relatively insignificant. The total surface energy of a ZnSe nanowire is mainly determined by the $\{111\}$ interfaces. However, after the length of the nanowire exceeds a certain value, $\langle 111 \rangle$ growth may not offer the minimum energy state because the energy of a

longer nanowire is determined by the side surfaces, for example, the $\{110\}$ surfaces (high surface energy) in nanowire oriented in the $\langle 111 \rangle$ direction. Therefore, at a fixed growth temperature, with an increase in the nanowire length, the orientation of a nanowire may change from the initial $\langle 111 \rangle$ to $\langle 112 \rangle$ or to $\langle 110 \rangle$ in order to minimize the total system energy of the nanowire.

Although a long $\langle 111 \rangle$ nanowire has a higher system energy, it may not change to a lower energy state of a $\langle 112 \rangle$ or $\langle 110 \rangle$ growth direction. The reason is because the solid wire body is in a stable crystal structure and the atoms in the solid crystal cannot be rearranged so that the nanowire shows a different growth direction. However, the atoms at the interface of the metal catalyst are in a semi-melting stage and can rearrange themselves to change the growth direction of the nanowire. The solid–liquid interface structure, also called the effective thickness, together with the size of the catalyst or the diameter of the nanowire at the tip of the nanowire, is the most critical factor influencing the nanowire growth direction. L_C was used to indicate the effective critical thickness of a nanowire nucleus (corresponding to the width of the special LS growth zone in Fig. 30) at which the growth direction can change. The critical thickness L_C in ZnSe nanowires is estimated at about 2 nm (six stacking layers of ZnSe) at a high temperature. Within this zone, the change of the nanowire growth direction can be triggered in order to favor a lower energy state. Since the L_C is proportional to the growth temperature, in a low temperature growth; that is, the L_C is small, the diameter at which the growth direction transition occurs becomes small.

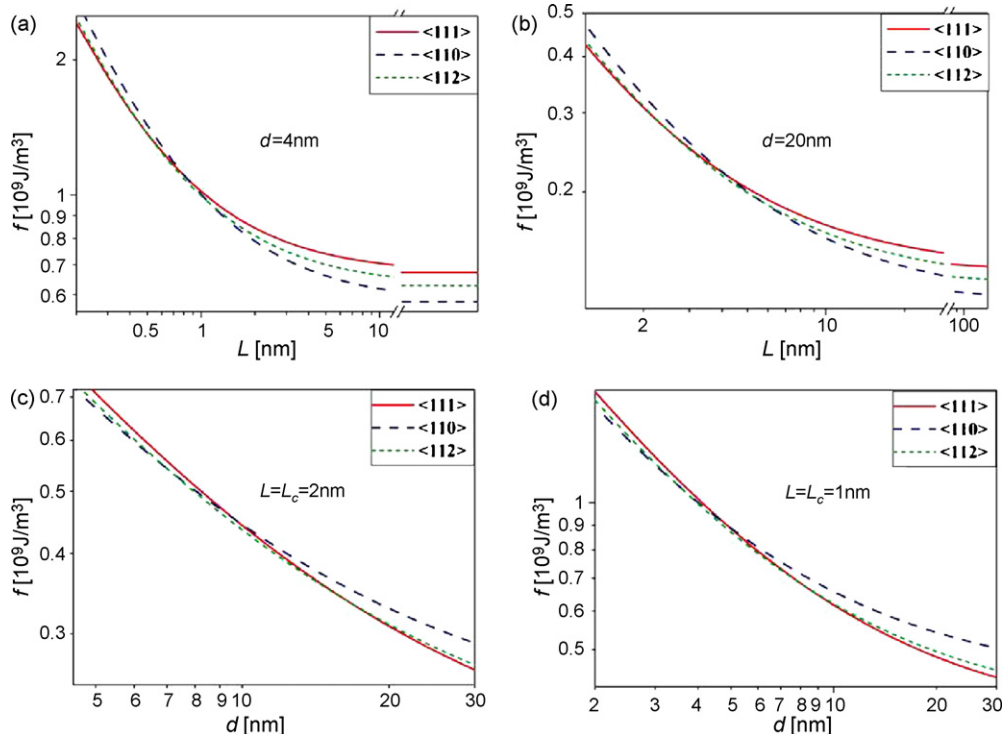


Fig. 35. Nanowire surface/interface energy (f) vs. the nanowire length (L) for ZnSe nanowires with a fixed diameter (a) $d = 4$ nm and (b) $d = 20$ nm. Nanowire surface/interface energy (f) vs. the nanowire diameter at the critical length (c) $L_C = 2$ nm and (d) $L_C = 1$ nm.

Hence, the diameter of the catalyst is critical. If the diameter of the catalyst is large, the contribution of the two interfaces in the total system energy will always be dominant when the length is shorter than L_C . In this case, the nanowire will keep on growing along the $\langle 111 \rangle$ direction even though its final energy is higher in comparison to that of other growth directions. For ZnSe nanowires catalyzed by small-diameter Au catalysts, within the critical thickness, the contribution from the side surfaces will be largely increased. As a consequence, this triggers the transition of nanowire growth direction to reach a lower energy state, such as, either along $\langle 112 \rangle$ or $\langle 110 \rangle$. For ZnSe nanowires with ultra small diameters, $\langle 110 \rangle$ growth will be more energetically preferable.

Fig. 35(c) illustrates the change of f versus the nanowire diameter d at the critical thickness $L_C = 2$ nm. For ZnSe nanowires with small diameters ($d < 7$ nm), $\langle 110 \rangle$ will be the most preferable growth direction. Medium-sized ZnSe nanowires ($7 \text{ nm} < d < 17$ nm) prefer $\langle 110 \rangle$ and $\langle 112 \rangle$ growth direction. $\langle 111 \rangle$ is the most preferable growth direction for ZnSe nanowires with large diameters ($d > 17$ nm).

At a low growth temperature, L_C becomes small and thus, the diameter at which the transition of the growth direction occurs is also small. This is revealed in Fig. 35(d) where $\langle 111 \rangle$ is the most preferable growth direction for nanowires with diameters greater than 9 nm ($L_C = 1$ nm). However, when $L_C = 2$ nm, the crossover diameter is about 17 nm. Fig. 36(a) summarizes the relationships between the growth direction, diameter and growth temperature (L_C thickness) qualitatively. The growth direction is also temperature-dependent. When L_C is fixed, that is, at a growth temperature, a large nanowire diameter results in $\langle 111 \rangle$ growth while a small diameter results in $\langle 110 \rangle$ growth. With a fixed nanowire diameter, a large L_C , such as a high growth temperature, results in $\langle 110 \rangle$ growth and a small L_C , that is, a low growth temperature, should lead to $\langle 111 \rangle$ growth. This result agrees well with the experimental observation that is shown in Fig. 32 where ZnSe nanowires with diameters of about 10 nm grown at a high temperature (530 °C) favor the $\langle 110 \rangle$ direction while those grown at a low temperature (390 °C) favor the $\langle 111 \rangle$ direction. While, ZnSe nanowires with the same diameter grown on the same substrate at 390 °C had incline angles of $\pm 35^\circ$ and 90° (see Fig. 32(c)). When these nanowires grown at the lower temperature were

viewed along the $[001]$ direction (see Fig. 32(d)), they inclined mainly in two directions at $\pm 45^\circ$. Obviously, the nanowires grew along the $\langle 111 \rangle$ direction on the (001) substrate at 390 °C.

The $\langle 111 \rangle$ growth direction of ultra-thin ZnSe nanowires inclined at 35.3° to the substrate surface (shown in Fig. 37(a)) at a lower growth temperature (390 °C) was also confirmed by HRTEM. Fig. 37(b) shows a cross-sectional HRTEM image of ZnSe nanowires grown at 390 °C on the GaAs(001) substrate. A thin ZnSe layer was also formed on the substrate surface due to the low growth temperature. The epitaxial ZnSe layer contained stacking faults. Although the Au nanocatalysts formed initially on the (001) substrate surface, the growth direction of the nanowires was not along the $[001]$ direction (not perpendicular to the (001) substrate surface). The growth direction transition occurred at the region near the root of the nanowires soon after the initial growth stage. Hence, all nanowires grew along the $\langle 111 \rangle$ direction. Based on the interesting diameter- and temperature-dependent properties of the VLS growth of nanowires, the growth directions of nanowires with different diameters at varying growth temperatures can be quantitatively explained and predicted. Furthermore, controlling some of the growth directions of the nanowires is possible. For example, by changing the growth temperature, nanowires change their growth directions accordingly (see Fig. 36(b)). The critical thickness at the catalytic tips of the nanowires is the most important factor for controlling the transition of the nanowire growth direction. It should be applicable to nanowire growth of different materials.

4.1.3. Defects in nanowires

The growth temperature not only affects the nanowire growth direction, but also the quality of the nanowires. According to the classical VLS mechanism, the growth temperature should be higher than the eutectic point of the metal catalyst in order to form alloy droplets. Recent studies [54,165] have demonstrated that due to the surface melting effect of nanosized particles or the interface melting effect, the growth of nanowires at a temperature below the eutectic temperature of the catalysts is possible. Fig. 38 shows ZnSe nanowires grown at a relatively low temperature of 390 °C. Note that the deposition of ZnSe on the substrate surface was

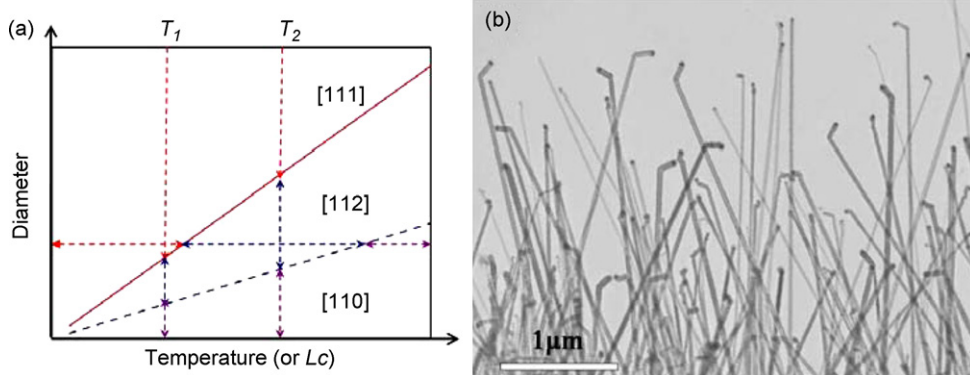


Fig. 36. (a) Relationship between the nanowire diameter, growth direction and temperature. (b) Nanowires change their growth directions at the tips [127].

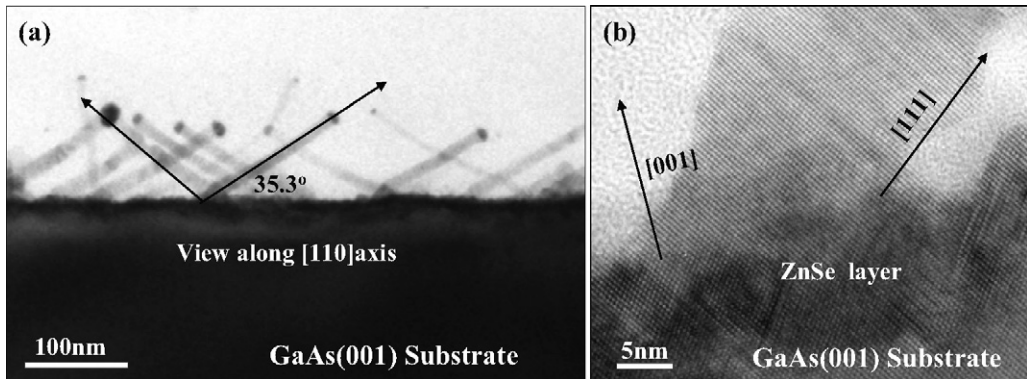


Fig. 37. (a) Cross-sectional TEM image of ZnSe nanowires grown at 390 °C on the GaAs(0 0 1) substrate. (b) HRTEM image showing the change of the nanowire growth direction from $\langle 0\ 0\ 1 \rangle$ to $\langle 1\ 1\ 1 \rangle$ direction [127].

significant and the diameter of a single nanowire was not uniform during the initial growth. The roots of the nanowires are thick in comparison to the tips of the nanowires. The surfaces near the roots are rough which are possibly due to the diffusion of atoms from the substrate surface to the nanowires. Once the length of the nanowire is longer than a certain value, there are not any obvious changes in the nanowire diameters. Since some of the catalyst diameters are much smaller than that of the root, the change of the root diameter should not result from the line tension as discussed in Section 3.1.

Similar to the case of Si nanowires, the quality of these nanowires was poor in comparison with the nanowires grown at a higher temperature. The main defects that resulted in the nanowires were high density stacking faults and twins. For $\langle 1\ 1\ 1 \rangle$ growth nanowires, these defects were parallel to the $\{1\ 1\ 1\}$ planes, that is, perpendicular to the nanowire's growth direction. One of the reasons for the formation of planar defects, such as twins or stacking faults, was due to the phase transformation from the FCC structure to the hexagonal close packed (HCP) structure. The formation energies for both structures were close. From the structural view point, stacking faults, $(1\ 1\ 1)$ twins (Σ_3 , twin plane $(1\ 1\ 1)$) and the HCP structure can be generated from the same planar defects of stacking faults. For the VLS growth of nanowires in cubic structure along the $[1\ 1\ 1]$ direction, the interface is closely packed $(1\ 1\ 1)$. The occupation of an atom on one sub-lattice (for example, B) prohibits the occupation of the neighboring

atoms which belong to the other sub-lattice (for example, C). At the liquid–solid interface, the structure of the first layer in contact with the crystal surface of $(1\ 1\ 1)$ has been systematically investigated by computer simulations. It has shown that islands of A-site atoms and C-site atoms both occupy the first liquid layer [128], separated by the channels in which it is not possible to place a new atoms in contact with the crystal surface. This is the origin of the stacking faults or disordered structure formation. High density twins and stacking faults in the $\langle 1\ 1\ 1 \rangle$ growth nanowires have been frequently observed (see Fig. 38(b)). The formation of defects is temperature dependent. At 530 °C, ZnSe nanowires are cubic structure. Decrease of the growth temperature results in the increase of the density of stacking faults and twins, and some HCP structure. At a low growth temperature ($T = 390$ °C), ZnSe nanowires are mainly HCP structures, as shown in Fig. 38(c).

In Fig. 39, the stacking faults are often parallel to the $[1\ 1\ 2]$ ZnS nanowire axes. Some of the stacking faults are equally spaced (Fig. 39(a)). The periodic arrangement of stacking faults on every closed-packed plane results in the formation of hexagonal structures. Fig. 39(b) is schematic of the twining structure viewed along the $[1\ 1\ 0]$ direction. When the nanowire along the $[1\ 1\ 1]$ direction (see Fig. 39(c)) was observed, all of the planar defects were overlapped and this causes the appearance of the $1/3(2\ 2\ 4)$ diffraction or the 0.33 nm fringes. In the HRTEM image in Fig. 39(c), the fringes show sixfold symmetry and correspond to the innermost diffractions that

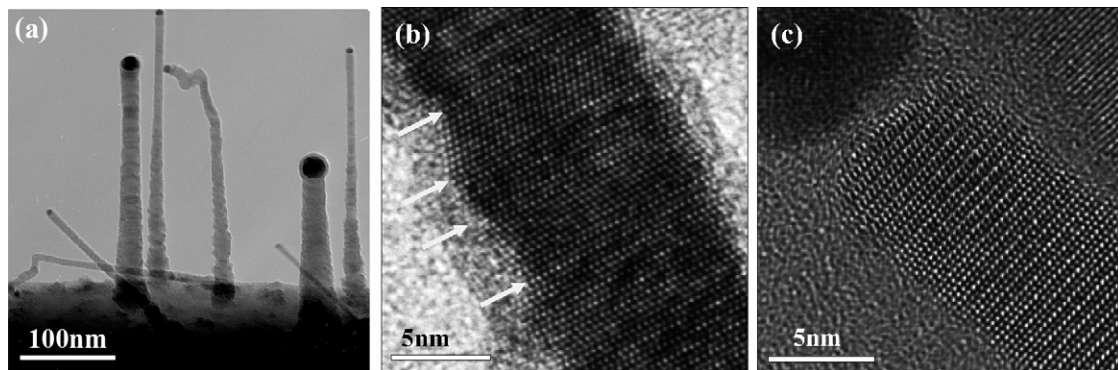


Fig. 38. (a) ZnSe nanowires grown at 390 °C. (b) High density stacking faults and twins (marked by the arrows) in a ZnSe nanowire grown at a low temperature. (c) HCP structure nanowires grown at a low temperature.

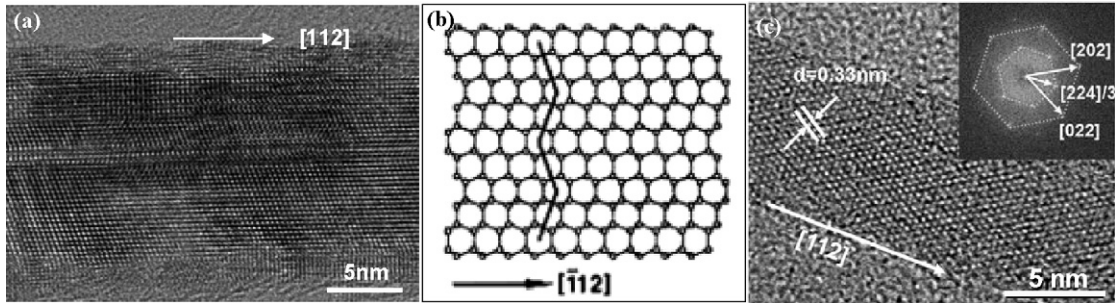


Fig. 39. (a) A $\langle 1\ 1\ 2 \rangle$ growth ZnS nanowire contains a high density of stacking faults and twins when viewed along the $[1\ 1\ 0]$ direction. (b) Twining structures viewed along the $[1\ 1\ 0]$ direction. The twining plans are $(1\ 1\ 1)$. (c) A $\langle 1\ 1\ 2 \rangle$ growth ZnS nanowire containing defects on $(1\ 1\ 1)$ planes which are invisible when viewed along the $[1\ 1\ \bar{1}]$ zone axis. The inset is the corresponding FFT [127].

appear at $(2\ 2\ 4)/3$ position. The Fourier transform of the HRTEM confirms that the fringes were generated by overlapping of the twining structures.

Nanowires often grow in the form of bi-crystals [166–168]. The bi-crystal nanowires may form by the self-catalytic growth of the twin boundary effect as discussed in Section 3.2 (no metal catalyst is needed) or induced by additives, for instance, Sb, Sb-oxide and MnBi, etc. Several kinds of ZnO bi-crystal nanowire tips that are fabricated by thermal evaporation methods are shown in Fig. 40. The growth of the bi-crystal nanowires can either be the VLS or VS deposition enhanced by boundaries. As discussed in Section 3.2, a twin boundary can effectively generate atomic steps and the melting temperature of a grain boundary is always lower than that of the bulk crystal. The boundary is also the place where impurities prefer to segregate. In some materials, bi-crystals have a certain

orientation relationship. For example, in Si bi-crystal nanowires, the growth direction is $[1\ 1\ 2]$ and the twin boundary is $(1\ 1\ 1)$, along the nanowire axis. The tip structure of a ZnO bi-crystal nanowire induced by a Sb catalyst is shown in Fig. 40(a) which is very similar to the Si bi-crystal nanowires catalyzed by Au particles. Obviously, their growth is the VLS reaction enhanced by the boundary effect.

With respect to thermal evaporation cases of pure ZnO power without adding metal catalyst, there is no obvious catalyst on the tips of ZnO bi-crystal nanowires (Fig. 40(d)). By adding graphite into the ZnO source material in order to generate a high concentration of Zn during the thermal evaporation, Zn metal droplets can sometimes be observed on the tips of ZnO bi-crystal nanowires (see Fig. 40(c)). By tilting the bi-crystal along the wire axis, the shape of the bi-wires is found to be ribbon-like (see Fig. 40(f)) which is possibly due to

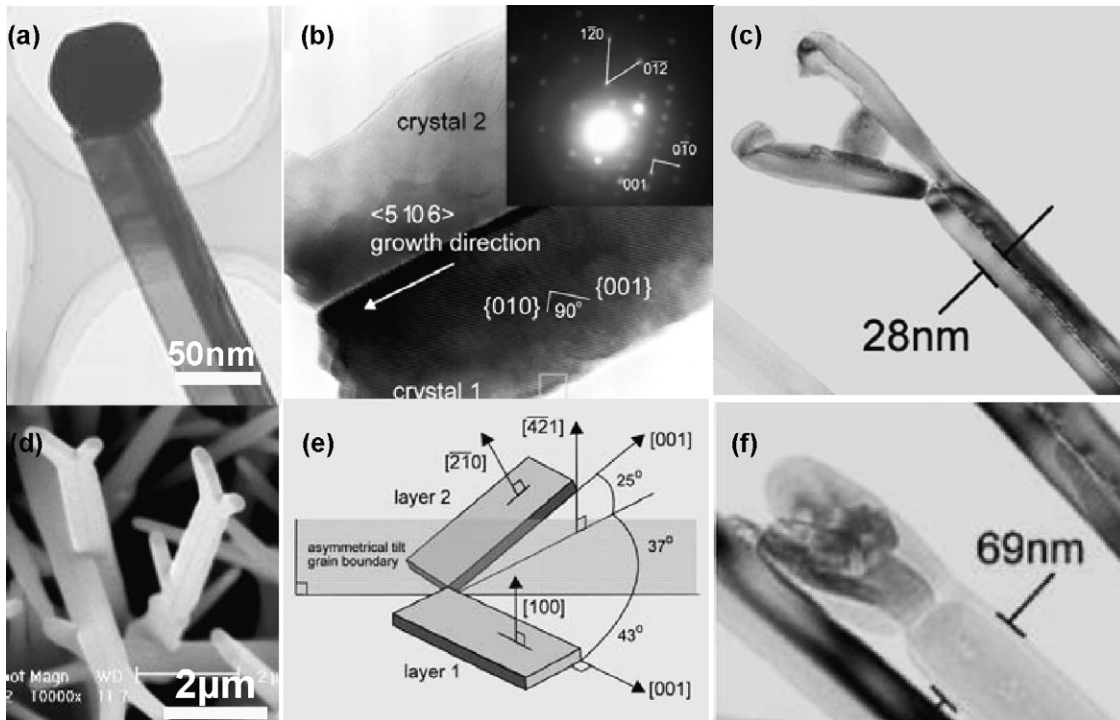


Fig. 40. Bi-crystal ZnO nanowires formed (a) with Sb catalysts and (b)–(f) without catalysts. (b) The interface structure of the bi-crystal nanowire of (c). (c) and (d) Bi-crystal nanowires formed by self-catalyzed VS process. (e) The orientation relationship of the bi-crystal nanowires. (f) The nanowire in (c) viewed in a different direction.

the sideway growth of the wires enhanced by the twin/grain boundaries. Fig. 40(b) and (e) shows the orientation relationship of grains in a ZnO bi-crystal wire. From the electron diffraction patterns and HRTEM image of this bi-crystal nanowire, the boundary was an asymmetrical tilting grain boundary with a growth direction along [5 10 6]. The thickness of the bi-wire is about 30 nm. By tilting about 90° along the nanowire axis, the width of the bi-wire is measured to be about 70 nm. For a prolonged growth, bi-crystal ribbons formed because of the boundary enhancement on the sideway growth.

Fig. 41 depicts two possible formation mechanisms of bi-crystal nanowires. The bi-crystal may form through (1) the merging of two nanowire nuclei and (2) twining structures. The presence of catalysts is unnecessary at the tips of the bi-crystal wires since grain boundaries (or twin boundaries) and the impurities segregated at the boundaries can catalyze the wire growth.

4.1.4. From nanowire to nanoribbon

By changing the synthesis conditions, the nanowire growth may switch to a quasi-two-dimensional growth, resulting in a ribbon or belt morphology. Such a special morphology has been frequently observed in non-layered structures of semiconductors and metal oxides [12,169–171]. To fabricate Si nanoribbons from the oxide-assisted growth, a typical experiment was carried out in a tube furnace, where SiO powder as the source was placed at the center zone with a temperature of 1150 °C. The evaporated material was carried down the tube by a gas mixture of 5% hydrogen in argon at a flow rate of 50 standard cubic centimeters per minute at a total pressure of 0.5 Torr. The growth of Si nanoribbons differs markedly from that of silicon nanowires and the conditions for nanoribbon growth are quite restrictive. In the same experiment, if the temperature and the pressure of the system (up to 1250 °C and 400 Torr, respectively) were increased, only wires and not ribbons were observed in the deposited product.

Si nanoribbons (Fig. 42) were abundantly grown on substrates that were placed down the tube where the temperature was 900 °C. The thickness of the Si ribbons was about 10–20 nm and the width was hundreds of nanometers to micrometers. Due to the presence of oxygen during the growth, the edges of the nanoribbons sometimes became oxide, forming

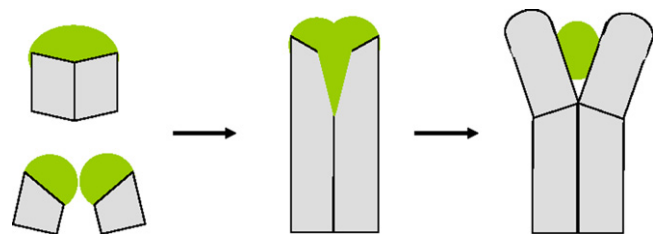


Fig. 41. Models for the formation of bi-crystals through merging or twining nuclei.

rippling edges. The rippling edge was determined to be amorphous silicon oxide. By carefully examining a number of long ribbons which have not been broken by the TEM sample preparation, it was found that the widths of all the intact ribbons had shrunk continuously (marked by the arrow in Fig. 42(b)) and finally, became nanowires with a diameter of about 20 nm (marked by “F”). It is suspected that the ribbons evolved from Si nanowires by sideway growth. As indicated by the HRTEM images, all of these ribbons (or the former nanowires) grew along the $\langle 1\ 1\ 1 \rangle$ direction. This direction was not the typical growth direction of Si nanowires from the oxide-assisted growth. This growth direction might have resulted from the changes in the experimental condition, such as, the pressure. Due to the presence of defects, for example, stacking faults or twin structures, the fast growth of $\langle 1\ 1\ 2 \rangle$ was triggered and enhanced by these defects. Since the ribbons are along the $\langle 1\ 1\ 1 \rangle$ direction, the $\langle 1\ 1\ 2 \rangle$ is perpendicular to the ribbon axis.

Fig. 43 is a high-resolution TEM image of a single crystalline nanoribbon. It reveals that the ribbon has a crystal core that is nipped by amorphous layers with atomically sharp interfaces. The in-plane layers of the nanoribbon are silicon (1 1 0) facet with a perfect atomic, defect-free, single-crystal structure grown along the $\langle 1\ 1\ 1 \rangle$ direction. Although stacking faults or twin boundaries are not visible in this HRTEM image, it does not mean that planar defects do not exist because planar defects may not be observed if they are not parallel to the observation direction. Using a dark-field imaging technique, the diffraction contrast (choosing (1 1 1) diffraction for the dark-field imaging) from some nanoribbons showed interesting features as illustrated in Fig. 44. There is a high density of line contrast perpendicular to the ribbon axis (the dark-field image

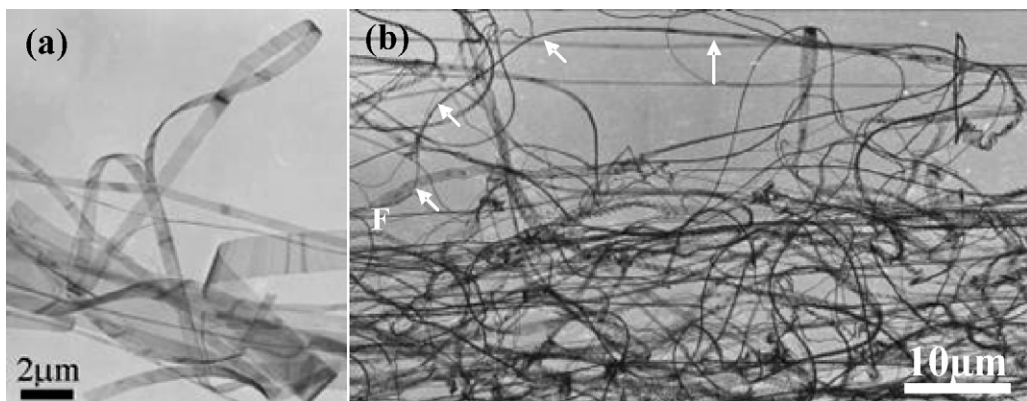


Fig. 42. (a) Si nanoribbons fabricated by the oxide-assisted growth. (b) The ribbons evolved from the sideway growth of nanowires.

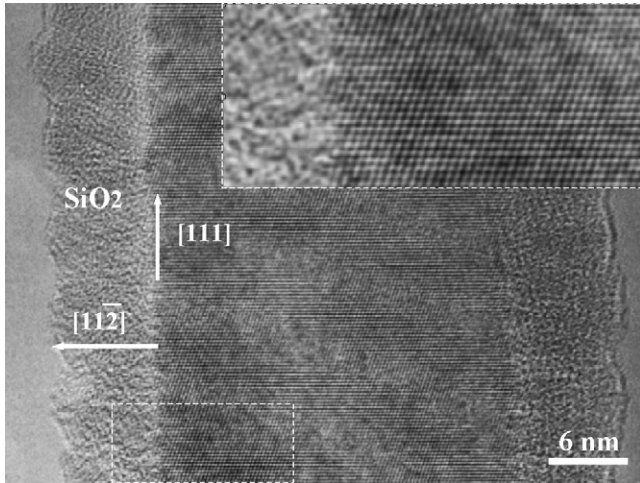


Fig. 43. HRTEM image of Si ribbon viewed along the zone axis of $[1\ 1\ 0]$. The ribbon axis is along the $\langle 1\ 1\ 1 \rangle$ direction and $\langle 1\ 1\ 2 \rangle$ is perpendicular to the ribbon axis.

in Fig. 44(b) shows a better contrast). This kind of contrast is visible only in certain orientations and it is not obvious in the bright field image.

In crystal growth, the density of dislocations needed to induce the fast growth of a bulk crystal is very low. For the nanosize crystals in nanowires or ribbons, one defect might be enough to enhance their growth. In fact, a high density of planar

defects has been frequently observed in Si nanowires and nanoribbons and this can be reflected in their electron diffraction patterns. (Fig. 44(c)) shows the electron diffraction pattern recorded with the electron beam perpendicular to a ribbon plane. The diffraction spots are very sharp and show hexagonal symmetry. If this is a $\langle 1\ 1\ 1 \rangle$ zone axis, the inner six diffraction spots should be $(2\ 2\ 0)$ with a d -spacing = 0.191 nm. However, the d -spacing of these diffractions is about 0.33 nm. The $(2\ 2\ 0)$ diffractions are actually the second inner most diffraction (see the indexes in Fig. 44(c)). By tilting the ribbon along the growth axis, the diffraction spots become very striking (Fig. 44(d)) indicating that the periodicity or the long range order of Si crystal along the direction perpendicular to the ribbon surfaces is broken. Si crystal in the ribbon should be sliced by stacking faults or twins. Obviously, these planar defects will largely enhance the sideway growth of the nanoribbon.

4.2. Structural transformation in nanowires

4.2.1. Surface relaxation and saturation of zinc oxide nanowires

Zinc oxide (ZnO) is a polar semiconductor with potential applications in electronics and optoelectronics, including sensors [174], field effect transistors [175], photodetectors [176] and nanolasers [177,178]. ZnO has a direct wide band gap

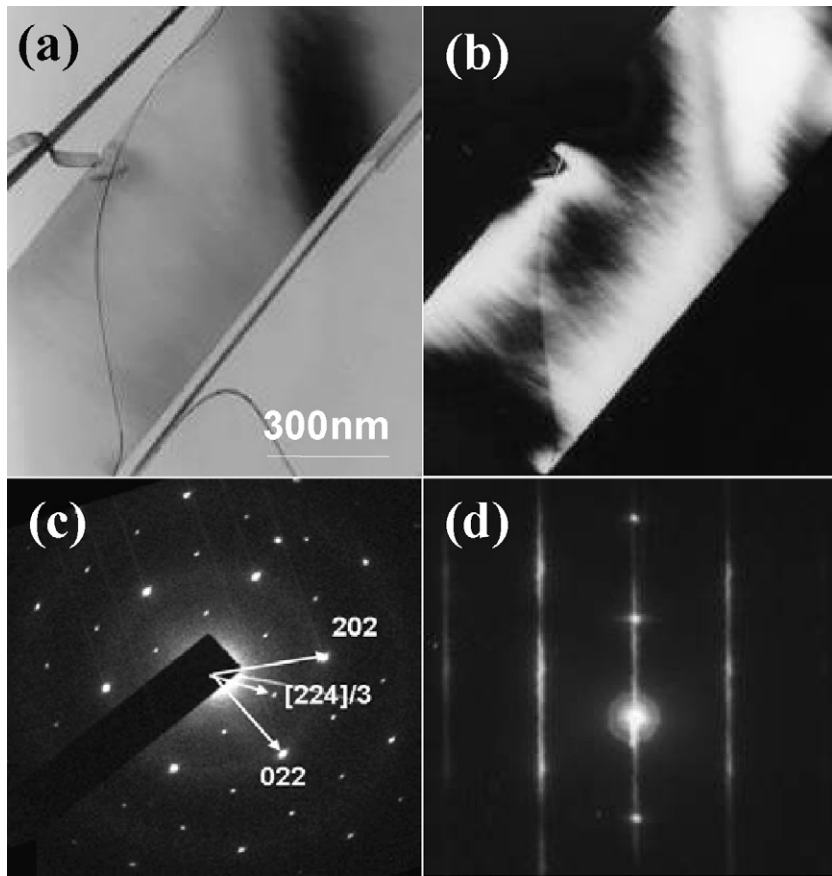


Fig. 44. (a) Bright-field and (b) dark-field images of Si nanoribbons. Electron diffraction patterns recorded (c) along the direction perpendicular to the ribbon surface and (d) along the direction almost parallel to the ribbon surface.

of 3.3 eV and a large exciton binding energy (60 meV) making it promising for high-efficiency blue and ultra-violet devices. The recent successful growth of highly ordered nanowires has expanded the list of potential applications. Although p-type doping is difficult to achieve in ZnO bulk, it was shown to be possible in ZnO nanowires, opening the doors for ZnO-based semiconductor electronics [179]. For sufficiently small nanowires, quantum size effects are expected to have a pronounced influence on all these applications. ZnO nanowires usually grow along the [0 0 0 1] direction and have hexagonal cross-sections [179,180]. Few theoretical investigations have been performed on small wires [181–183], mainly focusing on their elastic properties. For the structural and electronic properties of ZnO nanowires, our recent work [184] by DFT calculations showed that the relaxation on the surface plays an important role in stabilizing the nanowires. All nanowires show a semiconductor behavior. The band gap decreases as the size of the nanowire increases, while the shape of the band edges remains unaltered.

The relaxed structures of the studied nanowires are shown in Fig. 45. The nanowires A, B and C have 0.35, 1.0 and 1.65 nm in diameter, respectively. The Zn–O bond lengths along the c direction are obviously different on the surface and in the bulk region. Similar to what has been found for the (1,0,−1,0) surface, due to the buckle of the Zn–O atoms, the bond length along the [0 0 0 1] direction decreases to 1.88 Å. In the core region it remains very close to the bulk value (2.01 Å). Also along the basal plane, it decreases slightly to 1.95 Å. This trend is similar for all investigated wires. Relaxations for atoms in deeper layers are much smaller, as also found for the (1,0,−1,0) surface. In ZnO bulk, the two second-nearest neighbors of Zn atoms are apart by 3.2 Å. In the wires, due to surface relaxation, this distance is smaller, and has the values: 2.87 Å (wire A), 3.00 Å (wire B), 3.01 Å (wire C). The tilt angle of the surface Zn–O dimer is 7.60°, 10.40° and 10.96° for the wires A, B and C, respectively. The energy gained with the atomic relaxation is significant: 0.26, 0.16, and 0.11 eV/(ZnO unit) for the wires A, B, and C, respectively, contrary to the relaxation along the [0 0 0 1] direction that leads to very small energy gain (10 meV/cell). The wire formation energies decrease according to: 0.94 eV (wire A), 0.44 eV (wire B) and 0.30 eV (wire C), where the zero of energy is set to the calculated heat of

formation (at $T = 0$ K) of ZnO bulk, −3.02 eV, following a linear behavior and indicating that the edge effects are small and surface effects are dominant for this kind of wire.

During the surface creation process, one bond per atom is broken. The O 2p dangling bond points towards the direction of the missing bond. This feature is responsible for the insensitivity of the O surface atom to relaxation. The top of the valence band is formed mostly by O 2p (small contributions of the Zn 3d electrons are also seen), while the bottom of the conduction band has mostly Zn 4s character. All wires show a semiconducting character and a direct band gap at the Γ point. Qualitatively, the shapes of the band edges do not change, but individual bands are found to shift. The wire band gaps are 2.0, 1.5, and 1.1 eV for the wires A, B, and C, respectively, reflecting quantum confinement effects. The valence bands of wire A show a larger dispersion than the other two bigger wires due to the large surface/bulk ratio. In the case of wire A, the O 2p is slightly more localized than in the wires B and C. On the other hand, the surface atoms are somewhat different from the core atoms. Since the oxygen core atoms have one more neighbor than surface oxygen atoms, the O 2p state is much broader in the surface, reflecting a larger hybridization. The lowest empty state has mostly Zn 4s contributions, very similar to that in ZnO bulk.

The growth direction and shape controls provide the opportunities to tune various physical properties of the material, such as band gap, index of refraction, thermal and electrical conductivity, and piezoelectric polarization. ZnO nanowires usually grow along the [0 0 0 1] direction, having a hexagonal cross-section as described above. ZnO nanowires with a triangular cross section have been recently grown [185]. This particular shape can exhibit very interesting properties as it has been found for GaN nanowires [186]. Our recent first-principles density-functional calculations on [0 0 0 1] ZnO nanowires [187] showed that the surface relaxation is significant for the bare nanowires with triangular cross section. Hydrogen saturated wires show small relaxation and can have both semiconducting and metallic behaviors. The band gap of ZnO nanowires can be controlled by the thickness of the nanowires and by hydrogen adsorption. It is therefore suggested that hydrogenation leads to drastic changes in the ZnO nanowire electrical properties.

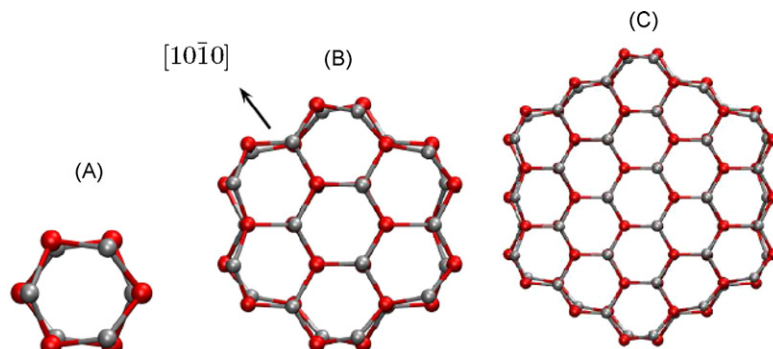


Fig. 45. Top view of the relaxed structures of the nanowires A, B and C. The grey (red) spheres represent Zn (O) atoms. (For interpretation of the references to colour in this figure legend, the reader is referred to the web version of the article.) [184].

4.2.2. The stability of Si nanowires

Nanowire growth is a non-equilibrium process. The stability of nanowires is crucial for technological applications. The as-prepared Si nanowires by the oxide-assisted or laser ablation method are very stable in air. Due to the thin oxide shells, no further oxidization occurs on Si nanowires that are stored in air for about 10 years. However, at elevated temperatures, the cylindrical shape of the nanowires is not stable under the influence of surface tension. By annealing treatment, Si nanowires have been observed to transform into nanospheres chains (see Fig. 46(a)). This transformation is accomplished via the spheroidization of Si nanowires of semi-infinite lengths. This process is determined by many factors, for example, the diffusion process, the annealing temperature, ambient pressure, initial Si nanowire diameters and the oxide state of the Si nanowire outer layers [188]. The uniform nanosphere chains consist of equally spaced Si crystalline nanospheres connected by Si-oxide bars (see Fig. 46(d)).

The transition from Si nanowires to Si nanosphere chains is accountable by considering the instability of the cylindrical shaped Si nanowires under the influence of surface tension at elevated temperatures. Rayleigh [189] first gave the perturbation analysis for inviscid fluids by assuming that the liquid cylinder had infinite length (no end effect) and determined the breakdown rate of a liquid cylinder into a row of spherical droplets. Nichols and Mullins [190] performed analogous treatment for the kinetic process of surface diffusion and volume diffusion. The stability of the cylinder shape is determined by the infinitesimal variation of the diameter or any longitudinal perturbation on the diameter of the cylinder with wavelength λ . The main results from these previous works are $\lambda = 2\pi R_0$ (where R_0 is the initial unperturbed cylinder radius) and λ_m (a function of the mass-transport mechanism). If the perturbation wavelength is $\lambda > \lambda_m$, the cylinder is unstable. For

$\lambda = \lambda_m$, the rate at which the perturbation develops has reached a maximum point. $\lambda_m = 58.89R_0$, $9.02R_0$, and $12.96R_0$ has been derived for surface, internal volume and external diffusion respectively, as the dominant transport mechanism [188]. It was observed that the temperature needed for this transition of thick nanowires is higher than that of thin ones. By increasing the annealing temperature, this results in an increase of the spacing between the neighboring Si nanospheres. This spacing is also dependent on the diameter of the original nanowire.

The diameter of the nanospheres increased accordingly in the annealing process due to the shape change from cylindrical to semispherical. The ratio of L/R was 6.0–6.4 (where L is the spacing between neighboring nanospheres and R the average lateral radius of the nanospheres), which deviated from theoretical calculations [190]. This is understandable because the structure of Si nanowires grown by the researcher's technique is cable-like instead of a single-phase homogeneous wire, that is, they are composed of a Si crystalline cylinder core and a thin Si-oxide shell. The spheroidization transition process may be divided into two steps (see Fig. 46(b)). First, the atoms in the inner Si core segregate periodically along the wire due to the perturbation wave. The driving force is the reduction of the interface/surface energy. Secondly, the diameters of Si nanospheres formed are larger than that of initial Si nanowires and the Si-oxide shells surrounding the newly formed Si spheres migrate towards the necks/bars. This can eliminate the interface of Si/Si-oxide and reduce the surface energy. The final spacing between Si spheres is then determined by the amount of Si-oxide. Since the formation of the nanospheres is limited by the opposite diffusion of Si and Si-oxide shell, the current experimental result should deviate from the ideal model of a single-phase cylinder. In particular, when Si nanospheres were formed, they were entirely separated from each other and the bars (connecting the spheres) consisted of only Si-oxide

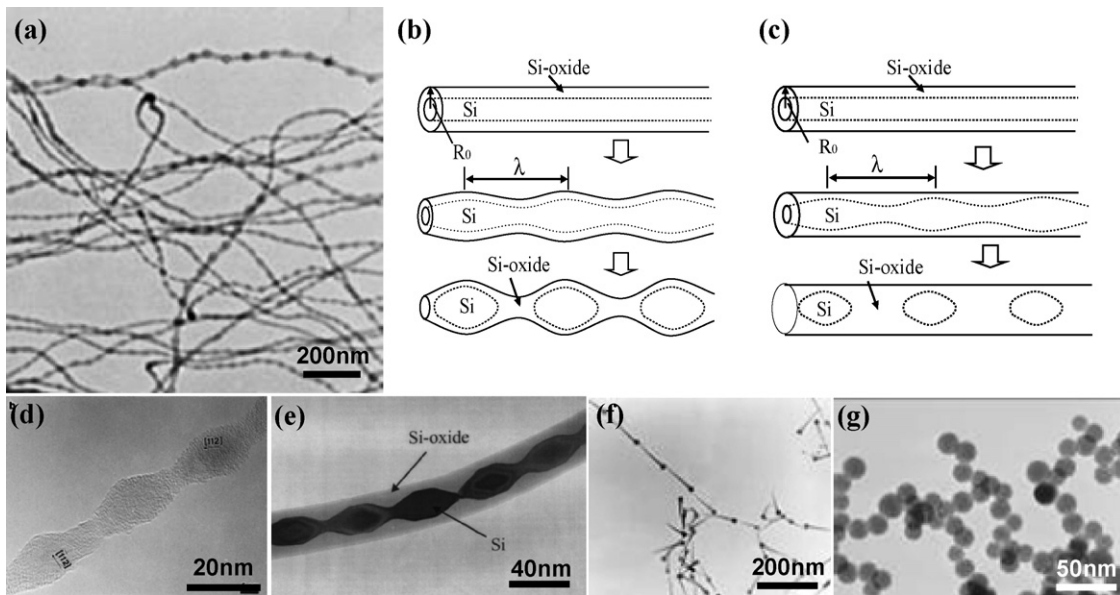


Fig. 46. (a) Si nanoparticle chains formed via the spheroidization S nanowires. (b) and (c) Models for the formation of Si nanoparticles by diffusion and oxidation, respectively. (d) and (e) Enlarged pictures of Si nanoparticle chains formed by diffusion and oxidation, respectively. (f) Further annealing of the nanosphere chains caused detaching of the Si nanospheres and the oxide bars changed into cone shapes. (g) Final product of spheres [188].

(Fig. 46(d)). It is believed that the oxide shell surface was in a semi-liquid state at the elevated temperature due to the lowering of the melting point by the nanosize effect. The results deduced from the perturbation consideration are reasonable. However, the final spacing between the spheres should be determined by the amount of the Si-oxide shell.

Further annealing of the nanosphere chains caused detaching of Si nanospheres and the oxide bars changed into cone shapes in order to further reduce their surface energy (Fig. 46(f)). Each Si nanosphere was attached with only one oxide tail. Again, this is due to the surface energy since two tails would have more surface area compared to the single tail. For lengthy annealing, the ultimate morphology of the Si nanowires was spheres as illustrated in Fig. 46(g)). If oxygen was sufficient, the spheres will totally convert into oxide spheres. Alternatively, with the presence of oxygen during the annealing, thick Si nanowires could transform into sphere chains in a non-diffusion mode. This could have resulted because the effective melting temperature for thick nanowires was low. Shown in Fig. 46(d), the Si core in a nanowire was truncated/etched periodically by the oxide shell. Notice that the outer diameter of the oxide shell was unchanged. It is believed that oxidation was selective because of the mismatch stress between the oxide shell and the Si core. This phenomenon is an analogy to the case of the interface stress that occurred between the hetero-junction where mismatch exists. Dislocations are generated periodically along the interface in order to release the interface stress. For the case of Si/Oxide shell, oxidation occurred rapidly with the assistance of the interface stress and this resulted in the morphology of the Si sphere chains.

4.2.3. Optical rapid annealing effect

The as-prepared Si nanowire samples are stable in air. A gas flame cannot ignite Si nanowires. However, the nanowires slowly oxidized in the flame, forming silica nanowires. When exposed to a camera flash, Si nanowires absorb the photo energy effectively and the temperature of the nanowires could be over 1000 °C instantly. This causes an ignition of Si nanowires and they fiercely burn down (see Fig. 47(a)).

The light power needed for the ignition in Ref. [74] was 0.1–0.2 J/cm². The pulse duration was about 5 ms. It is obvious that Si nanowires absorbed and confined the energy from the flash, resulting in a sufficiently high temperature and hence, leading to an instantaneously fierce oxidation. The ignition was found to start at certain areas of the sample and then the fierce burning propagated the entire sample. The remaining materials consisted of various forms of SiO₂ nanostructures, for example, particles, wires and tubes (see Fig. 47(b), (d), and (e)). When flashing the Si nanowires with a low light power, a large audible acoustic wave, that is, an optoacoustic effect was observed. Large optoacoustic effects, resulted from the absorption of the incident light, also occurred in Ge and B nanowires. However, TiO₂, ZnO and SiO₂ nanowires (all transparent to visible light) did not show an obvious optoacoustic effect.

When the flashing experiment was performed in inert gases, no ignition occurred. Flashing Si nanowires in Ar or He, resulted in structural transformation from nanowires to nanoparticles. As illustrated in Fig. 47(d), Si nanoparticles were embedded in the Si-oxide nanowires. It was believed that the Si cores suddenly transformed into a melting state after flashing and subsequently, segregated into crystalline Si nanoparticles in milliseconds. Therefore, the temperature within the Si cores might be 1000–1500 °C (Si melting point 1414 °C, Si nanowires were formed at about 1000 °C). However, Si nanowires with diameters greater than 40 nm cannot be easily ignited. The high temperature generated from burning the Si cores in air produced SiO₂ particles. Since thicker silicon oxide shells protected Si cores from oxidation, some Si nanowires might ignite like blast fuses. For those Si nanowires with thick oxide shells, the Si cores might not be fully oxidized. They should react with the shells as described by the following reaction:



In vacuum, similar reaction could also occur. The temperature needed for this reaction should be higher than 1200 °C, and the resulting materials could be Si monoxide that has much greater volatility than silica. If the resulting Si monoxide is volatilized

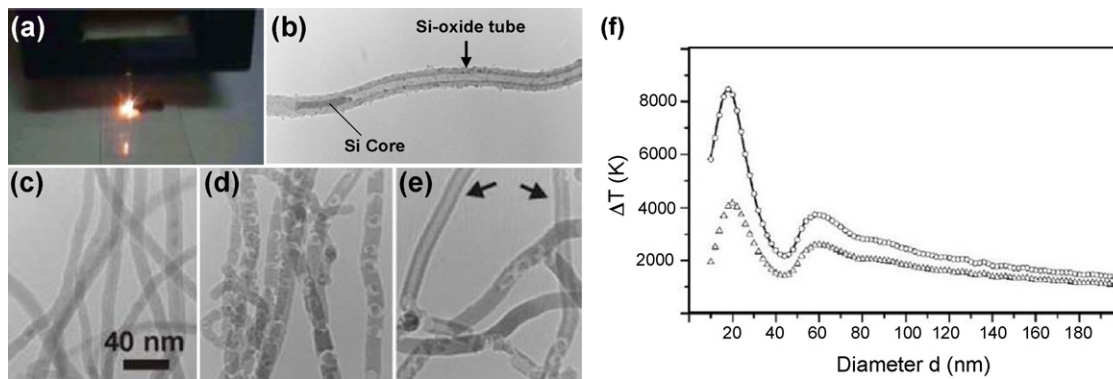


Fig. 47. (a) Burning of Si nanowires soon after flashing in air. (b) Si nanowires ignite-like blast fuses, resulting in Si-oxide tube structure in air [74]. (c) The original Si nanowires. (d) Si nanowires change to Si nanoparticles after flashing in Ar. (e) Si-oxide nanotubes formed by flashing the Si nanowires in vacuum. (f) The temperature rise ΔT vs. the nanowire diameter. The solid line indicates the ideal case when the photo energy absorbed from the flash is totally converted into heat. The open circles are the results if the nanowire is coated with 2 nm of silica. The triangles indicate the results calculated by considering heat dissipation (data (f), courtesy of Prof. C.T. Chan [195]).

during burning, then silica nanotubes are formed (see Fig. 47(b)). When the flashing experiment was done in vacuum, the molten Si cores or Si monoxide easily evaporated. This could be the reason that the remaining materials, after flashing Si nanowires in vacuum, contained many long silica nanotubes.

The exceptional photothermal effect that cannot be observed in bulk materials is another unusual phenomenon that is not only present in Si nanowires, but also in many nanoscaled materials. Similar photothermal effects have been previously reported in single-walled carbon nanotubes [191]. Using the enhanced photo thermal effect, Huang et al. demonstrate a new method for flash welding of conducting polymer nanofibres [192]. Under flash irradiation, polyaniline nanofibres ‘melt’ to form a smooth and continuous film from an originally random network of nanofibres. Therefore, this photothermal effect has potential technological application, for example, to melt-blend polymer–polymer nanocomposites rapidly and to photo-pattern polymer nanofibre film (see Fig. 48). The flash welding technique may open new avenues for processing and patterning polymer-based materials and devices [193].

Flashlight emulates sunlight and mainly consists of visible light. This raises a question about nanowires that capture so much energy from light. Recently, some theoretical considerations provided hints towards the understanding of the enhanced photothermal effect in Si nanowires. The increase of the absorption coefficient of a material means that the dielectric constant of the material may increase. Due to the quantum confinement effect in Si nanowires, Nishio et al. [194] report that the imaginary part of the dielectric constant of Si in the core of a Si nanowire is larger than the rest of the Si atoms in the nanowires. Another report by Ding et al. [195] reveals that a significant photothermal heating occurs when the diameter of the nanowire is about 20 nm. The optical ignition of Si nanowires can be explained entirely within the domain of the classical Maxwell theory. This analysis is based on the assumption that the nanowire is a blackbody although the diameter of the nanowire is much smaller in comparison with visible wavelengths. Si nanowires are presented by infinite length cylinders since their lengths are very long compared with their diameters. The ability of nanowires to absorb or scatter incident light can be characterized by the absorption and

scattering efficiencies, $Q_{\text{absorb}} = \sigma_{\text{absorb}}/G$ and $Q_{\text{scatt}} = \sigma_{\text{scatt}}/G$, where σ_{absorb} and σ_{scatt} are total absorption and scattering cross sections per unit length of the cylinder nanowires respectively, and G is the geometric cross-section of the cylinder per unit length ($G = \text{nanowire diameter}$). It is expected that both the dispersive permittivity (ϵ) and the structural resonance contribute to Q_{absorb} and Q_{scatt} . Both Q_{absorb} and Q_{scatt} are dependent on the wave length of the incident light. As the nanowire diameter increases, the absorption peak position shifts to the long-wavelength regime. By fixing the wavelength of the incident light, Ding et al. [195] obtained that the absorption efficiency oscillated with the variation of the nanowire diameter, and the scattering efficiency showed similar structure of oscillations with the diameter. It is shown that Si nanowires can have an absorption cross section that is even larger than the geometric cross section because of the resonance which is unique to the cylindrical geometry of the nanowires. The total scattering cross section per unit length of the cylinder nanowire is given by [195]:

$$\sigma_{\text{scatt}} = \frac{4}{k_0} \sum_{m=-M}^M |D_m|^2 \quad (4.2.2)$$

The total absorption cross section per unit length is

$$\sigma_{\text{absorb}} = -\frac{4}{k_0} \sum_{m=-M}^M [\text{Re}(D_m) + |D_m|^2] \quad (4.2.3)$$

where k_0 is the wave vector for the light in air and D_m is the scattering coefficient. The temperature rise ΔT of a Si nanowire induced by the absorption of the incident light from the photographic flash is

$$\Delta T = \frac{I_0 \sigma_{\text{absorb}}}{\rho C_p V} \quad (4.2.4)$$

where I_0 is the intensity of the incident light, ρ the density of Si, C_p the specific heat of Si, and V is the volume of the Si nanowire per unit length. It is found that the resonant absorption constitutes one of the most important elements in nanowire light absorption and heating. In Fig. 47(f), the calculated temperature increase induced by the absorption of incident light is plotted as a function of the nanowire diameter. The highest temperature rise ΔT is attained at the diameter $d = 20$ nm. ΔT decreases rapidly if $d > 20$ nm. The scattering coefficient can be described by $D_0 = -i(\pi/4)(k_0 r)^2(1 - \epsilon)$, and the absorption cross section per unit length is $\sigma_{\text{absorb}} = \pi k_0 r^2 \text{Im}(\epsilon)$. The absorption efficiency $Q_{\text{absorb}} = \sigma_{\text{absorb}}/G = (\pi/2)k_0 r \text{Im}(\epsilon)$. Hence, the energy that it absorbs per unit length is proportional to nanowire’s radius (r), while the number of atoms shares the absorbed energy $\sim r^2$ per unit length. The temperature rise (Eq. (4.2.4)) should then be $\sim 1/r$. Small diameter nanowires should be easily heated up in comparison with large ones. The large photo energy confinement effect in Si nanowires is unusual. This effect is also indicative in applications such as smart ignition systems, self-destructing systems for electronic devices, nanosensors, and nanostructural or nanophasic refor-

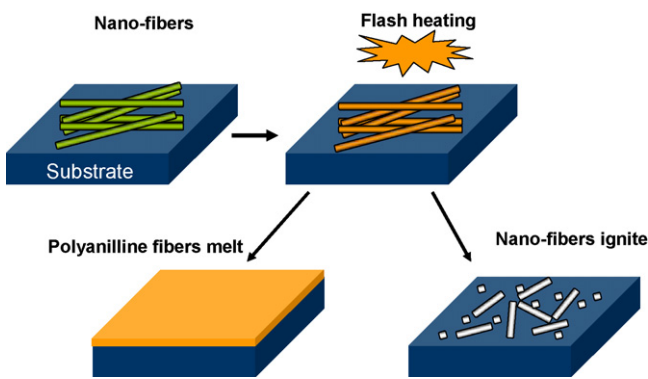


Fig. 48. On exposure to a flash of light, nanofibre’s morphology changes due to the enhanced photothermal effect (redraw after Ref. [193]).

mation. More properties of metallic and semiconductor nanowires are given in reviews and books [196,197].

4.3. Contacts and heterostructures in nanowires

4.3.1. Metal-semiconductor contacts

To realize the many potential applications of semiconductor nanowires in electronic circuits or sensor devices, the contacts or interface structures formed between nanowires and metals are important issues in nanotechnology. Si nanowires, for example, can react with metals to form nano contacts or metal silicides. Au has frequently been used as the leads because Au and Si can easily form solid solutions. The melting temperature of Au–Si alloy can be much lower than that of Si or Au and the contacts formed by Au are unstable at a high temperature. Interdiffusion often occurs in nanowires. Fig. 49(a) shows the Au particles deposited on a Si nanowire [198]. Since the oxide layer on the nanowire was removed before deposition, Au particles on the nanowire surface easily reacted with Si. Even if a thin Si oxide layer existed on the surface of a Si nanowire, Au could also diffuse through the thin oxide shell when heated at 500 °C (Fig. 49(b)). At a higher temperature of about 800 °C, the Au particles totally diffused into the nanowire and totally immersed at atomic levels, offering excellent electrical contact.

Furnace annealing of Au-coated Si nanowires could be used to synthesize crystalline gold nanowires (AuNWs) embedded in a SiO_x sheath [198]. The AuNWs with the diameters of around

10 nm can be produced by using silicon nanowires as the template as seen in Fig. 49(c) and (d). Due to the softening of Si nanowires upon oxidation and the increasing Au diffusion at elevated temperatures, the AuNW was formed, and the formation mechanism of the AuNWs is shown in Fig. 50. First, the deposited Au nanoparticles attached on the surface of a Si nanowire. Upon heating the coated Si nanowires, the Au nanoparticles tended to move into the core, together with the motion of the Si–SiO_x interface of the wire so as to reduce the surface area and thus the surface energy. As the annealing temperature was slightly below the melting point of Au, the Au nanoparticles would be in a semi-liquid state. The crystalline structure of silicon was changed to an amorphous structure soft enough to allow the diffusion of Au nanoparticles into the core of the nanowire. The SiO_x overlayer of AuNWs can be readily removed by HF etching to expose the AuNWs, if necessary. Thus, the furnace annealing of Au-coated Si nanowires offers a simple method of synthesizing thin and large quantity crystalline Au nanowires. The synthesized AuNWs should find interesting applications in nanodevices.

Metal silicides are promising candidates as electrical contacts for silicon nanowires because of their excellent properties, such as high thermal stability, good compatibility with Si and no electron migration effect. Several methods have been developed to convert the nanowires to metal silicides. Li et al. [199] used a metal vapor vacuum arc (MEVVA) ion source implantation to synthesize NiSi₂/Si and COSi₂/Si on the surface

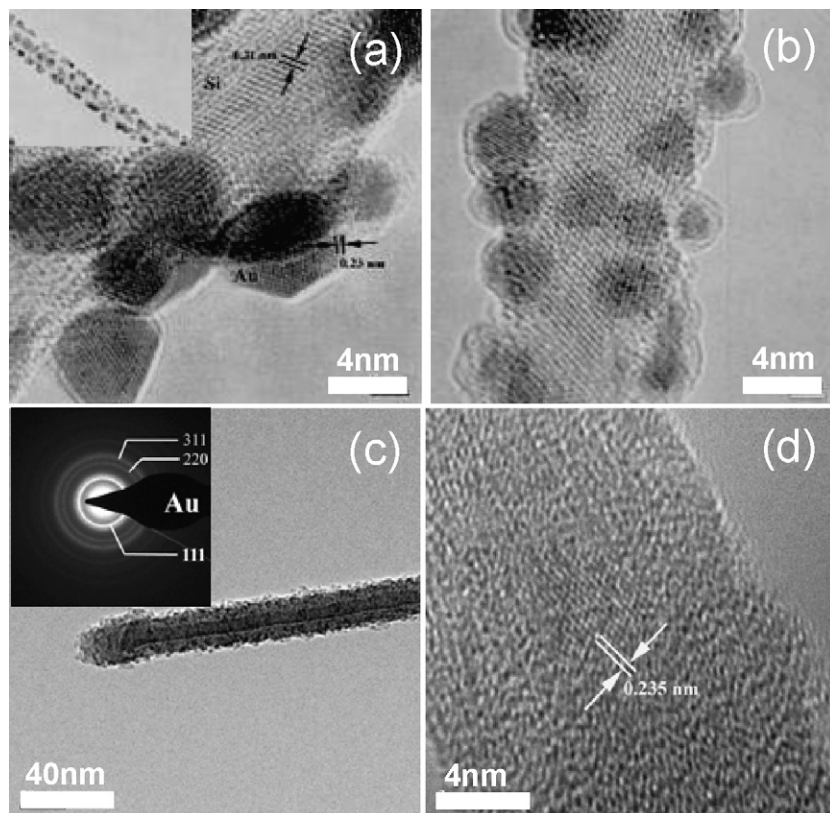


Fig. 49. TEM images of Si nanowires (a) coated with Au nanoparticles, (b) after annealing at 500 °C for 1 h. (c) Au nanowire inside SiO_x sheath formed by annealing of the Au-coated Si nanowire at 880 °C for 1 h at 10⁻² Torr (inset shows the electron diffraction pattern), and (d) the corresponding HRTEM image showing the Au core [198].

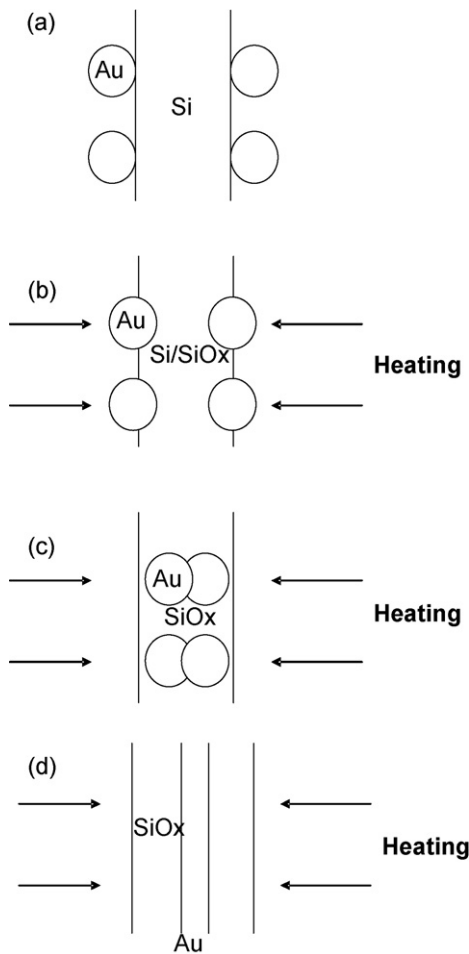


Fig. 50. Schematic diagrams showing the formation mechanism of AuNWs by furnace annealing: (a) Au nanoparticles deposited by argon ion sputtering are attached on the surface of a Si nanowire, (b) oxidation of Si nanowires and diffusion of Au nanoparticles into Si nanowires under heating, (c) diffusion of Au nanoparticles in the SiO_x matrix of the nanowire at elevated temperature (e.g. 880 °C), and (d) formation of AuNW in the SiO_x matrix [198].

of bare silicon nanowires. The formation mechanism of NiSi₂ and CoSi₂ is schematically shown in Fig. 51. At room temperature, the as-grown Si nanowires were implanted with Ni⁺ or Co⁺ ions in a relatively high dose (Fig. 51(a)). Since the incident ion beam is directional, only the side of the sample facing the ion beam was implanted. The morphology of Ni-implanted Si nanowires consists of a one-side coated nanowire structure. Upon rapid thermal annealing at 500 °C, the surface of the Ni-implanted Si nanowires was smoothed, and the implanted side of the Si nanowires was transformed to a continuous outer layer with a typical thickness of about 8 nm. The SiO_x layer of Si nanowires was no longer detected after the implantation, which suggested that the SiO_x layer of Si nanowires was probably removed by the metal ion implantation. The implanted ions combined with the Si crystalline core to form a mixture of metal/Si (or clusters). The energy of the ion beam is critical since overly high ion energy would result in excessive damage to the Si nanowires. It was found that 5 kV ions were optimal for the formation of metal/nanowire structures. The metal/Si layers contained a high density of defects or structural damage after the ion implantation. To reduce the defects in the metal/Si layer, annealing of the as-implanted wires at a high temperature (500–600 °C) was necessary. The quality of the Ni/Si layers (Fig. 51(e)) was largely improved. It has been demonstrated that the structure of the metal silicide layer is sensitive to the annealing temperature. Under appropriate conditions, the layer would be well oriented with respect to the nanowire core. This approach to the synthesis of metal silicide/Si nanowires can be potentially useful to fabricate electrical contacts to Si nanowires and improve the electrical conductivity of Si nanowires. Under proper annealing conditions, the metal silicide layer can exhibit a highly oriented relationship.

Using a novel technique of point contact reaction (see Fig. 52) between metal and Si nanowires, it has been demonstrated that Si nanowires can be transformed into a

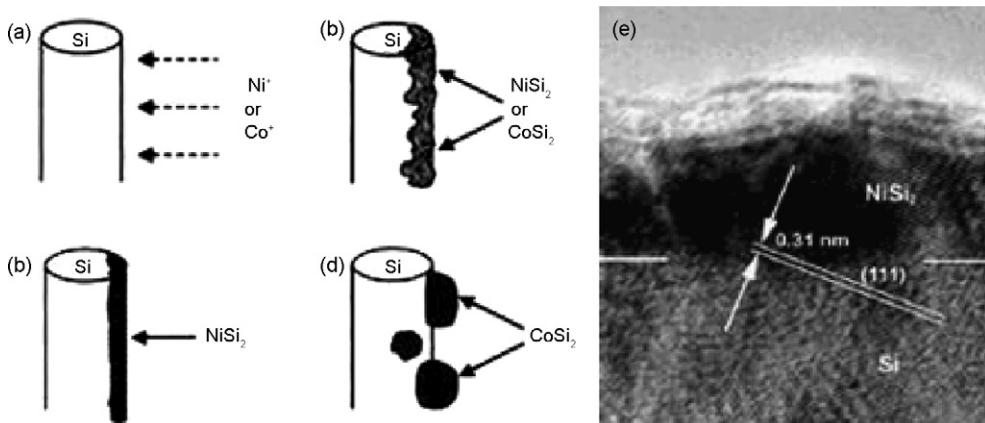


Fig. 51. The formation mechanism of NiSi₂/Si and CoSi₂/Si on the surface of bare Si nanowires. (a) Bare Si nanowires implanted with metal ions. (b) Formation of the metal/Si mixture layer on one side of Si nanowire. (c) The NiSi₂/Si nanowire after low temperature annealing. (d) CoSi₂ nanoparticles formed by coarsening at high temperature annealing. (e) HRTEM image of a Ni implanted Si nanowire after annealing. The implantation was carried out with Ni ions at a nominal dose of $1 \times 10^{17} \text{ cm}^{-2}$ using an extraction voltage of 5 kV at room temperature [199].

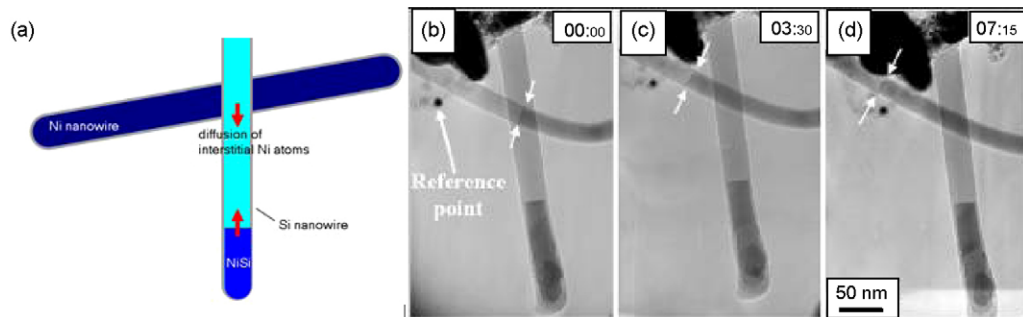


Fig. 52. (a) Schematic illustration of growth of NiSi by the point contact reaction. (b)–(d) The growth of NiSi formed at the tip of Si nanowire. No NiSi formed at the contact point of the Si nanowire (from Ref. [201]; reproduced with permission from American Institute of Physics).

single crystalline metal-silicide nanowire with an epitaxial interface which has no misfit dislocation [200–202]. The growth of the NiSi nanowire through point contacts shows an interesting behavior. Ni atoms first dissolve into the Si crystal and then diffuse to the ends (tips) of the nanowire, where SiNi nucleated and grew (see Fig. 52(b)–(d)). SiNi did not form at the contact point. It was believed that Ni atoms diffused interstitially in the nanowire from the contact point to the epitaxial interface. However, it is also possible that Ni diffused along the surface of the nanowire. The single crystal SiNi grew and transformed Si nanowire linearly with time. The interface between the SiNi and Si appeared atomically flat during the growth [201]. The reaction with a linear rate could be an interface-controlled reaction. Since the formation of SiNi was on both ends of the nanowire, this novel reaction enables the fabrication of single crystal NiSi/Si/NiSi heterostructures with atomically sharp interfaces as building blocks or function units for nanoscale devices [202].

As an effective method for making electrical contacts on a semiconductor nanowire, focused-ion beam (FIB) deposition has been widely used. As a consequence of high energy Ga ion beams, the crystal structure of the nanowire is generally highly damaged (see Fig. 53(a)). The thickness of the damaged layer for Si nanowires is typically 20 nm. The atoms in this layer are highly disordered. The concentration of Ga is about 2% as detected by the energy dispersive X-ray spectrometer. The commonly used electrode materials for FIB deposition are Pt

and W. As shown in Fig. 53(b), the as-prepared Pt electrode consists of Pt particles. There is a high concentration of carbon in the electrode [203]. The Pt(Ga)/C material consists of Pt particles (size < 3 nm), which are sheathed with Ga+-doped amorphous carbon layers. The conductivity of as prepared Pt electrodes is poor. By annealing treatment, the conductivity can be improved.

4.3.2. Heterostructures in nanowires

Heterostructured nanowires are important nanostructures for creating various functional devices with low dimensionality, for example, 1D quantum devices, p–n junctions and unipolar/bipolar transistors. Based on the VLS mechanism, longitudinal heterostructured nanowires can, in principle, be grown by switching between different source materials. With non-VLS syntheses, it is difficult to produce longitudinal heterostructured nanowires. Heterostructured nanowires of Si/SiGe have been synthesized using hybrid pulsed laser ablation/chemical vapor deposition by Yang's group at Berkeley [204]. In this synthesis, the Si and Ge vapor sources were independently controlled. The resulting nanowires were a Si/SiGe superlattice. Using a similar method, Lieber's group prepared GaAs/GaP heterostructured nanowires [156,205]. Solanki et al. [206] reported a method to prepare ZnSe/CdSe superlattice nanowires. Using Au-catalyzed chemical beam epitaxy, InAs/InP heterostructures were reported by Samuelson's group at Lund University [207]. The interfaces between InAs and InP

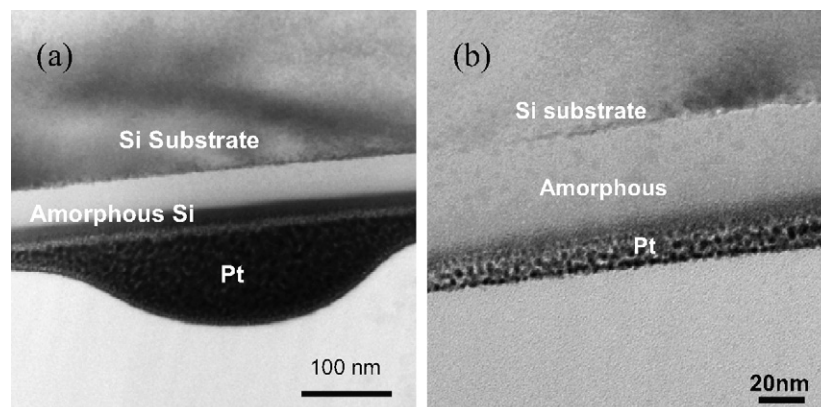


Fig. 53. (a) The interface structure between Si and Pt deposited by the FIB. (b) Enlarged picture of the interface area. The damaged layer is amorphous and Pt layer is in the form of clusters.

appeared to be atomically sharp and the growth direction was [0 0 1], which is different from that of most thick nanowires of cubic semiconductor materials.

The growth technologies for thin film heterostructures have been well developed and widely used to fabricate electronic devices. However, for growing ultra-thin heterostructured nanowires (diameter < 10 nm), the main problems are ways to interrupt the process and switch source materials. This is because the newly added material is not directly deposited onto the growth front of nanowires. The conditions for incorporation of the newly added source into the catalyst droplet, for example, the interruption time, temperature, vapor pressure, etc., strongly affect the quality of the heterostructured wires. Relying on the material systems, the abruptness of the interface is limited by the intermixing of the two source elements (assume that the hetero-junction consists of materials I and II) as well as the solubility of the source materials in the catalyst droplet. For most semiconductor material systems, the junction widths are always graded, with a width which is a fraction of the wire diameter [208]. As shown in Fig. 54(a), at any temperature above the eutectic point, there are always residual source materials in the droplet. At the onset (the beginning of growing material I on a nanowire containing only material II) of heterostructure growth, the residual materials in the liquid catalyst droplet will be mixed together. Therefore, the chemical composition gradient will occur at the interface. The concentration of the residual materials will decrease gradually and the concentration of the newly added sources will increase gradually.

Li et al. [208] have developed a model to describe the concentration gradient at the transition in hetero-junction and p-n-junction nanowires formed by the VLS reaction. The fraction of element II can be described by $c_{II}^s = \alpha[1 - \exp(-(3/\beta\gamma^3 c_0)(vt/r_s))]$, where c_0 is the fractional (I + II) concentration in the liquid droplet; γ the ratio of the radii of the liquid droplet and the nanowire; β a constant between 2 and 4, a geometry factor of the hemispherical droplet; r the radius of the nanowire; α the II source strength and v the vapor source flow rate. vt is the length of nanowire

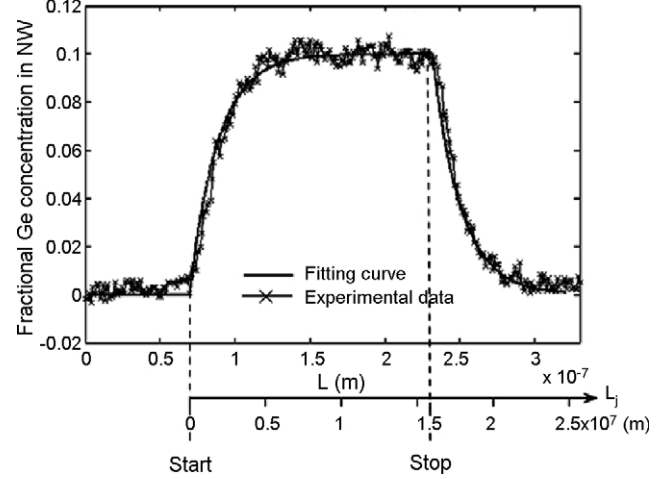


Fig. 55. The concentration profile measured in the transition region of a Si-Ge hetero-junction and the simulation result based on the model developed by Tan et al. (data from Ref. [208,209]; courtesy of Professors J. M. Redwing and T.Y. Tan).

grown since the hetero-junction. They demonstrated that the abruptness is not only material dependent, but also diameter dependent [206]. In principle, it is impossible to grow a hetero-junction with a junction width on the monolayer scale via the classical VLS method in the Si/Ge system (Fig. 54(b)). This is mainly due to the solubility of the semiconductors in the liquid metal droplet. With an Au catalyst, Si and Au can form a solid solution for all Si content (0–100%). However, for some III–V elements, hetero-junctions with satisfactory sharpness may be fabricated (Fig. 54(b)). For Si/Ge heterostructured nanowires, experimental results show that the gradient concentration profile in the transition region [209] matches fairly well with above theoretical prediction (Fig. 55). Nanowire p-n junctions fabricated by the VLS process should have similar growth behavior. The junction width is determined by the doping strength. Higher doping strength may result in sharper junctions.

The growth of heterostructured nanowires often fails because of (1) the absence of abrupt interface formation and (2) changes to the axial growth direction. The latter may cause

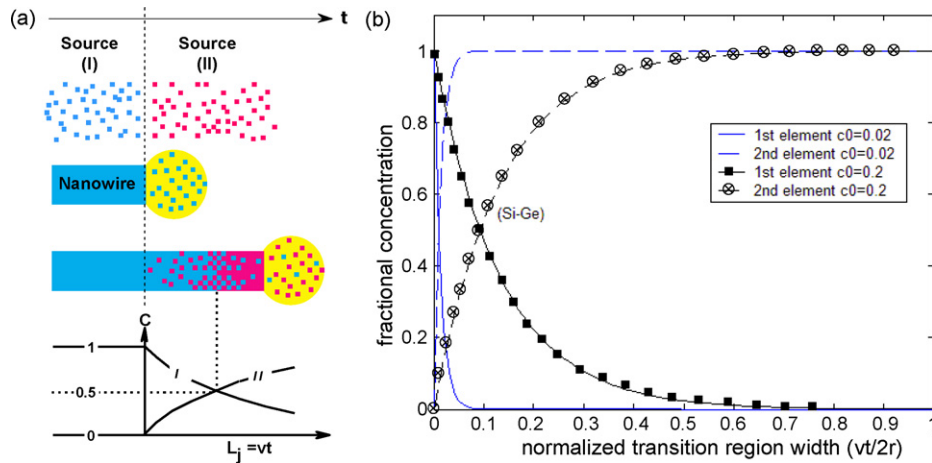


Fig. 54. (a) Schematic diagram showing the growth process of the heterostructured nanowires through the VLS growth. (b) The simulated concentration profiles in the transition region for different semiconductor solubility in Au (from Ref. [208]; courtesy of Prof. T.Y. Tan).

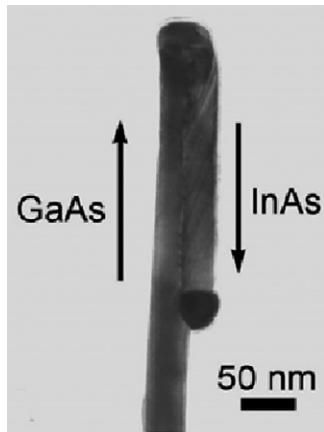


Fig. 56. TEM images showing the failure growth of the InAs/GaAs heterostructure. InAs nanowire catalyzed by the Au catalyst grows downward (from Ref. [210]; reproduced with permission from American Institute of Physics).

branch or downward growth. Paladugu et al. reported the evolution of InAs branches in InAs/GaAs heterostructured nanowires (see Fig. 56) [210], and explained that the change of the interface energy at the metal droplet caused the change in growth direction. The axial nanowire growth of heterostructures uses two elements A and B via the VLS mechanism with a metal catalyst C. If the interface energy between A and C is higher than that between B and C, the growth of A on B fails, whereas the growth of B on A is feasible. Although the axial growth of the nanowire fails, the branched wires or downward growth of the junction structures may have potential technological applications in nanodevice design and fabrication.

5. Other challenging nanowire structures

Material surfaces become extremely important when their sizes are reduced to the nanometer range. The smaller the size of the structures, the more significant the surface effect is. The surface effect could not only alter the materials properties such as electronic, electrical, optical properties that are determined directly by their electronic behaviors and affected by the well-known quantum confinement effect, but also cause structural stability problems, resulting in plenty forms of structures and thus offering a variety of opportunities for theoretical and experimental explorations. The surface saturated nanostructures usually retain their bulk structural configurations, whereas the surface unsaturated or partially saturated ones could adopt a huge number of possible structures that correspond to their local minima, without keeping their bulk structural features. This is particularly true for semiconductor nanostructures including nanoparticles and nanowires. A study of the structures of fully and partially hydrogenated Si nanocrystals and nanoclusters using an empirical tight-binding method by us [211] showed that the structural properties of the hydrogen saturated Si nanocrystals have little size effect, contrary to their electronic properties. The surface relaxation is small in the fully hydrogen saturated Si nanocrystals. Only the atoms in the outermost two or three layers exhibit small lattice contractions

of 0.01–0.02 Å. The surface relaxation is mainly dependent on the local environment, while the overall size and shape of the nanocrystals has little effect. Inside the hydrogenated Si nanocrystals, there is very small lattice expansion of the order 10^{-4} to 10^{-3} . Simulated annealing showed that the fully hydrogenated Si nanocrystals are the most stable structures compared to those partially hydrogenated. Removing up to 50% of the total terminating H atoms caused lattice distortions to the crystal structure, while the tetrahedral structures are retained. By removing more than 70–80% of the total terminating H atoms, the clusters will evolve to more compact structures, losing the tetrahedral bonding features. The effect is size-dependent [145]. For small- and intermediate-size hydrogen-free clusters (e.g. <200 atoms), the energetically favorable structures obtained are far from tetrahedral and may consist of small subunits like Si_{10} and Si_{12} . For spherical silicon nanocrystals, the surface atoms reconstruct to minimize the number of dangling bonds, forming a continuous surface. The large curvature of the continuous surface causes lattice contraction in the nanocrystals. Tight-binding calculations predicted the lattice contraction to be inversely proportional to the particle radius. The structural transition to bulk diamond structure in nanosized silicon clusters was estimated to occur in the range of 300–500 atoms, or about 2.3–2.7 nm in diameter.

As described below, without any surface or dangling bond saturation, the various nanosized structures such as nanowires involve a lot of local minima and could adopt many interesting configurations, therefore attracting intensive theoretical works and allowing fruitful predictions of the possible structures, although these structures remain challenging for experimental synthesis or fabrications. Although these structures are extremely challenging for experimental synthesis using the previously described techniques, some of them might be achieved in vacuum using the surface saturated nanostructures such as oxide covered silicon nanowires. By removing the surface layer and with the assistance of thermal annealing, the nanostructures could develop and adopt some of the predicted nanostructures described below.

5.1. Non-tetrahedral Si nanowires

Theoretical investigation of the atomic structures of the silicon nanowires is fundamentally important for their overall growth mechanism and properties. The surface-unsaturated Si nanowires involves significant structural transformation with environment changes and offers plenty of structural models that have been explored theoretically in the past several years. Although the Si nanowires with their surfaces saturated by atoms, small species, or small molecules are of more practical significance, the unsaturated Si nanowires composed of purely silicon atoms are also interesting and have received intensive studies in the past several years, because of their diverse structures.

Among the possible structures for Si nanowires predicted [212–221], Menon and Richter have reported the quasi one-dimensional structures of Si by using a generalized tight binding molecular-dynamics scheme [212]. They proposed the

Si nanowire geometries of whose surfaces closely resemble one of the most stable reconstructions of the crystalline Si surfaces with a core of buck-like fourfold coordinated atoms. In the work of Marsen and Sattler [213], the wires of 3–7 nm in diameter and at least 100 nm long tend to be assembled in parallel in bundles, and a fullerene-type Si_{24} -based atomic configuration for the nanowires was proposed. In an early work [214], we studied the geometric structures of thin short silicon nanowires consisting of tricapped trigonal prism Si_9 subunits and uncapped trigonal prisms, as shown in Fig. 57. These structures are the thinnest stable silicon nanowires and much more stable than the silicon nanotubes built analogously to small carbon nanotubes. In the work of Zhao and Yakobson [215], the energetics of formation of Si nanowires with crystalline and polycrystalline cores were compared and they suggested that for very thin (1–3 nm) nanowires, polycrystalline structure is lower in energy than the single crystal structure observed in experiments. Recently, they reported that a polycrystalline silicon wire of fivefold symmetry, rather than single-crystal types, represents the ground state for diameter less than 6 nm [216]. Menon et al. [217] compared the

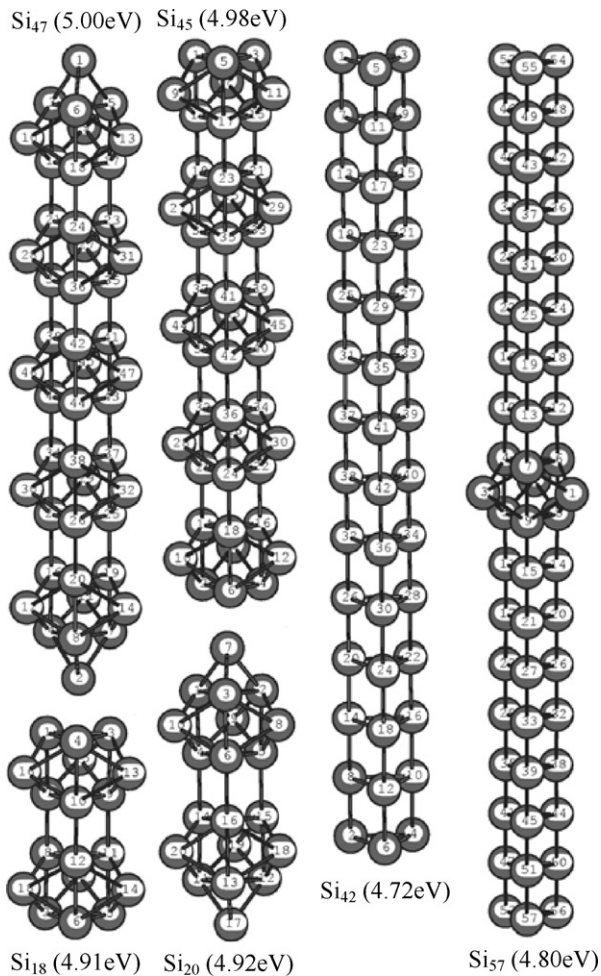


Fig. 57. Stable structures of selected Si clusters and wires. Si_{18} , Si_{20} , Si_{45} , and Si_{47} correspond to the stacked structures from the tricapped trigonal prisms. Si_{42} consists of the trigonal prisms. Si_{57} refers to the stacked trigonal prisms inserted among trigonal prisms by one tricapped trigonal prism. The binding energy per atom is included in the parenthesis [214].

tetragonal and cage-like or clathrate nanowires of Si and suggested that cage-like nanowires possessing lower density can maintain their structural integrity over a larger range of strain conditions than the tetrahedral nanowires. Kagimura and coworkers investigated several structures of pristine Si and Ge nanowires with diameters between 0.5 and 2.0 nm, and they reported that diamond-structure nanowires are unstable for diameters smaller than 1 nm. Filled-fullerene wires are the most stable for diameters between 0.8 and 1 nm, and a simple hexagonal structure is particularly stable for even smaller diameter [218]. In a series of annealing molecular dynamics simulations [219], Nishio et al. have shown a novel polyicosahedral nanowire which is energetically advantageous over the pentagonal one for a wire whose diameter is less than 6.02 nm. Cao et al. have performed extensive *ab initio* studies to search for stable geometries of $\langle 1\ 0\ 0 \rangle$ Si nanowires and reported that Si nanowires with diameters smaller than 1.7 nm prefer to adopt a shape with a square cross section [220]. By using a global optimization method Fthenakis and coworkers have found 17 optimum Si_{38} fullerene isomers constructed with permutations among their pentagons and hexagons [221]. The isomer with three distinct fused quadruples of pentagons is energetically optimal.

Although surface unsaturated silicon nanostructures favor non-tetrahedral configurations, the strong sp^3 hybridization of Si does not facilitate the formation of tubular structures, contrary to the ease of formation of the well-known carbon nanotubes which adopt sp^2 hybridization of carbon. Therefore, synthesis of hollow one-dimensional silicon nanotubes (SiNTs) is difficult due to the sp^3 hybridization in silicon, other than sp^2 hybridization in graphite. Despites of the obvious difficulty, the possibility of the existence of SiNTs similar to the conventional carbon nanotubes (CNTs) had been intensively studied theoretically by many groups [222–229]. For instance, Fagan et al. [222] established theoretical similarities between silicon and carbon nanotubes. Their results showed that the electronic and structural properties of SiNTs are similar to those of CNTs, i.e. they may exhibit metallic or semiconductive behaviors, depending on the structure type (zigzag, armchair, or chiral) and the tube diameter. Based on silicon's "inability" to adopt the sp^2 coordination, Seifert et al. [223] argued that the existence of SiNTs is doubtful. Alternatively, these authors proposed that Si-based silicide and SiH nanotubes are theoretically stable and energetically viable, and could thus be considered as sources of silicon nanotubes, particularly in view of the existence of many layered silicides. We explored the possibility of the existence of SiNTs based on semi-empirical calculations and found that SiNTs could in principle be formed with puckered surfaces under appropriate conditions [224]. The strain energy of such structures has recently been described by Barnard et al. [225]. In a more recent work, Zhang et al. [226] obtained a similar tubular structure optimized by DFT calculations. It is obvious from these studies that the calculated structures of SiNTs are sensitive to the method used. Further calculations using the total energy approaches showed that SiNTs can adopt a number of distorted tubular structures, depending on the theory and the initial models adopted [230].

In particular, “gear-like” structures with alternating sp^3 -like and sp^2 -like silicon local configurations are dominant for SiNTs via density-functional tight binding molecular dynamics simulations. The gear-like structures of SiNTs deviate notably from the smooth-walled tubes. However, they are energetically less stable than the “string-bean-like” SiNT structures previously derived from semiempirical molecular orbital calculations [224].

Double-walled silicon nanotubes (DWSiNTs) or called tube-like SiNWs with faceted wall surfaces, as shown in Fig. 58, are also favorable configurations [231]. These tube-like structures have higher energetic favorability than the conventionally adopted cylindrical configurations of single-walled silicon nanotubes (SWSiNTs). The hexagonal (h-) and tetrahedral (t-) like structures of these DWSiNTs are almost energetically equivalent.

The faceted DWSiNTs are energetically more favorable than the SiNW by about 0.078 eV/atom. They still have high formation energies and the tendency to become nanowires at high temperature. These faceted DWSiNTs are expected to be fabricated in experiments as metastable forms of Q1D silicon nanostructures.

It is encouraging that there are a few experimental reports on the synthesis of SiNTs in the past few years [232–237], supporting the predictions described above. The first is the preparation of crystalline SiNTs (designated as cSiNTs), which may be described as a hollow crystalline SiNW [232,233]. While this morphology represents a new silicon nanotubular structure, it is very different from the conventional rolled-up graphite-like sheet structures epitomized by the CNTs. The second is the synthesis of a new type of SiC nanostructure [234]

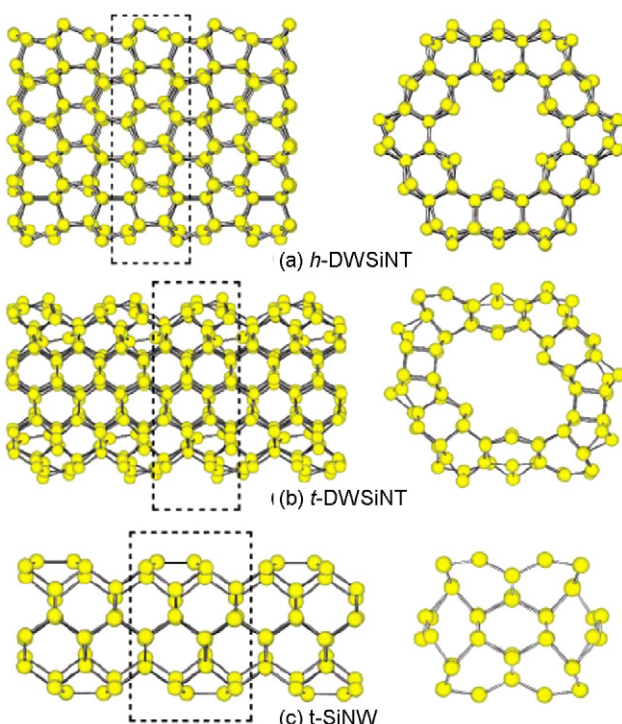


Fig. 58. Equilibrium configurations of SiNTs and a SiNW. Side view (left) and top view (right) of (a) h-DWSiNT, (b) t-DWSiNT, and (c) t-SiNW [231].

which may be described as SiC nanotube (SiCNT). It was prepared by thermal evaporation (disproportionation) of SiO onto multi-walled CNTs (as a sacrificial template). Element mappings under TEM show a multi-walled tubular structure composed of silicon and carbon atoms. While the morphologies of these multi-walled SiCNTs are similar to the conventional rolled-up graphite-like sheet structures of multi-walled CNTs (but with larger interlayer spacings), they are not pure SiNTs. More recently, Tang and coworkers [235,236] synthesized SiNTs from silicon monoxide powder under supercritically hydrothermal conditions with moderate temperature and press. The obtained SiNTs were hollow inner pores and the interplanar spacing of silicon wall layers was 0.31 nm. Moreover, Crescenzi et al. [237] reported the experimental imaging of SiNTs with very thin walls and showed that the armchair SiNTs were semiconducting. It is known that layered silicon systems exist in some silicides. For instance, in alkaline-earth metal silicides [238], the silicon layers, formed by cyclohexane-like rings, are separated by metal ions. It is conceivable that the layered structure of silicon in these systems may roll up to form tubular structures analogous to the “gear-like” configurations.

5.2. Oxide nanowires

5.2.1. Silicon oxide nanowires

Silica is an important material in many technological and scientific areas [239]. In the past decades, considerable progress has been made in growing 1D nanomaterials of silicon dioxide, including nanowires [240–245] and nanotubes [246–255], because of their potential applications in electronics, optics, and nanodevices. However, only a few experimental and theoretical studies have been reported on the atomic and electronic structures of these materials and on their nucleation and growth mechanisms, despite the success in their synthesis with a variety of methods, including laser ablation [240] for nanowires and the porous or solid rod-like template approach [246,247] for nanotubes. As the basic building blocks of these 1D nanomaterials, silicon dioxide nanoparticles and clusters have also attracted a great deal of experimental [256–265] and theoretical [141,266–286] interests. Extensive efforts have been devoted to determining the structures for small $(SiO_2)_n$ in the recent years. For example, Harkless et al. [269] have performed extensive searches to locate possible stable structures of $(SiO_2)_n$ ($n = 1–8$) using molecular dynamics simulations and an empirical pairwise interaction potential. Nayak et al. [270] have carried out calculations for $(SiO_2)_n$ ($n = 1–6$) at the generalized gradient approximation (GGA) level of density functional theory (DFT) using Becke form of the exchange functional and Perdew–Wang expression of the correlation functional. Recently, Flikkema et al. [275,276] reported the lowest-energy structures of $(SiO_2)_n$ with $n = 6–12$ at the B3LYP/6-31G(d) level of theory, based on the results obtained using the Basin Hopping global optimization algorithm [277] and their newly fitted interatomic potential for nanoscale silicon dioxide. The predicted ground state structures for $n = 7–8$ are different from those by Harkless [269]. The revealed structural

motifs could not only enrich the database of silicon dioxide clusters but also provide important structural basis of the nanosized clusters to assemble into 1D nanomaterials.

Among the existing predictions, a structural model of 1D thin silicon dioxide nanowires [287] proposed by us composed of spiro union two-membered-ring (SU-2MR) units. As revealed by density functional calculations, the SU-2MR wire is formed by parallel 2MRs bridged by oxygen atoms and is energetically more favorable, thermally more stable and chemically more reactive at the tip than the edge-sharing two-membered ring molecular chain proposed early. The isodensity surfaces of the HOMO and LUMO states of the SU-2MR chain at $n = 12$ are shown in Fig. 59, respectively. The energy gap is a signature of the chemical reactivity of a system. Compared to the edge-sharing (ES) 2MR chains, the relatively smaller gaps of SU-2MR chains indicate higher chemical reactivities, facilitating the continuous growth of the chains. Hence, the SU-2MR chain may be a more reasonable growth model of 1D silicon dioxide nanowires.

Given the frequent occurrence of three-membered-rings (3MRs) in small- and medium-sized silicon dioxide clusters [276,280,282,286], they can be expected to be assembled also into silicon dioxide nanowires. The formed 3MR-based nanowires would be slightly thicker than those assembled from the spiro union 2MR units [286]. The silicon dioxide cluster, $(\text{SiO}_2)_8$, that was shown to be magic by Flikkema et al. [276] presents a geometrical structure of high symmetry with reactive ends of $\text{Si}=\text{O}$ groups, making it easy to be assembled into larger linearly extended clusters and showing the possibility to act as the building block of 1D silicon dioxide nanowires. The growth mode of a silicon dioxide nanowire based on small silicon dioxide clusters may change at different wire lengths. A linear chain might be assembled from the smallest clusters of rhombic 2MR with $n \leq 5$, while the growth motif changes at $n = 6$ into a more compact form composed of 3MRs. The 3MR containing structures become energetically favorable configurations for even longer silicon dioxide clusters. In particular, the closed molecular ring consisting of 3MRs at $n = 8$ (i.e., $(\text{SiO}_2)_8$) with a high symmetry shows extreme energetic stability and relatively high chemical reactivity and thus is considered to be an important building block to assemble into silicon dioxide nanowires.

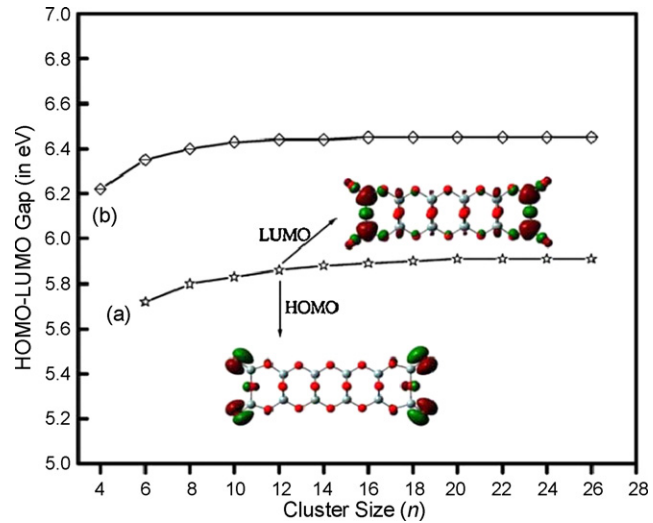


Fig. 59. HOMO–LUMO gaps of the silicon dioxide molecular chains as a function of n for (a) SU-2MR chains and (b) ES-2MR chains. The insets show the isodensity surfaces of the HOMO and LUMO of the SU-2MR chain at $n = 12$ [287].

A new structural type of silicon dioxide clusters appears once the 3MR ring motifs are assembled into larger size [288]. Fig. 60 shows three representative structures of the clusters assembled from this basic unit. These structures contain two, three, and nine units of the $(\text{SiO}_2)_8$ ring, respectively. They possess unique geometrical features: two basic units of $(\text{SiO}_2)_8$ link into a prolate, rhombus-like wire; the adjacent two units are mutually perpendicular to each other. The structure extends in a straight way. The two 2MRs naturally appear between two basic motifs. The geometries of these clusters are not apparently different from the initially assembled structures in DFT molecular dynamics simulations at temperature up to 3000 K with a time step of 1 fs for a total of 1000 steps, indicating their intrinsic structural stabilities.

Fig. 61 shows the binding energies (E_{bs}) of the one made of $(\text{SiO}_2)_8$ rings (curve (a)), compared with those of silicon dioxide nanowires of similar diameters in the literature, including the thinnest 2MR molecular chain [283] (curve (b)), the spiro union 2MR molecular chain [287] (curve (c)), the double six-ring nanowire [289] (curve (d)), and the double four-ring nanowire built from the ground-state building unit of

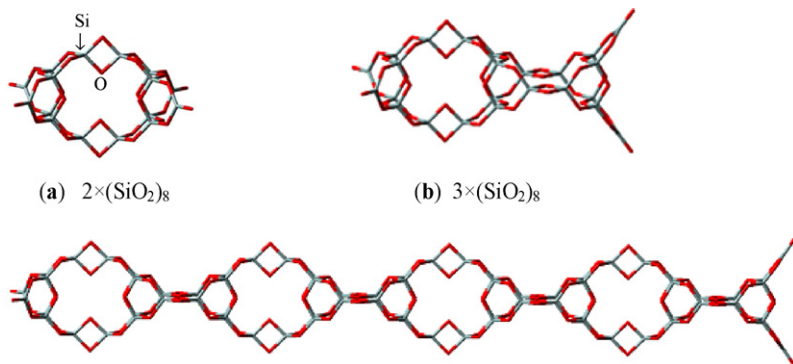


Fig. 60. Stable geometries of the silicon dioxide clusters assembled from the most stable 3MR-ring motif of $(\text{SiO}_2)_8$. The panels (a), (b) and (c) contain two, three, and nine $(\text{SiO}_2)_8$ units, respectively [288].

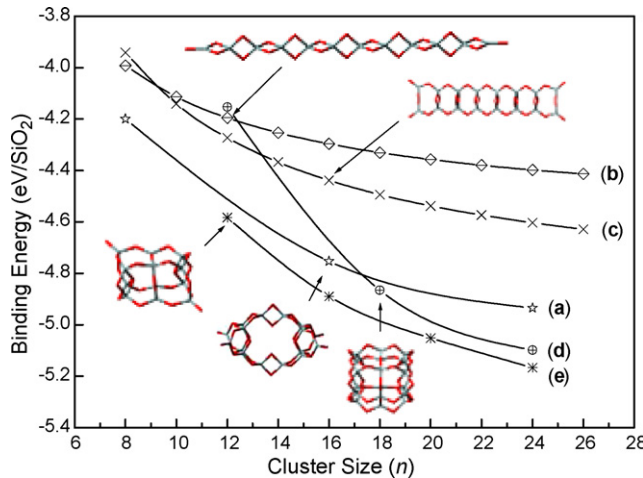


Fig. 61. The monomer binding energy (E_b) of the silicon dioxide clusters calculated at the B3LYP/6-31G(d) level as a function of the cluster size, n for (a) the structures made of $(\text{SiO}_2)_8$ rings, (b) the 2MR molecular chains [283], (c) the spiro union 2MR molecular chains [287], (d) the double six-ring wires, and (e) the double four-ring wires. The representative structures (one from each type) of the silicon dioxide clusters are included as the insets of the figure [288].

$(\text{SiO}_2)_{12}$ [276] (curve (e)). Clearly, the ones made of $(\text{SiO}_2)_8$ rings are much more stable in E_b than the 2MR chain and spiro union 2MR chain. For example, the silicon dioxide rods for $n = 16$ and $n = 24$ are respectively more stable by 0.314 and 0.349 eV than the corresponding spiro union 2MR molecular chains, by 0.424 and 0.456 eV than the corresponding edge-shared 2MR molecular rings, and by 0.456 and 0.537 eV than the corresponding edge-shared 2MR molecular chains. Compared with the double six-ring model and the double four-ring model, however, the 3MR-based silicon dioxide nanowire model is energetically less favorable. This can be attributed to the relatively larger strains in 3MRs than in 4- and 6MRs. Experimentally, silicon dioxide nanowires were synthesized via many methods, such as excimer laser ablation, carbothermal reduction, and catalyzed thermal decomposition. Therefore, the silicon dioxide nanowires synthesized at given conditions are expected to possess characteristic microstructures. In other words, the structures of synthetic silicon dioxide nanowires depend on the given condition. It should be noted that ground-state structures are not necessarily formed, but metastable structures in real 1D nanomaterials [285], as confirmed by recent experiments [290]. Based on these facts, the 3MR-based silicon dioxide model as one of the reasonable structural models of 1D silicon dioxide nanowires, even though it is not energetically the most favorable structure. The results provide valuable additional information for understanding the nucleation and growth mechanisms of the silicon dioxide nanowires.

5.2.2. Silicon dioxide tube-like nanowires

Silicon dioxide nanotubes have a hydrophilic nature, an easy formation of colloidal suspension, and ready access of both inner and outer walls for surface functionalization. As such they have wide applications in biocatalysis, bioseparation [291,292], nanoscale electronic devices [293], and protection of environmentally sensitive species [294,295]. So far, various methods

[296–303] have been used to synthesize silicon dioxide nanotubes. The as-prepared silicon dioxide nanotubes always have an amorphous wall with a thickness of several tens of nanometers. However, as the thickness is reduced to a few angstroms (ultra-thin), the ratio of surface-to-bulk atoms increases enormously. High surface energy would force the atoms on the tube wall to rearrange so as to reduce the number of dangling bonds, giving rise to a novel configuration. It would thus be interesting to reveal (i) if this ultra-thin silicon dioxide nanotube (USiO₂NT) has a well-ordered configuration and (ii) what fascinating properties, such as size-dependent electronic and elastic properties, can be induced in this novel structure by size effects.

A fully coordinated silicon dioxide cluster based on the hybridization of 2-, 4-, and 6MRs has been utilized as a model system for investigating the reaction of water with silicon dioxide nanotubes [304], as well as for modeling elongated silicon dioxide nanocages [305]. Built on these work, an exploration of the growth mechanism of the silicon dioxide nanotubes have been performed by us by studying a fully coordinated, well-ordered, and chirality-characterized model for USiO₂NTs [306], which are expected to be of advantages compared with the fibrous silicon dioxide [307].

The dependence of E_s of $(n,0)$ USiO₂NTs referencing to α -quartz versus n is plotted in Fig. 62. The open circles correspond to the CI configurations (as shown in Fig. 63(a)–(e)). The variation of E_s is not monotonic but with two local minima, $n = 5$ and 9, for n ranging from 3 to 16. These tubes have an E_s of 0.60–0.80 eV/SiO₂, which is much lower than that of the fully coordinated silicon dioxide sheet and silicon dioxide fibre, but higher than that of SWNTs with respect to graphite sheet, i.e. ~ 0.16 eV/atom for (5,5) SWNT [308]. The existence of magic configurations in USiO₂NTs is quite different from SWNTs, where the E_s decreases monotonously with increasing tube diameter and saturates at the value of

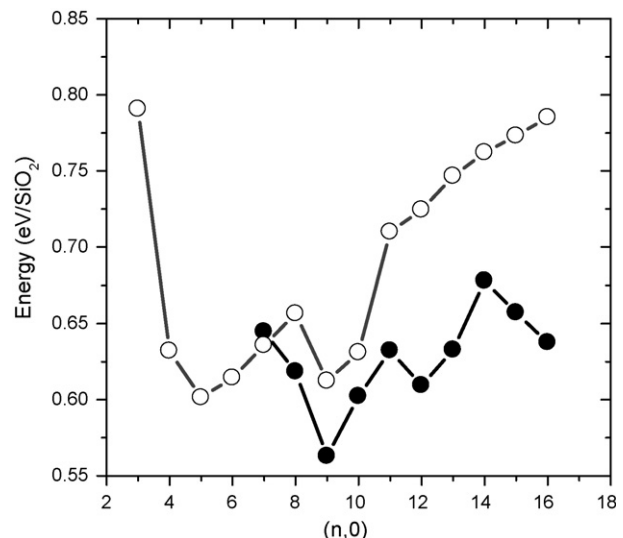


Fig. 62. The strain energy of USiO₂NTs relative to α -quartz for different tubes. Open circles represent the tubes without wall reconstruction, while solid circles denote the reconstructed USiO₂NTs [306].

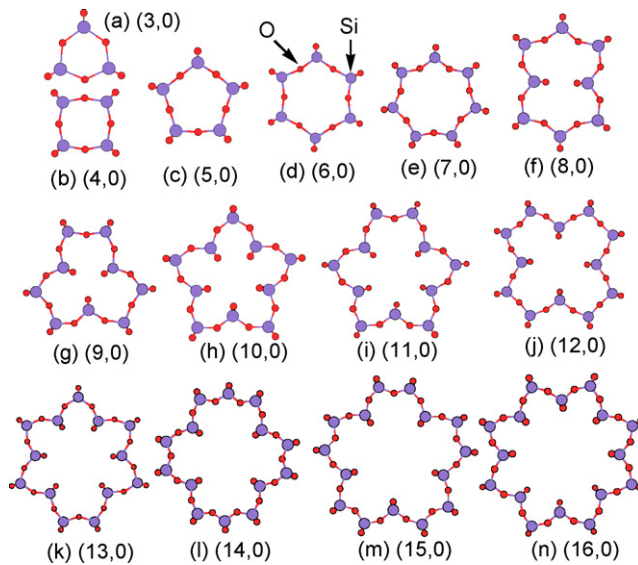


Fig. 63. Cross section views of different USiO_2NTs which are energetically the most favorable among their isomers [306].

graphite sheet [308]. The higher E_s involved in the fully coordinated silicon dioxide sheet compared to that of USiO_2NTs indicates that such a planar sheet is energetically unstable. A silicon dioxide sheet with finite width ($\sim 14 \text{ \AA}$) and infinite long (periodic) heated from 300 to 1000 K and kept at 1000 K for 5 ps with the time step of 1 fs is curved around an axis and tends to form USiO_2NTs . This suggests a promising way to synthesize USiO_2NTs , providing that the fully coordinated silicon dioxide sheet can be realized which remains challenging to experimentalists. Recently, a well-ordered ultra-thin silicon dioxide film with only a few angstroms of thickness has already been grown on Mo substrate [309–311]. The 2D network of this silicon dioxide film [309–311] is slightly different from the isolated silicon dioxide sheet here, mainly due to the Mo–O bond formation. It is reasonable to deduce that once the substrate is removed, e.g. by a selective etching procedure, a structural reorganization induced by the formation of additional O–Si bonds would probably result in a fully coordinated silicon dioxide sheet.

By pushing some Si and O atoms toward the tube axis and changing the orientation of the relevant Si–O bonds, several isomers with buckling surfaces are obtained after relaxation. The most favorable configurations (Fig. 63(f)–(n)) are collected among these isomers by comparing their total energies. These buckled silicon dioxide tubes are energetically more favorable than that with CI configuration as $n > 7$ (denoted by the solid circles in Fig. 62). The USiO_2NTs of the large radii cannot simply be modeled by rolling up the silicon dioxide sheet, and the reconstruction in the tube wall should be taken into account, which would definitely affect the surface dipoles and related properties. It is interesting that local energy minima appear at three magic configurations corresponding to $n = 5, 9$, and 12, among which (9,0) USiO_2NT is energetically the most favorable. The energetic stability of these magic configurations can be attributed to their small deviation of O–Si–O bond angle from that in α -quartz, which allows them to further release the strain

energy. The existence of magic configurations is important for the synthesis and detection of USiO_2NTs in experiments.

The elastic properties of magic USiO_2NTs under tensile strain along the axial direction provide the variation of stress σ_{zz} versus strain under tensile ε_{zz} loaded along an axial direction of (9,0) USiO_2NT . This tube follows the classical elasticity theory as $\varepsilon_{zz} < 0.1$. The Young's modulus of these tubes is almost of the same order of magnitude as that of carbon nanotubes, $\sim 1.0 \text{ TPa}$ [312], and several times greater than that of quartz microfibres of $\sim 70 \text{ GPa}$ [313]. The higher stiffness of USiO_2NTs could be attributed to their unique well-ordered structure compared to amorphous quartz microfibres. The band gap decreases linearly with increasing stress (or strain). The pressure coefficient of (9,0) tube is evaluated to be -55 meV/GPa . In view of the well-known piezoelectric properties of quartz, the USiO_2NTs are expected to be useful in building novel nanoscale electronic devices such as nano-oscillators.

5.2.3. Zinc oxide tube-like nanowires

The nanotubes synthesized so far include boron nitride nanotubes [314] and silicon carbide nanotubes [234,315]. In contrast, few works on ZnO nanotubes have been reported, as the tubular nanostructure is generally formed from a material which could also exist in a layered form. As such, it seems hard to obtain the tubular structure of the ZnO material as no layered ZnO exists. It is widely acknowledged that the hollow 1D ZnO structure could provide more prominent advantages than other 1D ZnO materials. The formation of tubes is expected to facilitate the confinement effect in 1D structure, and a large surface area/volume ratio in tubular structure could provide an effective way to store hydrogen. Several groups have already synthesized hexagonally shaped ZnO nanotubes [316–318]. However, single-walled ZnO nanotubes with round walls have not been synthesized till now. Recently, double-walled ZnO nanotubes with a round wall shape have been synthesized [319], and Tu et al. [320] indicated a possibility to synthesize single walled ZnO nanotubes. Similar to carbon nanotubes whose physical properties are correlated with their diverse phases, the tubular structure of ZnO material is expected to offer electronic and optical properties different from those of the bulk and other low dimensional structures. Erkoç et al. [321] have investigated the structural and electronic properties of (4,4) armchair and (4,0) zigzag single-walled ZnO nanotubes by performing semiempirical molecular orbital self-consistent field calculations at the level of the Austin model 1 (AM1) method within the restricted Hartree–Fock (RHF) formulation. They found armchair ZnO nanotubes seemed to be conductors and zigzag ZnO nanotubes semiconductors. Our recent first-principles calculations on the structure, stability and electronic properties of single-walled ZnO nanotubes provide reliable knowledge of this important nanomaterial [322]. It was found that the strain energy required for rolling a ZnO graphitic sheet into a tube is lower than those for BN and GaN nanotubes. The strain energy of ZnO nanotubes follows a classical $1/D^2$ strain law. All the ZnO nanotubes are found to be direct band semiconductors with band gaps decreasing from 2.005 to 1.631 eV with the increase of diameter, while the shapes of the band edges remain unaltered.

The ZnO nanotubes were distorted tubular structures in which zinc and oxygen atoms were shifted inward and outward to the axis, forming homocentric cylinders with different diameters (D_{Zn} and D_{O}), respectively. The radical buckling is 0.120 Å for (5,5) nanotubes and 0.117 Å for (9,0) nanotubes. The diameter of the oxygen cylinder is larger than that of zinc. Their difference ($D_{\text{O}} - D_{\text{Zn}}$) decreases with the increase in diameter. The larger the diameter, the smaller the buckling is.

The Zn–O bond length decreases with the increase of nanotube diameter in all the considered cases and is noticeably shorter than the corresponding value of 2.01 Å of ZnO bulk due to the buckle of the Zn–O atoms. The calculated Zn–O bond lengths vary from 1.892 to 1.957 Å, which are larger than the graphitic Zn–O bond length 1.890 Å and similar to those of BN and GaN nanotubes [323,324]. Due to the relaxation of atoms, the lattice constant c of the zigzag ZnO nanotube is increased with the diameter increase while that of the armchair ZnO nanotubes decreases with the diameter increase.

The binding energy of wurtzite ZnO is –3.678 eV/atom and the binding energy of the graphitic sheet is –3.440 eV/atom. The energy difference between graphitic and wurtzite ZnO (0.238 eV/atom) is lower than that between graphitic and zinc-blende bulk of GaN (0.36 eV/atom) [323], indicating that the graphitic ZnO structure is relatively stable, although no layered ZnO exists in reality. The graphitic ZnO is energetically less stable and ZnO prefers forming sp^3 bonds rather than sp^2 bonds. The strain energy for ZnO nanotubes is inversely proportional to the square of the diameter, suggesting that the ZnO nanotubes follow a classical elasticity law [325]. The strain energy decreases from 0.23 to 0.01 eV/atom with increasing diameter of the ZnO nanotube, similar to the case of the BN nanotube [326] and GaN nanotube [323]. The formation energies are relatively insensitive to the chirality of the nanotubes, similar to that of the GaN nanotube [323] but in big contrast with the fact that armchair carbon nanotubes are more stable than zigzag nanotubes [327]. The fact that the strain energies of ZnO nanotubes are comparable to those of carbon nanotubes [327] and BN nanotubes [326] indicates a possibility for the synthesis of ZnO nanotubes. However, the stability of a tubular structure does not only depend on the strain energy, but more importantly depends on the stability of the graphitic phase, which, however, is poor for ZnO.

The band structure of bulk wurtzite ZnO shows a direct band gap of 0.75 eV. The graphitic ZnO has a direct band gap of 1.68 eV at the Γ point. For the graphitic ZnO, the highest occupied state is mainly composed of O 2p states, while the lowest unoccupied state is mostly Zn 4s states. Further, all ZnO nanotubes are semiconducting with a direct band gap at the Γ point. Although the DFT usually underestimates the band gap, the trend of the band gaps of ZnO nanotubes is expected to be correct. The band gaps of the ZnO nanotubes range from 1.631 to 2.005 eV. These band gaps are larger than that of the ZnO bulk, indicating strong quantum confinement effects. The band gap decreases with increasing nanotube diameter. All the armchair and zigzag ZnO nanotubes are direct band gap semiconductors, different from GaN nanotubes [323].

6. Concluding remarks

In the past 10 years, the novel properties of 1D nanomaterials have been extensively studied. In addition to the opportunity to describe the new physics demonstrated by 1D nanostructures, much effort has been devoted to fabricating high-quality semiconductor and oxide nanoscale wires based on the bottom-up, self-assembly process by employing different techniques. The classical VLS process which was developed in the 1960s is still applicable to the growth of many nanoscale wires produced today. Various new techniques have been developed by which high-quality ultra-thin nanowire structures have been fabricated, such as oxide-assisted CVD, chemical solution techniques and metal-catalyzed MBE and CBE. In particular, the MBE and CBE techniques provide an ideal clean growth environment and allow high levels of control over atomic structures, chemical composition, defects, doping states, junctions, and so forth. These techniques are promising to fabricate desired 1D nanomaterials with tailored atomic structures and to integrate functional nanostructures into devices. 1D nanostructures grown by these technologies have been observed to exhibit interesting and sometimes unusual growth phenomena. With the extensive studies throughout the years, our understanding of the basic process of 1D nanostructure formation (nucleation, growth, defects, junctions and interfaces) has been greatly enhanced. For 1D semiconductor and oxide nanomaterials to have wide practical applications, however, many areas require further development. In particular, the fabrication of desired functional 1D nanostructures with fully controlled interface structures or junction and chemical composition, and their assembly into functional devices are still major challenges for nanotechnologists. The solution-based technique has been demonstrated as a promising alternative approach for mass production of metal, semiconductor and oxide nanomaterials with excellent controls of the shape and composition with high reproducibility. Its major limit is that the growth mechanisms are poorly known and most structural director agents are chosen by the way of trial and error. Many questions about the formation of nanowire structures via highly anisotropic growth of nanocrystals in semiconductor and metal oxide materials, their reactivity and stability still need to be further addressed. Most 1D nanostructures are formed under non-equilibrium state and controlled by kinetic processes. Theoretical works have helped our understanding of the mechanism of some growth and provided certain prediction on novel structures. Much more efforts are still needed for more complicated systems involving new structural morphologies and new processes. In particular, the highly anisotropic growth of nanocrystals, quantitative explorations and predictions of new properties and their energetic, dynamic and kinetic behaviors need further development.

Acknowledgements

The authors are truly grateful for financial support from the Research Grants Council of Hong Kong (Project Nos.

N_HKUST615/06 and CityU3/04C). RQZ thanks Ms. W.J. Fan for assistance in some literature material collections.

References

- [1] H. Sakaki, Jpn. J. Appl. Phys. 19 (1980) L735.
- [2] A.T. Tilke, F.C. Simmel, H. Lorenz, R.H. Blick, J.P. Kotthaus, Phys. Rev. B 68 (2003) 075311.
- [3] A.S. Eddlestein, R.C. Cammarata, Nanomaterials: Synthesis, Properties and Applications, Taylor & Francis, 1996.
- [4] M.A. Reed, J.N. Randall, R.J. Aggarwal, R.J. Matyi, T.M. Moore, A.E. Wetsel, Phys. Rev. Lett. 60 (1988) 535.
- [5] R.S. Wagner, W.C. Ellis, Appl. Phys. Lett. 4 (1964) 89.
- [6] (a) E.I. Givargizov, Highly Anisotropic Crystals, Springer, New York, 1987;
 (b) E.I. Givargizov, J. Cryst. Growth 31 (1975) 20.
- [7] A.M. Morales, C.M. Lieber, Science 279 (1998) 208.
- [8] D.P. Yu, Z.G. Bai, Y. Ding, Q.L. Hang, H.Z. Zhang, J.J. Wang, Y.H. Zou, W. Qian, G.C. Xiong, H.T. Zhou, S.Q. Feng, Appl. Phys. Lett. 72 (1998) 3458.
- [9] P. Yang, MRS Bull. 30 (2005) 85.
- [10] Y.F. Zhang, Y.H. Zhang, N. Wang, D.P. Yu, C.S. Lee, I. Bello, S.T. Lee, Appl. Phys. Lett. 72 (1998) 1835.
- [11] N. Wang, Y.F. Zhang, Y.H. Tang, C.S. Lee, S.T. Lee, Appl. Phys. Lett. 73 (1998) 3902.
- [12] Z.W. Pen, Z.R. Dai, Z.L. Wang, Science 291 (2001) 1947.
- [13] Z.H. Wu, X.Y. Mei, D. Kim, M. Blumin, H.E. Ruda, Appl. Phys. Lett. 81 (2002) 5177.
- [14] Y.F. Chan, X.F. Duan, S.K. Chan, I.K. Sou, X.X. Zhang, N. Wang, Appl. Phys. Lett. 83 (2003) 2665.
- [15] L. Schubert, P. Werner, N.D. Zakharov, G. Gerth, F.M. Kolb, L. Long, U. Gösele, Appl. Phys. Lett. 84 (2004) 4968.
- [16] M.T. Björk, B.J. Ohlsson, T. Sass, A.I. Persson, C. Thelander, M.H. Magnusson, K. Deppert, L.R. Wallenberg, L. Samuelson, Appl. Phys. Lett. 80 (2002) 1058.
- [17] A.P. Levitt, Whisker Technology, John Wiley & Sons Inc., 1971.
- [18] G.A. Bootsma, H.J. Gassen, J. Cryst. Growth 10 (1971) 223.
- [19] H. Adhikari, A.F. Marshall, C.E.D. Chidsey, P.C. McIntyre, Nano Lett. 6 (2006) 318.
- [20] J. Westwater, D.P. Gosai, S. Tomiya, S. Usui, H. Ruda, J. Vac. Sci. Technol. B 15 (1997) 554.
- [21] Y. Wu, P. Yang, Chem. Mater. 12 (2000) 605.
- [22] Y.W. Wang, V. Schmidt, S. SenZ, U. Gösele, Nat. Nanotechnol. 1 (2006) 186.
- [23] Y.J. Zhang, Q. Zhang, N.L. Wang, Y.J. Yan, H.H. Zhou, J. Zhu, J. Cryst. Growth 226 (2001) 185.
- [24] M. Lopez-Lopez, A. Guillen-Cervantes, Z. Rivera-Alearez, I. Hernandez-Calderon, J. Cryst. Growth 193 (1998) 528.
- [25] Y. Wang, G. Meng, L. Zhang, C. Liang, J. Zhang, Chem. Mater. 14 (2002) 1773.
- [26] Y. Wang, L. Zhang, C. Liang, G. Wang, X. Peng, Chem. Phys. Lett. 357 (2002) 314.
- [27] S.T. Lee, N. Wang, Y.F. Zhang, Y.H. Tang, MRS Bull. 24 (1999) 36.
- [28] K.A. Dick, K. Deppert, T. Martensson, B. Mandl, L. Samuelson, W. Seifert, Nano Lett. 5 (2005) 761.
- [29] M. Yazawa, M. Koguchi, A. Muto, K. Hiruma, Adv. Mater. 5 (1993) 577.
- [30] K. Hiruma, M. Yazawa, T. Katsuyama, K. Ogawa, K. Haraguchi, M. Koguchi, H. Kakibayashi, J. Appl. Phys. 77 (1995) 447.
- [31] T. Shimada, K. Hiruma, M. Shirai, M. Yazawa, K. Haraguchi, T. Sato, M. Matsui, T. Katsuyama, Superlattice Microstruct. 24 (1998) 453.
- [32] M.S. Gudiksen, C.M. Lieber, J. Am. Chem. Soc. 122 (2000) 8801.
- [33] X. Duan, C.M. Lieber, Adv. Mater. 12 (2000) 298.
- [34] C.C. Chen, C.C. Yeh, Adv. Mater. 12 (2000) 738.
- [35] C.C. Chen, C.C. Yeh, C.H. Chen, M.Y. Yu, H.L. Liu, J.J. Wu, K.H. Chen, L.C. Chen, J.Y. Peng, Y.F. Chen, J. Am. Chem. Soc. 123 (2001) 2791.
- [36] J. Zhang, X.S. Peng, X.F. Wang, Y.W. Wang, L.D. Zhang, Chem. Phys. Lett. 345 (2001) 372.
- [37] Y. Wu, H. Yan, M. Huang, B. Messer, H.J. Song, P. Yang, Chem. Eur. J. 8 (2002) 1260.
- [38] M. He, P. Zhou, S.N. Mohammad, G.L. Harris, J.B. Halpern, R. Jacobs, W.L. Sarney, L.S. Riba, J. Cryst. Growth 231 (2001) 357.
- [39] W.S. Shi, Y.F. Zhang, N. Wang, C.S. Lee, S.T. Lee, J. Vac. Sci. Technol. B 19 (2001) 1115.
- [40] T. Kuykendall, P. Pauzauskie, S. Lee, Y. Zhang, J. Goldberger, P. Yang, Nano Lett. 3 (2003) 1063.
- [41] Z. Zhou, F. Qian, D. Wang, C.M. Lieber, Nano Lett. 3 (2003) 343.
- [42] P. Yang, C.M. Lieber, Science 271 (1996) 1836.
- [43] M.H. Huang, Y. Wu, H. Feick, N. Tran, E. Weber, P. Yang, Adv. Mater. 13 (2001) 113.
- [44] X.C. Wu, W.H. Song, B. Zhao, Y.P. Sun, J.J. Du, Chem. Phys. Lett. 349 (2001) 210.
- [45] X.S. Peng, G.W. Meng, X.F. Wang, Y.W. Wang, J. Zhang, X. Liu, L.D. Zhang, Chem. Mater. 14 (2002) 4490.
- [46] X. Liu, C. Li, S. Han, J. Han, C. Zhou, Appl. Phys. Lett. 82 (2003) 1950.
- [47] P. Nguyen, H.T. Ng, J. Kong, A.M. Cassel, R. Quinn, J. Li, J. Han, M. McNeil, M. Meyyappan, Nano Lett. 3 (2003) 925.
- [48] H.Y. Kim, J. Park, H. Yang, Chem. Phys. Lett. 371 (2003) 269.
- [49] R. Ma, Y. Bando, Chem. Mater. 14 (2002) 4403.
- [50] H.Y. Kim, J. Park, H. Yang, Chem. Commun. (2003) 256.
- [51] J.M. Howe, H. Saka, MRS Bull. 29 (2004) 951.
- [52] H. Wang, G.S. Fischman, J. Appl. Phys. 76 (1994) 1557.
- [53] L. Schubert, P. Werner, N.D. Zakharov, Appl. Phys. Lett. 84 (2004) 4968.
- [54] S. Kodambaka, J. Tersoff, M.C. Reute, F.M. Ross, Science 316 (2007) 729.
- [55] L. Holland (Ed.), Vacuum Deposition of Thin Films, Chapman & Hall Ltd., London, 1966.
- [56] W. Shi, Y. Zheng, H. Peng, N. Wang, C.S. Lee, S.T. Lee, J. Am. Ceram. Soc. 83 (2000) 3228.
- [57] E. Stern, G. Cheng, S. Guthrie, D. Turner-Evans, E. Broomfield, B. Lei, C. Li, D. Zhang, C. Zhou, M.A. Reed, Nanotechnology 17 (2006) S246.
- [58] T.Q. Jia, H.X. Chen, M. Huang, X.J. Wu, F.L. Zhao, M. Baba, M. Suzuki, K. Kuroda, J.R. Qiu, R.X. Li, Z.Z. Xu, Appl. Phys. Lett. 89 (2006) 101116.
- [59] Y.F. Zhang, Y.H. Tang, H.Y. Peng, N. Wang, C.S. Lee, I. Bello, S.T. Lee, Appl. Phys. Lett. 75 (1999) 1842.
- [60] D.P. Yu, C.S. Lee, I. Bello, X.S. Sun, Y.H. Tang, G.W. Zhou, Z.G. Bai, Z. Zhang, S.Q. Feng, Solid State Commun. 105 (1998) 403.
- [61] E.A. Stach, P.J. Pauzauskie, T. Kuykendall, J. Goldberger, R. He, P. Yang, Nano Lett. 3 (2003) 867.
- [62] Z.L. Wang, X.Y. Kong, J.M. Zou, Phys. Rev. Lett. 91 (2003) 185502.
- [63] Y.F. Zhang, Y.H. Tang, X.F. Duan, Y. Zhang, C.S. Lee, N. Wang, I. Bello, S.T. Lee, Chem. Phys. Lett. 323 (2000) 180.
- [64] H. Yan, R. He, J. Pham, P. Yang, Adv. Mater. 15 (2003) 402.
- [65] H. Yan, R. He, J. Johnson, M. Law, R.J. Saykally, P. Yang, J. Am. Chem. Soc. 125 (2003) 4728.
- [66] Z.R. Dai, Z.W. Pen, Z.L. Wang, Adv. Funct. Mater. 13 (2003) 9.
- [67] B.D. Yao, Y.F. Chan, N. Wang, Appl. Phys. Lett. 81 (2002) 757.
- [68] N. Wang, Y.H. Tang, Y.F. Zhang, C.S. Lee, S.T. Lee, Phys. Rev. B 58 (1998) 16024.
- [69] N. Wang, Y.H. Tang, Y.F. Zhang, C.S. Lee, S.T. Lee, Chem. Phys. Lett. 299 (1999) 237.
- [70] Y.F. Zhang, Y.H. Tang, N. Wang, C.S. Lee, I. Bello, S.T. Lee, Phys. Rev. B 61 (2000) 4518.
- [71] W.S. Shi, Y.F. Zheng, N. Wang, C.S. Lee, S.T. Lee, Adv. Mater. 13 (2001) 591.
- [72] S.C. Lyu, Y. Zhang, H. Ruh, H.J. Lee, C.J. Lee, Chem. Phys. Lett. 367 (2003) 717.
- [73] H.Y. Peng, X.T. Zhou, N. Wang, Y.F. Zheng, L.S. Liao, W.S. Shi, C.S. Lee, S.T. Lee, Chem. Phys. Lett. 327 (2000) 263.
- [74] N. Wang, B.D. Yao, Y.F. Chan, X.Y. Zhang, Nano Lett. 3 (2003) 475.
- [75] G. Hass, J. Am. Ceram. Soc. 33 (1950) 353.
- [76] C.J. Murphy, T.K. San, A.M. Gole, C.J. Orendorff, J.X. Gao, L. Gou, S.E. Hunyadi, T. Li, J. Phys. Chem. B 109 (2005) 13857.
- [77] Y.W. Jun, J.S. Choi, J. Cheon, Angew. Chem. Int. Ed. 45 (2006) 3414.

- [78] J.D. Holmes, K.P. Johnston, R.C. Doty, B.A. Korgel, *Science* 287 (2000) 1471.
- [79] T. Hanrath, B.A. Korgel, *J. Am. Chem. Soc.* 124 (2002) 1424.
- [80] T.J. Trentler, K.M. Hickman, S.C. Goel, A.M. Viano, P.C. Gibbons, W.E. Buhro, *Science* 270 (1995) 1791.
- [81] S.D. Dingman, N.P. Rath, P.D. Markowitz, P.C. Gibbons, W.E. Buhro, *Angew. Chem.* 112 (1995) 1530.
- [82] T.J. Trentler, S.C. Goel, K.M. Hickman, M.Y. Chiang, A.M. Geatty, P.C. Gibbons, W.E. Buhro, *J. Am. Chem. Soc.* 119 (1997) 2172.
- [83] H. Yu, W.E. Buhro, *Adv. Mater.* 15 (2003) 416.
- [84] T. Hanrath, B.A. Korgel, *Adv. Mater.* 15 (2003) 437.
- [85] S.P. Ahrenkiel, O.I. Micic, A. Miedaner, C.J. Curtis, J.M. Nedeljkovic, A.J. Nozik, *Nano Lett.* 3 (2003) 833.
- [86] X. Lu, T. Hanrath, K.P. Johnston, B.A. Korgel, *Nano Lett.* 3 (2003) 93.
- [87] F.M. Davidson III, A.D. Schrieker, R.J. Wiacek, B.A. Korgel, *Adv. Mater.* 16 (2004) 646.
- [88] H.Y. Tuan, D.C. Lee, T. Hanrath, B.A. Korgel, *Nano Lett.* 5 (2005) 681.
- [89] R.L. Penn, J.F. Banfield, *Geochim. Cosmochim. Acta* 63 (1999) 1549.
- [90] J.D.H. Donnay, D. Harker, *Am. Mineral.* 22 (1937) 446.
- [91] Z.Y. Tang, N.A. Kotov, M. Giersig, *Science* 297 (2002) 237.
- [92] K.S. Cho, D.V. Talapin, W. Gaschler, C.B. Murray, *J. Am. Chem. Soc.* 127 (2005) 7140.
- [93] J.H. Yu, J. Joo, H.M. Park, S.I. Baik, Y.W. Kim, S.C. Kim, T. Hyeon, *J. Am. Chem. Soc.* 127 (2005) 5662.
- [94] C. Pacholski, A. Kornowski, H. Weller, *Angew. Chem. Int. Ed.* 41 (2002) 1188.
- [95] G. Che, B.B. Lakshmi, E.R. Fisher, C.R. Martin, *Nature* 393 (1998) 346.
- [96] K.K. Lew, C. Reuther, A.H. Carim, J.M. Redwing, B.R. Martin, *J. Vac. Sci. Technol. B* 20 (2002) 389.
- [97] K.K. Lew, J.M. Redwing, *J. Cryst. Growth* 254 (2003) 14.
- [98] E.C. Greyson, Y. Babayan, T.W. Odom, *Adv. Mater.* 16 (2004) 1348.
- [99] G. Sauer, G. Brehm, S. Schneider, K. Nielsch, R.B. Wehrspohn, J. Choi, H. Hofmeister, U. Gosele, *J. Appl. Phys.* 91 (2002) 3243.
- [100] C. Schonenberger, B.M.I. vanderZande, L.G.J. Fokkink, M. Henny, C. Schmid, M. Kruger, A. Bachtold, R. Huber, H. Birk, U. Staufer, *J. Phys. Chem. B* 101 (1997) 5497.
- [101] B. Gates, B. Mayers, B. Cattle, Y. Xia, *Adv. Funct. Mater.* 12 (2002) 219.
- [102] X.Y. Zhang, G.H. Wen, Y.F. Chan, R.K. Zheng, X.X. Zhang, N. Wang, *Appl. Phys. Lett.* 83 (2003) 3341.
- [103] J.Y. Miao, Y. Cai, Y.F. Chan, P. Sheng, N. Wang, *J. Phys. Chem. B* 110 (2006) 2080.
- [104] Y. Sun, B. Gates, B. Mayers, Y. Xia, *Nano Lett.* 2 (2002) 165.
- [105] Y. Sun, Y. Yin, B.T. Mayers, T. Herricks, Y. Xia, *Chem. Mater.* 14 (2002) 4736.
- [106] B.D. Busbee, S.O. Obare, C.J. Murphy, *Adv. Mater.* 15 (2003) 414.
- [107] Y.G. Sun, B. Mayers, T. Herricks, Y.N. Xia, *Nano Lett.* 3 (2003) 955.
- [108] C.J. Murphy, N.R. Jana, *Adv. Mater.* 14 (2002) 80.
- [109] B.H. Hong, S.C. Bae, C.W. Lee, S. Jeong, K.S. Kim, *Science* 294 (2001) 348.
- [110] L. Vayssieres, *Adv. Mater.* 15 (2003) 464.
- [111] L. Vayssieres, K. Keis, S.F. Lindquist, A. Hagfeldt, *J. Phys. Chem. B* 105 (2001) 3350.
- [112] L.E. Greene, M. Law, J. Goldberger, F. Kim, J.C. Johnson, Y.F. Zhang, R.J. Saykally, P.D. Yang, *Angew. Chem. Int. Ed.* 42 (2003) 3031.
- [113] Y.L. Wang, X.C. Jiang, Y.N. Xia, *J. Am. Chem. Soc.* 125 (2003) 16176.
- [114] C. Cheng, K.F. Yu, Y. Cai, K.K. Fung, N. Wang, *J. Phys. Chem. C* 111 (2007) 16712.
- [115] B. Cheng, T.S. Edward, *Chem. Commun.* (2004) 986.
- [116] D.S. Xu, X.S. Shi, G.L. Guo, L.L. Gui, Y.Q. Tang, *J. Phys. Chem. B* 104 (2002) 5061.
- [117] Z.A. Peng, X.G. Peng, *J. Am. Chem. Soc.* 124 (2002) 3343.
- [118] R.S. Wagner, W.C. Ellis, *Trans. Met. Soc.* 233 (1965) 1053.
- [119] J.P. Borel, *Surf. Sci.* 106 (1981) 1.
- [120] V. Schmidt, S. Senz, U. Gosele, *Appl. Phys. A* 80 (2005) 445.
- [121] N. Li, T.Y. Tan, U. Gosele, *Appl. Phys. A* 86 (2007) 433.
- [122] J.S. Rowlinson, B. Windom, *Molecular Theory of Capillarity*, Dover, 2003.
- [123] T.Y. Tan, N. Li, U. Gosele, *Appl. Phys. Lett.* 83 (2003) 1199.
- [124] A.A. Chernov, H. Müller-Krumbhaar, *Modern Theory of Crystal Growth*, Springer, New York, 1983.
- [125] E.I. Givargizov, A.A. Chernov, *Sov. Phys. Crystallogr.* 18 (1973) 89.
- [126] G. Neumann, G.M. Neumann, *Surface Self-diffusion of Metals*, Diffusion Monograph Series, vol. 1, Diffusion Information Center, 1972, p. 105.
- [127] Y. Cai, Characterization of ultrathin II–VI semiconductor nanowires by transmission electron microscopy, PhD Dissertation, Physics Department, the Hong Kong University of Science and Technology, Hong Kong, September 2007.
- [128] S.K. Chan, MBE-VLS grown ZnSe and ZnS nanowires, PhD Dissertation, Physics Department, the Hong Kong University of Science and Technology, Hong Kong, August 2007.
- [129] (a) V. Schmidt, S. Senz, U. Gosele, *Phys. Rev. B* 75 (2007) 45335; (b) V. Schmidt, S. Senz, U. Gosele, *Phys. Rev. Lett.* 75 (2007) 45335.
- [130] V.G. Dubrovskii, N.V. Sibirev, *J. Cryst. Growth* 304 (2007) 504.
- [131] Y. Cai, S.K. Chan, I.K. Sou, Y.F. Chan, D.S. Su, N. Wang, *Adv. Mater.* 18 (2006) 109.
- [132] W.K. Burton, N. Cabrera, F.C. Frank, *Nature* 163 (1949) 398.
- [133] A.H. Cottrell, *Dislocations and Plastic Flow in Crystals*, Oxford University Press, London, 1963.
- [134] X.Y. Kong, Y. Ding, Z.L. Wang, *J. Phys. Chem. B* 108 (2004) 570.
- [135] Z.L. Wang, *Nanowires and Nanobelts – Materials, Properties and Devices*, vol. I, Metal and Semiconductor Nanowires, Kluwer Academic Publisher, 2003.
- [136] Z.L. Wang, in: M.H. Geng (Ed.), “*Nanotechnology and Nanomanufacturing*”, Semiconductor Manufacturing Handbook, McGraw-Hill, 2004.
- [137] B.K. Rao, P. Jena, *Phys. Rev. B* 32 (1985) 2058.
- [138] S. Ogut, J.R. Chelikowsky, S.G. Louie, *Phys. Rev. Lett.* 79 (1997) 1770.
- [139] M.F. Jarrold, *Science* 252 (1991) 1085.
- [140] M. Zacharias, J. Heitmann, R. Scholz, U. Kahler, M. Schmidt, J. Blasing, *Appl. Phys. Lett.* 80 (2002) 661.
- [141] R.Q. Zhang, T.S. Chu, H.F. Cheung, N. Wang, S.T. Lee, *Phys. Rev. B* 64 (2001) 113304.
- [142] R. Hoffmann, *Rev. Mod. Phys.* 60 (1988) 601.
- [143] K. Kim, M.S. Suh, T.S. Kim, C.J. Youn, E.K. Suh, Y.J. Shin, K.B. Lee, H.J. Lee, M.H. An, H.J. Lee, H. Ryu, *Appl. Phys. Lett.* 69 (1996) 3908.
- [144] R.Q. Zhang, M.W. Zhao, S.T. Lee, *Phys. Rev. Lett.* 293 (2004) 095503.
- [145] D.K. Yu, R.Q. Zhang, S.T. Lee, *Phys. Rev. B* 65 (2002) 245417.
- [146] R.Q. Zhang, Y. Lifshitz, S.T. Lee, *Adv. Mater.* 15 (2003) 635.
- [147] M. Mamiya, M. Kikuchi, H. Takei, *J. Cryst. Growth* 237 (2002) 1909.
- [148] Ph. Buffat, J.P. Borel, *Phys. Rev. A* 13 (1976) 2287.
- [149] S.W. Cheng, H.F. Cheung, *J. Appl. Phys.* 94 (2003) 1190.
- [150] S.W. Cheng, H.F. Cheung, *Appl. Phys. Lett.* 85 (2004) 5709.
- [151] Y. Wu, Y. Cui, L. Huynh, C.J. Barrelet, D.C. Bell, C.M. Lieber, *Nano Lett.* 4 (2004) 433.
- [152] Y. Ding, P.X. Gao, Z.L. Wang, *J. Am. Chem. Soc.* 126 (2004) 2066.
- [153] A.I. Persson, M.W. Larsson, S. Stenstrom, B.J. Ohlsson, L. Samuelson, L.R. Wallenberg, *Nat. Mater.* 3 (2004) 677.
- [154] A.A. Stekdnikov, J. Furthmüller, F. Bechstedt, *Phys. Rev. B* 65 (2002) 115318.
- [155] D.J. Eaglesham, A.E. White, L.C. Feldman, N. Moriya, D.C. Jacobson, *Phys. Rev. Lett.* 70 (1993) 1643.
- [156] M.S. Gudiksen, L.J. Lauhon, J. Wang, D.C. Smith, C.M. Lieber, *Nature* 415 (2002) 617.
- [157] N. Ozaki, Y. Ohno, S. Takeda, *Appl. Phys. Lett.* 73 (1998) 3700.
- [158] Y. Cui, L.J. Lauhon, M.S. Gudiksen, J. Wang, C.M. Lieber, *Appl. Phys. Lett.* 78 (2001) 2214.
- [159] Z.H. Wu, X. Mei, D. Kim, M. Blumin, H.E. Ruda, J.O. Liu, K.L. Kavanagh, *Appl. Phys. Lett.* 83 (2003) 3368.
- [160] V. Schmidt, S. Senz, U. Gosele, *Nano Lett.* 5 (2005) 931.
- [161] T.Y. Tan, S.T. Lee, U. Gosele, *Appl. Phys. A* 74 (2002) 423.
- [162] T.Y. Tan, N. Li, U. Gosele, *Appl. Phys. A* 78 (2004) 519.
- [163] Y. Zhao, B.I. Yakobson, *Phys. Rev. Lett.* 91 (2003) 35501.
- [164] S.B. Zhang, S.H. Wei, *Phys. Rev. Lett.* 92 (2004) 86102.
- [165] A. Colli, S. Hofmann, A.C. Ferrari, C. Ducati, F. Martelli, S. Rubini, S. Cabrini, A. Franciosi, J. Robertson, *Appl. Phys. Lett.* 86 (2005) 153103.
- [166] A.H. Carim, K.K. Lew, J.M. Redwing, *Adv. Mater.* 13 (2001) 1489.

- [167] Y. Dai, Y. Zhang, Y.Q. Bai, Z.L. Wang, *Chem. Phys. Lett.* 375 (2003) 96.
- [168] R.M. Wang, Y.F. Chen, Y.Y. Fu, H. Zhang, C. Kisielowski, *J. Phys. Chem. B* 109 (2005) 12245.
- [169] X.Y. Kong, Z.L. Wang, *Nano Lett.* 3 (2003) 1625.
- [170] W. Shi, H. Peng, N. Wang, C.P. Li, L. Xu, C.S. Lee, R. Kalish, S.T. Lee, *J. Am. Chem. Soc.* 123 (2001) 11095.
- [171] R.Q. Zhang, Y. Lifshitz, D.D.D. Ma, Y.L. Zhao, Th. Frauenheim, S.T. Lee, S.Y. Tong, *J. Chem. Phys.* 123 (2005) 144703.
- [172] C.P. Li, C.S. Lee, X.L. Ma, N. Wang, R.Q. Zhang, S.T. Lee, *Adv. Mater.* 15 (2003) 607.
- [173] D.D.D. Ma, C.S. Lee, F.C.K. Au, S.Y. Tong, S.T. Lee, *Science* 299 (2003) 1874.
- [174] H.J. Fan, W. Lee, R. Scholz, A. Dadgar, A. Krost, K. Nielsch, M. Zacharias, *Nanotechnology* 16 (2005) 913.
- [175] Z. Fan, D. Wang, P.C. Chang, W.Y. Tseng, J.G. Lu, *Appl. Phys. Lett.* 85 (2004) 5923.
- [176] Z. Fan, P.C. Chang, J.G. Lu, E.C. Walter, R.M. Penner, C.H. Lin, H.P. Lee, *Appl. Phys. Lett.* 85 (2004) 6128.
- [177] Y. Zhang, R.E. Russo, S.S. Mao, *Appl. Phys. Lett.* 87 (2005) 043106.
- [178] C.H. Liu, J.A. Zaprien, Y. Yao, X.M. Meng, C.S. Lee, S.S. Fan, Y. Lifshitz, S.T. Lee, *Adv. Mater.* 15 (2003) 838.
- [179] B. Xiang, P. Wang, X. Zhang, S.A. Dayeh, D.P.R. Aplin, C. Soci, D. Yu, D. Wang, *Nano Lett.* 7 (2007) 323.
- [180] C.H. Liu, W.C. Yiu, F.C.K. Au, J.X. Ding, C.S. Lee, S.T. Lee, *Appl. Phys. Lett.* 83 (2003) 3168.
- [181] H.J. Xiang, J. Yang, J.G. Hou, Q. Zhu, *Appl. Phys. Lett.* 89 (2006) 223111.
- [182] C.Q. Chen, Y. Shi, Y.S. Zhang, J. Zhu, Y.J. Yan, *Phys. Rev. Lett.* 96 (2006) 075505.
- [183] L. Zhang, H. Huang, *Appl. Phys. Lett.* 90 (2007) 023115.
- [184] W. Fan, H. Xu, A.L. Rosa, Th. Frauenheim, R.Q. Zhang, *Phys. Rev. B* 76 (2007) 073302.
- [185] X. Wang, J. Song, Z.L. Wang, *Chem. Phys. Lett.* 424 (2006) 86.
- [186] S. Gradecak, F. Qian, Y. Li, H.G. Park, C.M. Lieber, *Appl. Phys. Lett.* 87 (2005) 173111.
- [187] H. Xu, A.L. Rosa, Th. Frauenheim, R.Q. Zhang, S.T. Lee, *Appl. Phys. Lett.* 91 (2007) 031914.
- [188] H.Y. Peng, N. Wang, W.S. Shi, Y.F. Zhang, C.S. Lee, S.T. Lee, *J. Appl. Phys.* 89 (2001) 727.
- [189] L. Rayleigh, *Proc. London Math. Soc.* 10 (1878) 4.
- [190] F.A. Nichols, W.W. Mullins, *Trans. Metall. Soc. AIME* 233 (1965) 1840.
- [191] P.M. Ajayan, M. Terrones, A. de la Guardia, V. Huc, N. Grobert, B.Q. Wei, H. Lezec, G. Ramanath, T.W. Ebbesen, *Science* 296 (2002) 705.
- [192] J. Huang, R.B. Kaner, *Nat. Mater.* 3 (2004) 783.
- [193] D. Li, Y. Xia, *Nat. Mater.* 3 (2004) 753.
- [194] K. Nishio, J. Koga, H. Ohtani, T. Yamaguchi, F. Yonezawa, *J. Non-Cryst. Solid* 293 (2001) 705.
- [195] G.H. Ding, C.T. Chan, Z.Q. Zhang, P. Sheng, *Phys. Rev. B* 71 (2005) 205302.
- [196] M. Law, J. Goldberger, P. Yang, *Annu. Rev. Mater. Res.* 34 (2004) 83.
- [197] C.N.R. Rao, A. Müller, A.K. Cheetham, *The Chemistry of Nanomaterials: Synthesis, Properties and Applications*, Wiley–VCH, 2004.
- [198] T.C. Wong, C.P. Li, R.Q. Zhang, S.T. Lee, *Appl. Phys. Lett.* 84 (2004) 407.
- [199] C.P. Li, N. Wang, S.P. Wong, C.S. Lee, S.T. Lee, *Adv. Mater.* 14 (2002) 218.
- [200] Y. Wu, J. Xiang, C. Yang, W. Lu, C.M. Lieber, *Nature* 430 (2004) 61.
- [201] K.C. Lu, K.N. Tu, W.W. Wu, L.J. Chen, B.Y. Yoo, N.V. Myung, *Appl. Phys. Lett.* 90 (2007) 253111.
- [202] K.C. Lu, W.W. Wu, H.W. Wu, C.M. Tanner, J.P. Chang, L.J. Chen, K.N. Tu, *Nano Lett.* 7 (2007) 2389.
- [203] Z.M. Liao, J. Xu, Y.P. Song, Y. Zhang, Y.J. Xing, D.P. Yu, *Appl. Phys. Lett.* 87 (2005) 182112.
- [204] Y. Wu, R. Fan, P. Yang, *Nano Lett.* 2 (2002) 83.
- [205] L.J. Lauhon, M.S. Gudiksen, C.M. Lieber, *Philos. Trans. R. Soc. Lond. Ser. A: Math. Phys. Eng. Sci.* 362 (1819) 1247.
- [206] R. Solanki, J. Huo, J.L. Freeouf, B. Miner, *Appl. Phys. Lett.* 81 (2003) 451.
- [207] M.T. Bjork, B.J. Ohlsson, T. Sass, A.I. Persson, C. Thelander, M.H. Magnusson, K. Deppert, L.R. Wallenberg, L. Samuelson, *Nano Lett.* 2 (2002) 87.
- [208] N. Li, Thermodynamic and kinetics on nanowire growth by the vapor–liquid–solid process, Supervisor Prof. T.Y. Tan, PhD dissertation, Department of Mechanical Engineering and Materials Science, Duke University, USA, July 2007.
- [209] T.E. Clark, K.K. Lew, L. Pan, P. Nimmatoori, J.M. Redwing, E.C. Dickey, Diameter dependent growth rate and interfacial abruptness in vapor–liquid–solid Si/Si_{1-x}Ge_x heterostructure nanowires, *Nano Lett.*, submitted for publication.
- [210] M. Paladugu, J. Zou, G.J. Auchterlonie, Y.N. Guo, Y. Kim, H.J. Joyce, Q. Gao, H.H. Tan, C. Jagadisha, *Appl. Phys. Lett.* 91 (2007) 133115.
- [211] D.K. Yu, R.Q. Zhang, S.T. Lee, *J. Appl. Phys.* 92 (2002) 7453.
- [212] M. Menon, E. Richter, *Phys. Rev. Lett.* 83 (1999) 792.
- [213] B. Marsen, K. Sattler, *Phys. Rev. B* 60 (1999) 11593.
- [214] B.X. Li, P.L. Cao, R.Q. Zhang, S.T. Lee, *Phys. Rev. B* 65 (2002) 125305.
- [215] Y. Zhao, B.I. Yakobson, *Phys. Rev. Lett.* 91 (2003) 035501.
- [216] Y. Zhao, Y.H. Kim, M.H. Du, S.B. Zhang, *Phys. Rev. Lett.* 93 (2004) 115502.
- [217] M. Menon, D. Srivastava, I. Ponomareva, L.A. Chernozatonskii, *Phys. Rev. B* 70 (2004) 125313.
- [218] R. Kagimura, R.W. Nunes, H. Chacham, *Phys. Rev. Lett.* 95 (2005) 115502.
- [219] K. Nishio, T. Morishita, W. Shinoda, M. Mikami, *J. Chem. Phys.* 125 (2006) 074712.
- [220] J.X. Cao, X.G. Gong, J.X. Zhong, R.Q. Wu, *Phys. Rev. Lett.* 97 (2006) 136105.
- [221] Z.G. Fthenakis, R.W. Havenith, M. Menon, P.W. Fowler, *Phys. Rev. B* 75 (2007) 155435.
- [222] S.B. Fagan, R.J. Barierle, R. Mota, A.J.R. da Silva, A. Fazzio, *Phys. Rev. B* 61 (2000) 9994.
- [223] G. Seifert, Th. Kohler, H.M. Urbassek, E. Hernandez, Th. Frauenheim, *Phys. Rev. B* 63 (2001) 193409.
- [224] R.Q. Zhang, S.T. Lee, C.K. Law, W.K. Li, B.K. Teo, *Chem. Phys. Lett.* 364 (2002) 251.
- [225] A.S. Barnard, S.P. Russo, *J. Phys. Chem. B* 107 (2003) 7577.
- [226] M. Zhang, Y.H. Kan, Q.J. Zang, Z.M. Su, R.S. Wang, *Chem. Phys. Lett.* 379 (2003) 81.
- [227] J.W. Kang, H.J. Hwang, *Nanotechnology* 14 (2003) 402.
- [228] J.W. Kang, K.R. Byun, H.J. Hwang, *Model. Simul. Mater. Sci. Eng.* 12 (2004) 1.
- [229] J. Bai, X.C. Zeng, H. Tanaka, J.Y. Zeng, *Proc. Natl. Acad. Sci.* 101 (2004) 2664.
- [230] R.Q. Zhang, H.L. Lee, W.K. Li, B.K. Teo, *J. Phys. Chem. B* 109 (2005) 8605.
- [231] M.W. Zhao, R.Q. Zhang, Y. Xia, C. Song, S.T. Lee, *J. Phys. Chem. C* 111 (2007) 1234.
- [232] J. Sha, J.J. Niu, X.Y. Ma, *Adv. Mater.* 14 (2002) 1219.
- [233] B.K. Teo, C.P. Li, X.H. Sun, N.B. Wong, S.T. Lee, *Inorg. Chem.* 42 (2003) 6723.
- [234] X.H. Sun, C.P. Li, W.K. Wong, N.B. Wong, C.S. Lee, S.T. Lee, B.K. Teo, *J. Am. Chem. Soc.* 124 (2002) 14464.
- [235] Y.H. Tang, L.Z. Pei, Y.W. Chen, C. Guo, *Phys. Rev. Lett.* 95 (2005) 116102.
- [236] Y.W. Chen, Y.H. Tang, L.Z. Pei, C. Guo, *Adv. Mater.* 17 (2005) 564.
- [237] M.D. Crescenzi, P. Castrucci, M. Scarsilli, M. Diociaiuti, P.S. Chaudhari, C. Balasubramanian, T.M. Bhave, S.V. Bhoraskar, *Appl. Phys. Lett.* 86 (2005) 231901.
- [238] K.H. Janzon, H. Schafer, A. Weiss, Z. Anorg. Allg. Chem. 372 (1970) 87.
- [239] P. Jena, S.N. Khanna, B.K. Rao, *Physics and Chemistry of Finite System: From Clusters to Crystals*, vols. I and II, Kluwer Academic Publishers, Boston, 1992.
- [240] D.P. Yu, Q.L. Hang, Y. Ding, H.Z. Zhang, Z.G. Bai, J.J. Wang, Y.H. Zou, W. Qian, G.C. Xiong, S.Q. Feng, *Appl. Phys. Lett.* 73 (1998) 3076.
- [241] H. Takikawa, M. Yatsuki, T. Sakakibara, *Jpn. J. Appl. Phys.* 38 (1999) L401.

- [242] X.C. Wu, W.H. Song, K.Y. Wang, T. Hu, B. Zhao, Y.P. Sun, J.J. Du, *Chem. Phys. Lett.* 336 (2001) 53.
- [243] Z.Q. Liu, S.S. Xie, L.F. Sun, D.S. Tang, W.Y. Zhou, C.Y. Wang, W. Liu, Y.B. Li, X.P. Zou, G. Wang, *J. Mater. Res.* 16 (2001) 683.
- [244] W.B. Hu, Y.Q. Zhu, W.G. Xu, *Sci. China Ser. B* 45 (2002) 389.
- [245] J.Q. Hu, Y. Jiang, X.M. Meng, C.S. Lee, S.T. Lee, *Chem. Phys. Lett.* 367 (2003) 339.
- [246] G. Che, B.B. Lakshmi, C.R. Martin, E.R. Fisher, R.S. Ruoff, *Chem. Mater.* 10 (1998) 260.
- [247] C.N.R. Rao, M. Nath, *Dalton Trans.* 1 (2003) 1.
- [248] B.B. Lakshmi, C.J. Patrissi, C.R. Martin, *Chem. Mater.* 9 (1997) 2544.
- [249] M. Zhang, Y. Bando, K. Wada, *J. Mater. Res.* 15 (2000) 187.
- [250] S.O. Obare, N.R. Jana, C.J. Murphy, *Nano Lett.* 1 (2001) 601.
- [251] Y. Yin, Y. Lu, Y. Sun, Y. Xia, *Nano Lett.* 2 (2002) 427.
- [252] D.T. Mitchell, S.B. Lee, L. Trofin, N. Li, T.K. Nevanen, H. Soderlund, C.R. Martin, *J. Am. Chem. Soc.* 124 (2002) 11864.
- [253] H.S. Qian, S.H. Yu, L. Ren, Y.P. Yang, W. Zhang, *Nanotechnology* 17 (2006) 5995.
- [254] N.I. Kovtyukhova, T.E. Mallouk, T.S. Mayer, *Adv. Mater.* 15 (2003) 780.
- [255] L.Z. Wang, S. Tomura, F. Ohashi, M. Maeda, M. Suzuki, K. Inukai, *J. Mater. Chem.* 11 (2001) 1465.
- [256] L.S. Wang, S.R. Desai, H. Wu, J.B. Nichloas, *Z. Phys. D* 40 (1997) 36.
- [257] M. Iraqi, N. Goldberg, H. Schwarz, *J. Phys. Chem.* 97 (1993) 11371.
- [258] N. Goldberg, M. Iraqi, W. Koch, H. Schatzl, *Chem. Phys. Lett.* 225 (1994) 404.
- [259] P.E. Lafargue, J.J. Gaumet, J.F. Muller, *J. Mass Spectrom.* 31 (1996) 623.
- [260] L.S. Wang, H. Wu, S.R. Desai, J. Fan, S.D. Colson, *J. Phys. Chem.* 100 (1996) 8697.
- [261] L. Zhao, L. Zhu, J. Zhang, Y. Li, J. Sheng, B. Zhang, J. Wang, *Chem. Phys. Lett.* 255 (1996) 142.
- [262] L.S. Wang, J.B. Nicholas, M. Dupuis, H. Wu, S.D. Colson, *Phys. Rev. Lett.* 78 (1997) 4450.
- [263] I.S. Altman, D. Lee, J.D. Chung, J. Song, M. Choi, *Phys. Rev. B* 63 (2001) 161402.
- [264] Y.D. Glinka, S.H. Lin, Y.T. Lin, Y.T. Chen, *Phys. Rev. B* 62 (2000) 4733.
- [265] T. Uchino, A. Aboshi, S. Kohara, Y. Ohishi, M. Sakashita, K. Aoki, *Phys. Rev. B* 69 (2004) 155409.
- [266] L.C. Snyder, K. Raghavachari, *J. Chem. Phys.* 80 (1984) 5076.
- [267] A.I. Boldyreva, J. Simons, *J. Phys. Chem.* 97 (1993) 5875.
- [268] T. Sommerfeld, M.K. Scheller, L.S. Cederbaum, *J. Chem. Phys.* 103 (1995) 1057.
- [269] J.A.W. Harkless, D.K. Stillinger, F.H. Stillinger, *J. Phys. Chem.* 100 (1996) 1098.
- [270] S.K. Nayak, B.K. Rao, S.N. Khanna, P. Jena, *J. Chem. Phys.* 109 (1998) 1245.
- [271] J.R. Chelikowsky, *Phys. Rev. B* 57 (1998) 3333.
- [272] C. Xu, W. Wang, W. Zhang, J. Zhuang, L. Liu, Q. Kong, L. Zhao, Y. Long, K. Fan, S. Qian, Y. Li, *J. Phys. Chem. A* 104 (2000) 9518.
- [273] J.M. Nedelev, L.L. Hench, *J. Non-Cryst. Solids* 277 (2000) 106.
- [274] T.S. Chu, R.Q. Zhang, H.F. Cheung, *J. Phys. Chem. B* 105 (2001) 1705.
- [275] E. Flikkema, S.T. Bromley, *Chem. Phys. Lett.* 378 (2003) 622.
- [276] E. Flikkema, S.T. Bromley, *J. Phys. Chem. B* 108 (2004) 9638.
- [277] D.J. Wales, J.P.K. Doye, *J. Phys. Chem. A* 101 (1997) 5111.
- [278] J. Song, M. Choi, *Phys. Rev. B* 65 (2002) 241302.
- [279] P. Umar, X. Gonze, A. Pasquarello, *Phys. Rev. Lett.* 90 (2003) 027401.
- [280] W.C. Lu, C.Z. Wang, K.M. Ho, *Chem. Phys. Lett.* 378 (2003) 225.
- [281] W.C. Lu, C.Z. Wang, V. Nguyen, M.W. Schmidt, M.S. Gordon, K.M. Ho, *J. Phys. Chem. A* 107 (2003) 6936.
- [282] M.W. Zhao, R.Q. Zhang, S.T. Lee, *Phys. Rev. B* 69 (2004) 153403.
- [283] S.T. Bromley, M.A. Zwijnenburg, Th. Maschmeyer, *Phys. Rev. Lett.* 90 (2003) 035502.
- [284] Q. Sun, Q. Wang, P. Jena, *Phys. Rev. Lett.* 92 (2004) 039601.
- [285] S.T. Bromley, M.A. Zwijnenburg, E. Flikkema, Th. Maschmeyer, *Phys. Rev. Lett.* 92 (2004) 039602.
- [286] M.W. Zhao, R.Q. Zhang, S.T. Lee, *Phys. Rev. B* 70 (2004) 205404.
- [287] D.J. Zhang, R.Q. Zhang, *Chem. Phys. Lett.* 394 (2004) 437.
- [288] D.J. Zhang, R.Q. Zhang, *J. Phys. Chem. B* 110 (2006) 1338.
- [289] T. Zhu, J. Li, S. Yip, R.J. Bartlett, S.B. Trickey, N.H. Deleeuw, *Mol. Simul.* 29 (2003) 671.
- [290] L. Kronik, R. Fromherz, E. Ko, G. Ganterförl, J.R. Chelikowsky, *Nat. Mater.* 1 (2002) 49.
- [291] D.T. Mitchell, S.B. Lee, T. Trofin, N.C. Li, T.K. Nevanen, H. Soderlund, C.R. Martin, *J. Am. Chem. Soc.* 124 (2002) 11864.
- [292] S.B. Lee, D.T. Mitchell, L. Trofin, T.K. Nevanen, H. Soderlund, C.R. Martin, *Science* 296 (2002) 2198.
- [293] M. Zhang, E. Ciocan, Y. Bando, K. Wada, L.L. Cheng, P. Pirouz, *Appl. Phys. Lett.* 80 (2002) 491.
- [294] E.A. Whitsitt, A.R. Barron, *Nano Lett.* 3 (2003) 775.
- [295] J.Q. Hu, X.M. Meng, Y. Jiang, C.S. Lee, S.T. Lee, *Adv. Mater.* 15 (2003) 70.
- [296] C.R. Martin, *Chem. Mater.* 8 (1996) 1739.
- [297] B.C. Satshkumar, A. Govindaraj, E.M. Vogl, L. Basumallick, C.N.R. Rao, *J. Mater. Res.* 12 (1997) 604.
- [298] B.B. Lakshmi, P.K. Dorhout, C.R. Martin, *Chem. Mater.* 9 (1997) 857.
- [299] R. Fan, Y. Wu, D. Li, M. Yue, A. Majumdar, P. Yang, *J. Am. Chem. Soc.* 125 (2003) 5254.
- [300] Z.L. Wang, R.P. Gao, J.L. Gole, J.D. Stout, *Adv. Mater.* 12 (2000) 1938.
- [301] C. Liang, Y. Shimizu, T. Sasaki, H. Umehara, N. Koshizaki, *J. Mater. Chem.* 14 (2004) 248.
- [302] M.E. Spahr, P. Bitterli, R. Nesper, M. Muller, F. Krumeich, H.U. Nissen, *Angew. Chem. Int. Ed.* 37 (1998) 1263.
- [303] J.H. Jung, S. Shinkai, T. Shimizu, *Nano Lett.* 2 (2002) 17.
- [304] N.H. de Leeuw, Z. Du, J. Li, S. Yip, T. Zhu, *Nano Lett.* 3 (2003) 1347.
- [305] S.T. Bromley, *Nano Lett.* 4 (2004) 1427.
- [306] M.W. Zhao, R.Q. Zhang, Y.Y. Xia, S.T. Lee, *Phys. Rev. B* 73 (2006) 195412.
- [307] A. Weiss, *Z. Anorg. Allg. Chem.* 276 (1954) 95.
- [308] M.S. Dresselhaus, G. Dresselhaus, P. Avouris, *Carbon Nanotubes: Synthesis, Structure, Properties, and Applications*, Springer, New York, 2001.
- [309] T. Schroeder, M. Adelt, B. Richter, M. Naschitzki, J.B. Giorgi, M. Bäumer, H.J. Freund, *Surf. Rev. Lett.* 7 (2000) 7.
- [310] M.S. Chen, A.K. Santra, D.W. Goodman, *Phys. Rev. B* 69 (2004) 155404.
- [311] J. Weissenrieder, S. Kaya, J.L. Lu, H.J. Gao, S. Shaikhutdinov, H.J. Freund, M. Sierka, T.K. Todorova, J. Sauer, *Phys. Rev. Lett.* 95 (2005) 076103.
- [312] J.P. Liu, *Phys. Rev. Lett.* 79 (1997) 1297.
- [313] X. Chen, S. Zhang, G.J. Wagner, W. Ding, R.S. Ruoff, *J. Appl. Phys.* 95 (2004) 4823.
- [314] N.G. Chopra, R.J. Luyken, V.H. Crespi, M.L. Cohen, S.G. Louie, A. Zettl, *Science* 269 (1995) 966.
- [315] T. Taquchi, N. Iqawa, H. Yamamoto, S. Jitsukawa, *J. Am. Chem. Soc.* 88 (2005) 459.
- [316] Y.J. Xing, Z.H. Xi, X.D. Zhang, J.H. Song, R.M. Wang, J. Xu, Z.Q. Xue, D.P. Yu, *Solid State Commun.* 129 (2004) 671.
- [317] A. Wei, X.W. Sun, C.X. Xu, Z.L. Dong, M.B. Yu, W. Huang, *Appl. Phys. Lett.* 88 (2006) 213102.
- [318] Y.J. Xing, Z.H. Xi, Z.Q. Xue, X.D. Zhang, J.H. Song, R.M. Wang, J. Xu, Y. Song, S.L. Zhang, D.P. Yu, *Appl. Phys. Lett.* 83 (2003) 1689.
- [319] W.Z. Xu, Z.Z. Ye, D.W. Ma, H.M. Lu, L.P. Zhu, B.H. Zhao, X.D. Yang, Z.Y. Xu, *Appl. Phys. Lett.* 87 (2005) 93110.
- [320] Z.C. Tu, X. Hu, *Phys. Rev. B* 74 (2006) 035434.
- [321] S. Erkoç, H. Kökten, *Phys. E* 28 (2005) 162.
- [322] H. Xu, R.Q. Zhang, X.H. Zhang, A.L. Rosa, Th. Frauenheim, *Nanotechnology* 18 (2007) 485713.
- [323] S.M. Lee, Y.H. Lee, Y.G. Hwang, J. Elsner, D. Porezag, Th. Frauenheim, *Phys. Rev. B* 60 (1999) 7788.
- [324] E. Hernández, C. Goze, P. Bernier, A. Rubio, *Phys. Rev. Lett.* 80 (1998) 4502.
- [325] D.H. Robertson, D.W. Brenner, J.W. Mintmire, *Phys. Rev. B* 45 (1992) 12592.
- [326] G.Y. Guo, J.C. Lin, *Phys. Rev. B* 71 (2005) 165402.
- [327] D.H. Oh, Y.H. Lee, *Phys. Rev. B* 58 (1998) 7407.